UNIVERSITY OF CALIFORNIA
SANTA CRUZ

EXPLORING GALACTIC NUCLEI WITH TIDAL DISRUPTION EVENTS

A dissertation submitted in partial satisfaction of the
requirements for the degree of

Doctor of Philosophy

in

ASTRONOMY AND ASTROPHYSICS

by

Brenna Mockler

June 2022

The Dissertation of Brenna Mockler is approved:

Enrico Ramirez-Ruiz, Chair

Daniel Kasen

Ruth Murray-Clay

Smadar Naoz

Peter F. Biehl
Vice Provost and Dean of Graduate Studies

Table of Contents

List of Figures

3.3 We compare the predicted values for νL_ν and L_{bol} from `MOSFiT` to the observed FUV luminosities and corresponding L_{bol} estimates from van Velzen et al. (2019). The 'predicted' values are calculated by extrapolating the `MOSFiT` fits out to the relevant observation times. The x-axis is in units of time from first mass fallback normalized by the peak timescale (this removes the influence M_h has on the light curve timescale). The uncertainties in the model luminosities come from the fits to early-time data (as shown in the inset light curves). The model uncertainties are then added in quadrature with the uncertainties from the observations. *Top Panel:* νL_ν is calculated at $\gamma = 1500$Å. $\nu L_{\nu,\,\mathrm{observed}}$ is derived from HST observations with the F125LP and F150LP filters (for 10jh, D3-13, D1-9, 09djl, and 09ge) and from Swift observations in the UVOT filters (for 14li, 14ae, and 16fnl). The `MOSFiT` extrapolation set the minimum photosphere radius to R_{isco}. *Bottom Panel:* To calculate $L_{bol,\,\mathrm{predicted}}$, the model efficiency was assumed to be constant at late times. $L_{bol,\,\mathrm{observed}}$ was estimated from blackbody fits to observations in the filters listed above. There is significant uncertainty in the estimate of $L_{bol,\,\mathrm{observed}}$ due to the lack of SED coverage. 16fnl has a late-time observation in just one filter, therefore $L_{bol,\,\mathrm{observed}}$ was calculated using the temperature estimated from blackbody fits at early times and we are thus unable to accurately estimate the associated uncertainties for this measurement. *Inset Plots:* We plot νL_ν and L_{bol} light curves for 14li to give the reader an idea of how the discrepancies between the model and the observations shown in this plot map to a typical light curve. The green shaded curves are the model fits to the early time data, the black points are the late time observations. The x-axes units are the same as for the larger plots. 91

List of Tables

3.1 **Notes for Table 3.1:** The transients in the table are organized as follows: The first 9 events have UV detections during the same time period as the optical detections. The events in bold have observations at or before the light curve peak. Systematic errors for parameters are listed at the top of their respective columns, throughout the text we include the systematic errors in the errors quoted for the parameters. Systematic errors for $t_{\rm peak}$ and efficiency (ϵ) are taken from Mockler et al. (2019a), additional errors were calculated using the method described in the same paper and are based on the uncertainty in the stellar mass-radius relation. **Column descriptions:** (1) transient names; (2) Bolometric energy estimates from the literature. The methods used to calculate these estimates are described below in this caption; (3) Bolometric energy estimates from the `MOSFiT` fits, integrated over the same time period used for the literature energy estimates in column 2. The literature energy estimate for PTF09ge is from late-time dust emission and therefore the `MOSFiT` energy estimate for column 3 for this event was integrated over the time period of the initial optical observations presented in Arcavi et al. (2014); (4) Column 2 divided by column 3; (5) The peak bolometric luminosity multiplied by the timescale from first fallback to peak luminosity, divided by column 3; (6) The Δt between when the first stellar debris falls back to pericenter ('first fallback') and the time of peak luminosity. This is necessarily less than the time from disruption to peak; (7) & (8) t_{50} and t_{90} are the respective times when 50% and 90% of the total energy is radiated. The first 5% and last 5% are excluded from the integral. In columns 7 & 8 they are scaled by the peak timescale calculated from first fallback; (9) The average observed efficiency, defined as $E_{\rm bol}/\Delta Mc^2$, where ΔM is the total amount of mass that is bound to the black hole; (10) The peak observed efficiency, defined as $L_{\rm peak}/\dot{M}_{\rm peak}c^2$; (11) Eddington ratio at peak luminosity; (12) The minimum amount of mass required to generate the integrated energy if the conversion from mass to energy were 100% efficient ($E_{\rm bol} = \Delta M_{\rm min}c^2$). **Notes on literature energy estimates:** The value for PS1-10jh was calculated by integrating the light-curve model using a lower limit for the temperature and luminosity (Gezari et al. 2012). The values for both D1-9 and D3-13 were calculated by integrating a $t^{-5/3}$ power law starting at $t_{\rm discovery}$ (after $t_{\rm peak}$) using the lower limits to the blackbody temperature and luminosity (Gezari et al. 2008). The value for PTF09ge was calculated from IR dust emission, motivating that there is additional radiated energy not observed in the initial optical and UV light curve (van Velzen et al. 2016a). The values for ASASSN-14ae, ASASSN-14li, ASASSN-15oi, iPTF16fnl, iPTF16axa, and OGLE16aaa were calculated by integrating the blackbody fits to the observed optical and UV light curves (Holoien et al. 2014, 2016b,a; Blagorodnova et al. 2017; Hung et al. 2017; Wyrzykowski et al. 2017). According to Holoien et al. (2016b), the blackbody fit for ASASSN-14li was 'dominated by systematic errors'. For PS1-11af, Chornock et al. (2014) calculated the radiated energy by using a constant bolometric correction to the light curve from a blackbody fit 10 rest-frame days after peak. 66

Abstract

Exploring Galactic Nuclei with Tidal Disruption Events

by

Brenna Mockler

One of the most promising avenues for studying supermassive black holes (SMBHs) in the local Universe is through tidal disruption events (TDEs). TDEs occur when unlucky stars pass too close to a black hole and are torn apart and consumed. This often pushes the black holes to their critical Eddington limits, outshining their galactic centers and encoding the resultant light curves with a wealth of information about the disrupter and disruptee (e.g. Rees 1988). Observations of TDEs are quickly becoming commonplace (e.g. van Velzen et al. 2020), with over 50 confirmed disruptions discovered in the last decade, and thousands more expected to be observed by upcoming time-domain surveys such as the Vera Rubin Observatory. These phenomena provide an exciting opportunity to study SMBHs in quiescent galaxies, the stellar populations in galactic nuclei, and the physics of black hole accretion under well defined conditions. In this thesis I develop a new model for the light curves of tidal disruption events, and combine it with data from observed tidal disruption events and dynamical models of galactic nuclei to learn about the properties and evolution of the supermassive black holes at the centers of galaxies as well as the stars that surround them.

I first describe the components of the light curve model, and use it to fit a population of observed TDEs. I show that the model can estimate the masses of the disrupting black holes as well as other properties of the system. I then use energy and

efficiency estimates from the models to constrain the emission mechanism, as the source of the emission for the majority of these transients is hidden inside a layer of stellar debris and cannot be observed directly. I compare my results to similar measurements of active galactic nuclei. Next, I combine the light curve models with data from the spectra and host galaxies of TDEs to put constraints on the masses of disrupted stars for several events. I find that they have high nitrogen-to-carbon abundances, implying stellar masses $\gtrsim 1 - 2M_{\odot}$. These 'moderately massive' stars are over-represented by a factor of $\gtrsim 10^2$ compared to the overall stellar population of the hosts. Finally, I explore how SMBH binaries can increase the rates of tidal disruptions in post-merger galaxies, and how TDEs can, in turn, help us discover SMBH binaries.

Acknowledgments

I must begin by thanking my advisor, Enrico Ramirez-Ruiz, without whose tireless support this dissertation would not have been possible. His intuition and excitement helped me find my own joy in scientific discovery and his early belief in my capability as an astrophysicist helped build the confidence I needed to make my own contributions to this field. I do not know how I got so lucky to find an advisor who is not only an excellent scientific mentor, but who also cares deeply about his community, and who so often goes above and beyond to support his students and collaborators outside of their scientific endeavours. This community has given me a number of lovely collaborators and friends, who I'd like to thank for their support over the years. Sophie, who was with me every step of the way, and who I am so happy to graduate with this summer. Katie, whose support and advice have been invaluable from the beginning, and who made conferences less scary and much more fun. Phil, Ari, Jamie, Rosa, Sierra, and many others who helped make Enrico's group so supportive and enjoyable to be a part of.

I also owe a great deal of thanks to Dan Kasen and Smadar Naoz. Thank you for letting me insert myself into your wonderful research groups, for being patient and providing support as I developed new skills, and for your thoughtful perspectives and advice on science and life.

I would also like to thank the UC Santa Cruz graduate student community and in particular the astronomy graduate students. You are ultimately the reason I came to this graduate program and you have shown me many times over that I made the right

decision. It has been such a relief to find a group of people in academia who care more about community than competition and career advancement. You all are brilliant and talented and I cannot wait to watch what you do next.

Thank you especially to Tyler for being my best friend and for your endless belief in me. I'm so grateful I've had the opportunity to grow and learn with you, and I'm looking forward to continuing to do so for many more years.

Finally, thank you to my parents Ann & Rick for giving me the room to grow in whatever direction I chose, and for always being there to lend a hand. And to my sister Alana – thank you for teaching me patience and for showing me how to slow down and think carefully when I'd normally rush ahead. I love you very much.

Published Material

The text of this dissertation includes reprints of the following published material led by Mockler, with the permission of the listed coauthors.

Chapter 1 was published in the literature as Mockler et al. (2019a). I was responsible for developing the models, performing the analysis, as well as creating the figures and writing the text, with the exception of §2.2.1, which was written in part by James Guillochon. I wish to thank my coauthors Enrico Ramirez-Ruiz and James Guillochon for their generous support and feedback in the course of this research.

Chapter 2 was published in the literature as Mockler & Ramirez-Ruiz (2020). I was responsible for developing the models and performing the analysis, as well as creating the figures and writing the text. I wish to thank my coauthor Enrico Ramirez-Ruiz for his generous support and feedback in the course of this research.

Chapter 3 was published in the literature as Mockler et al. (2022). I was responsible for performing the analysis, creating the figures, as well as writing the text, with the exception of §4.6.2, which was written by Katie Auchettl. Figure§4.1 was created together with Angela Twum, and Figure§4.3 was created with help from Sierra Dodd and Jamie A.P. Law-Smith. I wish to thank my coauthors Angela Twum, Katie Auchettl, Sierra Dodd, K.D. French, Jamie A.P. Law-Smith, and Enrico Ramirez-Ruiz for their generous support and feedback in the course of this research.

Scientific Acknowledgments

I gratefully acknowledge research support from the AAUW and UCSC President's dissertation year fellowships. I also acknowledge support from the Danish National Research Foundation (DNRF132) and Swift grant 80NSSC21K1409, as well as NASA ATP grant NNX14AH37G, NSF grants (AST-1615881, AST-1911206 and AST-1852393), Chandra grant GO9-20122X, and Swift grant 80NSSC19K1391 to Enrico Ramirez-Ruiz.

I would further like to thank to James Guillochon for his development of the `MOSFiT` code and for his mentorship while I developed the research presented in Chapter§2 of this thesis. Thank you also to Angela Twum, David Khatami, Jane Dai, Nathaniel Roth, Decker French, Jamie Law-Smith, and Tiara Hung for their collaboration and for the enlightening and enjoyable conversations that helped shape the direction of this dissertation.

Chapter 1

Introduction

Tidal disruptions events (TDEs) light up quiescent galaxies, exposing black holes that are not actively accreting. The singular origin of the accreted mass makes it possible to constrain properties of the star the mass came from, and also makes it simpler to constrain the total amount of mass available to be accreted, as it is limited by the mass of the one disrupted star. These accretion events regularly bring black holes to their Eddington limits – a black hole's theoretical maximum accretion limit – probing the growth constraints of supermassive black holes.

This thesis uses TDEs as tools to constrain properties of supermassive black holes (SMBHs) and galactic nuclei, and explores the connection between the properties and rates of TDEs and the evolution of the host galaxy. It benefited greatly from the increase in state-of-the-art hydrodynamic simulations of tidal disruption processes, as well as the explosion in observations of TDEs that occurred over the past 10 years. This work seeks to synthesize these results by fitting theoretical models of light curves to

observations, and by combining constraints from light curves, spectra, and host galaxy observations to estimate physical quantities such as the masses of the black holes and disrupted stars, the pericenter of the star's orbit when it was disrupted, and the efficiency of black hole accretion during these transient events. Before delving into the projects that make up this thesis, I will begin with some background.

1.1 Light curve modeling of TDEs

Long before tidal disruption events were first observed, they were theorized as a natural consequence of the co-existence of the supermassive black holes that reside at the centers of galaxies and the nuclear star clusters that surround them (e.g. Rees 1988). If a star gets too close to its giant neighbor, the tidal forces from the SMBH grow large enough to rip the star apart. It is possible to calculate the approximate radius where this occurs by equating the tidal force with the self-binding energy of the star and solving for the radius where they are equal. This 'tidal radius' can also be calculated by determining the size of the sphere where, if we spread out the black hole's mass uniformly throughout it, the sphere's density would match the average density of the star (a Hill radius argument):

$$M_h/R_t^3 = M_*/R_*^3 \tag{1.1}$$

$$R_t = R_*\Big(\frac{M_h}{M_*}\Big)^{1/3} \tag{1.2}$$

It turns out that the shape and magnitude of the light curves can be reasonably well predicted by estimating the spread in orbital energy of a star during its pericenter passage (at the approximate point of disruption). This allowed early theoretical work to predict some of the key signatures of these events, including their approximate peak luminosities and decay timescales (Rees 1988; Evans & Kochanek 1989). Most stars that get close enough to be disrupted will be on extremely high eccentricity orbits. By approximating the orbit as parabolic (barely unbound), we can find simple relations between the properties of the star and the black hole and the rate that mass returns to the black hole after disruption (e.g. Kesden 2012a; Lodato et al. 2009; Guillochon & Ramirez-Ruiz 2013, see Chapter 2.2 for more detail):

$$\frac{dm}{dt} \propto t^{-5/3} \tag{1.3}$$

$$\frac{dm}{dt} \propto M_h^{-1/2} M_*^2 R_*^{-3/2} \tag{1.4}$$

$$t \propto M_{\rm h}^{1/2} M_*^{-1} R_*^{3/2} \tag{1.5}$$

Given that the luminosity generated by TDEs is powered by the mass from the disrupted star that falls back to the black hole, a simple assumption to make is that the shape of the light curve follows the mass fallback rate (the rate of mass return, $\frac{dm}{dt}$). Observations of these transients have confirmed that this assumption is generally accurate – TDE light curves do follow the expected mass fallback rates to the black hole (e.g. Gezari et al. 2012; Mockler et al. 2019a, see Chapter 2.6.1).

1.1.1 Converting mass to luminosity

While initial theoretical predictions for the peak luminosities and timescales of these transients have proved impressively accurate, observations of TDEs have generated many new questions. For example, TDEs were expected to be bright at x-ray wavelengths, similar to other accreting black holes such as active galactic nuclei (AGN), but the majority of observed flares have been discovered by optical transient surveys. These TDEs are emitting at temperatures between $10^4 - 10^5 K$, much lower than would be expected if the luminosity was coming directly from an accretion disk around a SMBH. It is now generally assumed that much of the initial emission is reprocessed to lower wavelengths by the significant amount of stellar debris surrounding the black hole (the details of this process are still somewhat uncertain, Roth et al. 2016; Roth & Kasen 2018; Dai et al. 2018). The very high mass accretion rates can also push the black hole to its Eddington limit (peak luminosities are generally within a factor of a few of $L_{\rm Edd}$, see Chapter 3):

$$L_{\rm edd} = 4\pi G M_h c/\kappa_T \tag{1.6}$$

where κ_T is the mean Thomson opacity, and the Eddington limit of a $10^6_\odot$ black hole is approximately 1.4×10^{44} erg/s.

Because the gas from the star is expected to obscure the source of the luminosity, debate has arisen over the mechanism producing the majority of the luminosity. The two leading theories are that it is either due to the formation and evolution of an accretion disk close to the circularization radius of the debris (as was originally assumed, e.g. Rees 1988; Evans & Kochanek 1989) or to the initial orbiting debris streams collid-

ing at large radii from the black hole (e.g. Piran et al. 2015). The origin of the emission has important implications for the mass-to-energy efficiency of these flares. Accretion processes at small radii are expected to be significantly more efficient at producing luminosity than stream collisions farther away from the black hole, and assuming the wrong mechanism can lead to a inaccurate estimates of the mass accreted and energy released during these events. Chapter 3 analyzes a population of TDEs to determine trends in the amount of energy released and the mass-to-energy efficiency of the flares to help answer the question of how the energy is produced. We would like to use TDEs to learn about general properties of accreting black holes (for example, to get constraints on the efficiency of super-Eddington accretion), but to do this we must know whether we are observing luminosity from an accretion disk or from the earlier circularization process.

Closely connected to the question of the nature of the emission mechanism is the problem of how material from the star is able to lose energy and move from very eccentric, high energy orbits onto more circular orbits to eventually form an accretion disk. Regardless of the source of the initial luminosity, an accretion disk is expected to eventually form due to the high angular momentum of the orbiting debris. However, if the disk forms more slowly than the material returns to the black hole, the luminosity from the disk would have no reason to trace the mass fallback rate of debris from the black hole. If the majority of the initial luminosity is produced by the accretion disk, and the luminosity tracks the fallback rate, this circularization of the debris from the star to form the disk must happen on timescales shorter than the mass fallback rate timescale. This is generally true for any emission mechanism – for the luminosity to

track the fallback rate, the timescale of luminosity production must be shorter than the mass fallback timescale. If the timescale of luminosity production is longer than the timescale of mass return to the black hole, we would expect it to dominate over the mass fallback timescale, and we would not expect the light curve to follow the mass fallback rate to the black hole. Multiple theoretical works have shown that if the initial pericenter passage of the star is very relativistic (with R_p of order $10R_g$ or less), general relativistic precession will cause the debris stream orbits to intersect, allowing them to quickly lose energy and circularize into a disk on much shorter timescales than the mass fallback rate (Bonnerot et al. 2016b; Bonnerot & Lu 2020; Andalman et al. 2022). However, we expect there to be many more shallow, partial disruptions at larger radii than deep, relativistic disruptions close to the gravitational radius of the black hole (assuming the dominant dynamical mechanism moving stars onto disrupting orbits is two-body relaxation, e.g. Stone & Metzger 2016). It is possible that we are less likely to observe these shallow encounters – either because the partial disruption of the star does not feed enough mass to the black hole to produce a bright transient (regardless of the emission mechanism), or because the luminosity production timescale is long (e.g. because it is produced by a disk that takes a long time to form), and therefore the energy released is smeared out over much longer timescales and the instantaneous luminosity is lower (Guillochon & Ramirez-Ruiz 2015a). Either of these outcomes would produce flares that would be more difficult to observe with wide field transient surveys. Constraints on the black hole masses and impact parameters of disruption can help us understand the properties and emission mechanisms of the TDEs we do observe. An

understanding of the properties and rates of observed events can also help us understand what flares we might be missing. Chapters 2 and 3 analyze the properties of a large population of TDEs, and Chapter 3 estimates the pericenter and circularization radii of the stars before disruption and the debris afterwards for the same events. Chapter 4 explores observed rates of tidal disruptions for different stellar masses versus what we would expect from the galaxies' stellar populations.

1.1.2 TDEs as measurements of black hole masses

For TDEs whose observed light curves do follow their mass fallback rates, Equations 1.4 and 1.5 describe the dependence of the light curve on the mass of the black hole. Of particular interest is the time-dependence on the black hole mass. For most main sequence stars, the time-dependence on the mass and radius of the star nearly cancel out, and the rise timescales of TDEs vary by less than a factor of 2 when the stellar mass varies between 0.1 and 10 $M_\odot$ (Guillochon & Ramirez-Ruiz 2013, see Chapter 2.7). Because of this, we are able to use the timescales of the light curves of these events to uniquely constrain the masses of the disrupting black holes. Chapter 2 describes in detail how we can extract black hole masses from TDE light curves. This is particularly exciting because TDEs preferentially probe lower mass SMBHs that are difficult to measure using dynamical mass measurement methods. The majority of constraints we have on black hole masses below $\sim 10^7 M_\odot$ come from AGN (e.g. Xiao et al. 2011), and most galaxies do not host AGN (Greene & Ho 2007). At black hole masses above $\sim 10^8 M_\odot$, most stars will only be disrupted inside the event horizon of the black hole, where we cannot observe their deaths (evolved stars with puffier envelopes

can be disrupted by slightly higher mass SMBHs, but as the black hole mass increases they too will eventually only be disrupted once they are already inside the black hole; e.g. MacLeod et al. 2012; Kesden 2012b). Therefore, our observations of TDEs are dominated by transients from black holes $\lesssim 10^8 M_\odot$, in the regime where it is otherwise difficult to measure the masses of quiescent black holes. Our understanding of how massive black holes form and how galaxies evolve with their black holes is dependent on our understanding of the black hole mass function, which is expected to peak at lower masses where there are very few measurements to constrain it. TDEs have already begun to help fill in the black hole mass function between $\sim 10^5 M_\odot - 10^8 M_\odot$, and the expected increase in TDEs from upcoming transient surveys should provide a population of low-mass SMBHs with masses estimated through this method.

1.2 Nuclear stellar populations and host galaxies

Tidal disruption events make it possible to study stars in the very centers of galaxies at size scales that we cannot resolve directly outside our closest galactic neighbors. Because of this, TDEs provide a path towards learning about the stellar populations in galactic nuclei, and therefore also about the dynamics and star formation history of the host galaxies.

Previous work has generally assumed that the population of stars disrupted in TDEs follow the stellar population of the galaxy at large (with a slight dependence on the tidal radius of the star, e.g. MacLeod et al. 2012; Stone & Metzger 2016), and that this population in turn follows a Kroupa initial mass function (Kroupa 2001).

The process of moving stars onto disrupting orbits is most often described through the dynamics of two-body relaxation. For a single SMBH in a spherical stellar cusp, it is the most efficient dynamical process for producing TDEs. Stars interact randomly with other stars in the stellar cusp surrounding the black hole, receiving angular momentum kicks from these interactions that change the stars' orbital trajectories and, if they are unlucky, send them plunging towards the central black hole (e.g. Frank & Rees 1976; Magorrian & Tremaine 1999; Stone & Metzger 2016).

These assumptions have been challenged by population studies of the host galaxies of TDEs and the properties of the disrupted stars, which have discovered unexpected trends. For example, Arcavi et al. (2014); Law-Smith et al. (2017b); French et al. (2020) showed that TDEs have a surprising preference for rare, post-starburst host galaxies. Possible theories explaining this host galaxy preference include different dynamical mechanisms disrupting stars in these galaxies (Arcavi et al. 2014; Madigan et al. 2018), or very concentrated stellar cusps (Stone et al. 2018), however the problem remains unresolved. In Chapter 4 we describe another TDE population anomaly. We find that observed events show a preference for disrupting stars with high metallicities, requiring masses $\gtrsim 1 - 2M_{\odot}$ assuming normal stellar evolution.

Explaining these anomalies in the observed rates of TDEs requires understanding the stellar populations in these galaxies, as well as how stars move onto disrupting orbits in the first place. In Chapters 4 and 5 we discuss how different star formation histories and dynamical processes can change the observed rates of TDEs, and how we might use TDEs to learn about properties of the host galaxies.

1.2.1 Connecting spectra to stellar composition

In TDEs, stars are pulled apart by the black hole before they are consumed. Their outer layers are tightly bound to the black hole and consumed first, while the core of the star is saved for last. In principle, this stellar dissection makes it possible to study different layers of the star individually as they are accreted. There are strong contrasts in composition between the outer layers and the core, particularly for evolved stars, and by looking at the time-dependent composition of the debris as it returns to the black hole, it is possible to put constraints on the mass and age of the disrupted star (Kochanek 2015; Gallegos-Garcia et al. 2018; Law-Smith et al. 2019). Composition abundance ratios can be imprinted in the line ratios from spectra taken from the event (this has previously been studied in detail for AGN, e.g. Hamann & Ferland 1993; Batra & Baldwin 2014), however the radiation transfer process also impacts the strength of spectral lines and complicates the the connection between composition and spectra (Roth et al. 2016).

While no radiation transport simulations of these events have been run that include elements heavier than helium, in some cases it is possible to sidestep the dependence that the spectral line ratios have on the radiation transfer process. For example, the connection between the composition abundance and UV line ratio of N III/C III is much less dependent on gas conditions, because the UV N III (λ1750) and C III (λ1908) line transitions have similar critical densities and excitation energies, and involve ions with similar ionization energies. This allowed Yang et al. (2017) to estimate a minimum N/C abundance ratio for several TDEs, and in Chapter 4 these results are combined

with modeling of the transient light curves and of the star formation history of the host galaxies to produce constraints on the masses of the stars disrupted in these events. Proposed radiation transfer simulations to improve and expand upon these existing constraints are described in Chapter 6.

1.2.2 Dynamics of stellar orbits

There are many dynamical processes other than two-body relaxation that can move stars onto disrupting orbits, two-body relaxation is simply the most efficient at producing TDEs in an isolated spherical stellar cusp. For example, coherent perturbations from the orbits of stars in the cusp (Rauch & Tremaine 1996; Kocsis & Tremaine 2015), an eccentric stellar disk (Madigan et al. 2018; Wernke & Madigan 2019), or an external perturber such as a SMBH binary (e.g. Chen et al. 2011; Li et al. 2015) can all be significantly more efficient than two-body relaxation at moving stars onto disrupting orbits. In Chapter 5 we focus on the SMBH binary channel, and explore how TDEs can help us find hidden SMBH binaries.

TDE rates will be enhanced around both black holes in a SMBH binary, however flares from the smaller of the two black holes are particularly useful for alerting us to the presence of the binary. The potential of the cusp should be dominated by the larger black hole, and therefore dynamical mass measurements of the system will likely estimate a black hole mass close to the value of the primary (the uncertainty on most mass measurement methods is of order 0.3-0.5 dex, e.g. McConnell & Ma 2013; Xiao et al. 2011). However, if a star is disrupted by the smaller black hole, the timescale of its flare will be shorter than what would be expected from a disruption by the larger black

hole. In the most extreme case, if the larger black hole is $\gtrsim 10^8 M_\odot$, most stars will be disrupted inside its event horizon and any tidal disruption flare observed from the center of the galaxy would provide a strong indication of a SMBH binary (e.g. Coughlin & Armitage 2017). We discuss these possibilities in more detail in Chapter 5, where we calculate the rates of tidal disruption events for the smaller black hole in a SMBH binary to help determine their observability.

1.3 Outline of this work

Chapter 2 describes a light curve model for tidal disruption events, and uses it to fit a population of optical and UV TDE flares, constraining parameters of the system such as the masses of the black hole and star, and the impact parameter of disruption (β). Chapter 3 delves deeper into the analysis of the light curve model and TDE observations described in Chapter 2, with a focus on the energy release timescales and efficiencies measured for the light curves and their implications for the emission mechanism. Chapter 4 combines constraints from models of TDE light curves and spectra to put limits on the properties of disrupted stars, and compares the results to the expected stellar populations of the host galaxies. Chapter 5 models the dynamics of SMBH binaries and calculates the rates of tidal disruptions from the eccentric Kozai-Lidov mechanism. Finally, Chapter 6 summarizes the results of the previous chapters and also discusses possible follow-up studies to expand upon the work described in this thesis.

Chapter 2

Modeling the light curves of Tidal Disruption Events

2.1 Introduction

One of the most promising avenues for studying black holes in quiescent galaxies is through tidal disruption events (TDEs). Unlucky stars that pass too near a black hole are torn apart, lighting up previously dormant black holes (Rees 1988) and encoding the resultant light curves with a wealth of information about the nature of disruptor and disruptee. The initial disruption tests how stars behave under the presence of strong gravity (Kobayashi et al. 2004; Guillochon et al. 2009). The shape of the light curve includes clues about the mass and spin of the black hole (Evans & Kochanek 1989; Kesden 2012a; Cheng & Bogdanović 2014; Tejeda et al. 2017), as well as the properties of the star (Lodato et al. 2009; Haas et al. 2012; Law-Smith et al. 2017a), and the

mechanics of the disruption and accretion processes (Rosswog et al. 2009; Ayal et al. 2000; Bonnerot et al. 2016b).

For a TDE to be observable, the tidal disruption radius, $R_{\rm t} \equiv (M_{\rm h}/M_*)^{1/3} R_*$ of a star of mass M_* and radius R_* by a black hole of mass $M_{\rm h}$ must be outside the gravitational radius of the black hole (e.g. MacLeod et al. 2012), else the black hole will swallow the star whole. For most stars, black holes $\lesssim 10^8 M_\odot$ are the most likely disruptors. This makes TDEs all the more exciting, as they are probing lower mass black holes that are otherwise difficult to study, and whose mass determinations are uncertain.

The fallback rate and the peak timescale of TDEs are dependent on the mass of the disrupting black hole, the mass of the star, and the stellar structure of the star (Lodato et al. 2009; Guillochon & Ramirez-Ruiz 2013). Because the dependence on the mass and radius of the star largely cancel one another out on the main sequence, the peak timescale is sensitive to the mass of the black hole. Thus, if a TDE's luminosity follows the fallback rate (i.e. is "prompt" Guillochon & Ramirez-Ruiz 2015a), the light curve can be used to measure the black hole's mass and the properties of the disrupted star. In order for the luminosity to follow the fallback rate, the stellar debris that initially returns on highly eccentric orbits must circularize on a timescale that is shorter than the fallback timescale (Shiokawa et al. 2015; Bonnerot et al. 2016b; Hayasaki et al. 2016). As we show here, the optical and UV events that we modeled all require prompt circularization, suggesting that we can use their light curves to acquire reliable black hole mass measurements.

New TDEs have been uncovered at a steady rate in recent years and the rate of discoveries will continue to increase. As such, it has become imperative to be able to systematically quantify the key variables responsible for shaping TDE light curves so that we can compare these variables across events and develop a statistical understanding of the physical ingredients at play. To facilitate this, it is important for TDE data to be accessible, and the *Open TDE Catalog* (Auchettl et al. 2017; Guillochon et al. 2017b) is aiming to do this by collecting TDE data and hosting it online in a standardized format. To compare and contrast between different TDEs it is important to fit the events consistently, and to this end in this paper we introduce a theoretical model for fitting TDEs as part of `MOSFiT`, the modular Open-Source Fitter for Transients (Guillochon et al. 2017b). This model has been implemented in `MOSFiT` and is available immediately.

Along with the model we present fits to the optical and UV data of 14 TDEs from the *Open TDE Catalog*. Using `MOSFiT` we are able to extract posterior distributions for key parameters, most notably the black hole mass. We attempt to capture the broad features of a TDE while minimizing the number of free parameters in our model. Our model ingredients are outlined in Section 2.2.1 and our TDE sample is described in Section 2.3. Our black hole mass estimates are presented in Section 2.4 along with a detailed comparison with those derived using other methods. In Section 2.6 we discuss how the posteriors from our fits can help inform TDE emission models and presents a summary of our findings.

2.2 Method

The tidal disruption model in `MOSFiT` uses `FLASH` simulations of the mass fallback rate (Guillochon & Ramirez-Ruiz 2013) as inputs to fit data of TDEs. It is modeled similarly to `TDEFit`, a code for fitting tidal disruption events, originally described in Guillochon et al. (2014), but excludes a few features of that code that will be ported to future versions of the `MOSFiT` model (see Section 2.6.3). In the sections that follow we provide a detailed description of the model components along with a brief overview of the fitting procedure.

2.2.1 MOSFiT Modules

The `MOSFiT` platform sub-divides the components of a model into independent modules such that common operations for fitting transients can be utilized by various transient types. This means any new model implemented in `MOSFiT` re-uses many existing modules, reducing the chance of coding errors and improving overall performance. Below, we describe the new modules added to `MOSFiT` specifically created for modeling TDEs, which include new *engine* (source of radiant emission), *transform* (reprocessing of radiant emission), and *photosphere* (conversion of bolometric flux to a distribution of flux as a function of wavelength) modules.

Fallback Engine

The *engine* for the TDE model comes from converting the fallback rate of material onto the black hole post-disruption directly to a bolometric flux via a constant

Parameter	Prior	Min	Max
$M_{\rm h}(M_\odot)$	Log	10^5	5×10^8
b (scaled impact parameter[a])	Flat	0	2
$M_*(M_\odot)$	Kroupa	0.01	100
ϵ (efficiency)	Flat	0.005	0.4
$\rm R_{ph0}$ (photosphere power law constant)	Log	10^{-4}	10^4
l (photosphere power law exponent)	Flat	0	4
$t_{\rm first\ fallback}$ (days since first detection[bc])	Flat	-500	0
$T_{\rm viscous}$ (days)	Log	10^{-3}	10^5

[a]The parameter b is a proxy for β as the relationship between β and ΔM bound to the black hole differs for different γ. Minimum disruptions for both $\beta_{5/3}$ and $\beta_{4/3}$ correspond to $b = 0$ and full disruptions for both β correspond to $b = 1$. Disruptions with $b = 2$ correspond to $\beta_{5/3} = 2.5$ and $\beta_{4/3} = 4.0$ respectively.
[b]For our fit of iPTF16fnl we narrowed the range of $t_{\rm disruption}$ as `MOSFiT` was having difficulty isolating the relatively short peak for that event, it is clear from the photometry that $t_{\rm first\ fallback}$ is $\ll 500$ days before the first observation.
[c]The parameter $t_{\rm first\ fallback}$ is different from the time of disruption. For any combination of disruption parameters (β, γ) there exists a fixed time between $t_{\rm disruption}$ and $t_{\rm first\ fallback}$. This delay can be affected by the precession of debris out of the original orbital plane, however it does not affect the determination of M_h because the mass-energy distribution remains intact during this delay (see Section 2.6.1).

Table 2.1: Here we list the parameters and priors used in our model. Where the listed prior is 'Log', the natural logarithm was used.

efficiency parameter ϵ. To model this process we used hydrodynamical simulations of polytropic stars tidally disrupted by supermassive black holes (SMBHs) (Guillochon & Ramirez-Ruiz 2013). Polytropic stars are stars whose equation of state is defined by $P \propto \rho^\gamma$. The parameter γ is the polytropic index – colloquially the 'polytrope.' Stars of different masses are better represented by different polytropes, we take stars with mass $\leq 0.3 M_\odot$ and mass $\geq 22 M_\odot$ to be represented by 5/3 polytropes ($\gamma = 5/3$) while stars with masses between $1 M_\odot$ and 15 $M_\odot$ are modeled as 4/3 polytropes ($\gamma = 4/3$). For stars in the transition ranges ($0.3 M_\odot$ – $1 M_\odot$, $15 M_\odot$ – $22 M_\odot$), we use hybrid fallback functions that smoothly blend between the 4/3 and 5/3 polytopes, the details of which are described later in this section. The simulations were run for a wide range of impact

parameters ($\beta = R_{\rm t}/R_{\rm p}$, $R_{\rm p}$ is the pericenter radius), varying from interactions that barely disrupted the star to interactions with β values significantly larger than what is needed for full disruption. Stars are considered to be fully disrupted when no surviving core remains post-disruption, which for SMBH encounters yields a fallback mass $\Delta M = M_*/2$. Because both the mass of the black hole and the mass of the star enter into the rate of fallback as simple scaling parameters (Guillochon & Ramirez-Ruiz 2013, 2015b), all simulations were run with $M_{\rm h} = 10^6 M_\odot$ and $M_* = 1 M_\odot$.

The hydrodynamical simulations provide us with the distribution of debris mass dm/de as a function of specific binding energy e after it is torn apart. This distribution is dependent on the structure of the star, a feature that is particularly important when fitting the shape of the light curve and its power-law decline at late times. To obtain the fallback rate $dm/dt = \dot{M}$, dm/de is converted into a mass distribution in time using de/dt calculated from keplerian orbital dynamics,

$$T = \frac{\pi\mu}{\sqrt{2}}(-e)^{-3/2} \tag{2.1}$$

$$de/dt = \frac{(2\pi\mu)^{2/3}}{3t^{5/3}}. \tag{2.2}$$

In the above equations, e is the specific orbital energy, μ is the standard gravitational parameter, and T is the orbital period of the bound debris that falls back onto the black hole.

Our model assumes that stars meet black holes on approximately zero-energy

(parabolic) orbits, as is true for most tidal disruptions in galactic nuclei. This means that the energy of the bound stellar debris is only dependent on the potential of the SMBH. Using this simplification and taking a Taylor expansion of the potential of the SMBH at the surface of the star at the pericenter of the orbit, one finds

$$e \propto \frac{GM_{\rm h}R_*}{R_t^2} \propto M_{\rm h}^{1/3} M_*^{2/3} R_*^{-1}. \tag{2.3}$$

The mass-energy distribution is related to the black hole mass and specific binding energy through $dm/de \propto M_{\rm h}/2e$ when the ratio of the black hole's mass to the star's mass is large (Rees 1988; Phinney 1989). Substituting Equation 2.3 into Equation 2.1 gives us the dependence between the timescale and the properties of the star and the black hole; $t \propto M_h^{1/2} M_*^{-1} R_*^{3/2}$. Using this relation together with Equation 2.2, we find that $de/dt \propto M_h^{-1/6} M_*^{5/3} R_*^{-5/2}$ and therefore $dm/dt = dm/de \times de/dt \propto M_h^{-1/2} M_*^2 R_*^{-3/2}$. To summarize, the following relations relate the parameters of the star and black hole to the mass fallback rate,

$$\dot{M} \propto M_h^{-1/2} M_*^2 R_*^{-3/2}, \tag{2.4}$$

$$t(\dot{M}) \propto M_h^{1/2} M_*^{-1} R_*^{3/2}. \tag{2.5}$$

Here we use $\dot{M}$ to denote the fallback rate, so $t(\dot{M})$ is the time of a given fallback rate. We will continue to use this notation throughout the rest of the paper.

After collecting $\dot{M}$ for various values of β and γ, values for β, M_* and $M_{\rm h}$ are input into the *fallback* module, which linearly interpolates in β-M_* space (using the

mapping between M_* and γ described above) to obtain fallback curves as a functions of both parameters. In order to provide accurate description for the light curve with M_* and $M_{\rm h}$, we make use of the following scalings given in Equation 2.4 and Equation 2.5.

We use Tout et al. (1996) to get R_* from M_* for $M_* \geq 0.1 M_\odot$. Below that mass we assume that the radius is constant and use $R_{*,\rm Tout}(M_* = 0.1 M_\odot) \approx 0.1 R_\odot$, roughly the radius of Jupiter.

We also assume the stars are zero-age main-sequence stars (ZAMS) and that they have solar metallicity. Both the ZAMS and composition assumption as well as the assumption that the stars are represented by blends of 4/3 and 5/3 polytropes are simplifying assumptions that allow us to build this minimal model without introducing excessive numbers of free parameters. In future work we plan to use simulations of realistic stars for a wide range of ages and compositions as inputs into our fallback module (Law-Smith et al. 2017a).

At the end of the fallback module, we convert $\dot{M}$ to luminosity by assuming a constant efficiency ϵ, which we allow to vary as a free parameter in our fitting procedure, yielding $L = \epsilon \dot{M} c^2$. This freedom allows us to remain agnostic about the physical mechanism driving this conversion, which can be sub-percent if originating from a stream-stream collision (Jiang et al. 2016b) or up to 42% if the conversion occurs at the ISCO of a maximally-spinning black hole (Beloborodov 1999). We also introduce a soft cut at the Eddington limit $L_{\rm Edd} \equiv 4\pi G M_{\rm h} c/\kappa$ to prevent the radiated luminosity from exceeding this value (here κ is the mean opacity to Thomson scattering assuming solar metallicity). This is motivated by both the fact that the peak bolometric luminosi-

ties derived observationally for optical/UV TDEs appear to be sub-Eddington (Hung et al. 2017; Wevers et al. 2017) and that other accreting black hole systems (such as AGN) rarely show evidence for large thermal Eddington luminosity excesses.

Viscous Delay

The assumption that the luminosity closely follows the fallback rate is a bold assertion that, if correct, gives us a deterministic way to relate how stellar debris circularizes and how it accretes onto the black hole. We define a 'viscous time' in this work, which encompasses the effects of time delays due to the circularization process as well as delays due to accretion through the disk surrounding the black hole. If the viscous time about the black hole were short as compared to the fallback time, the accretion rate onto the black hole from the forming disk $\dot{M}_{\rm d}$ should be equal to the fallback rate $\dot{M}_{\rm fb}$. It is likely that once debris reaches the disk the time it will take to accrete onto the black hole will be much shorter than the fallback time. The orbital timescale at the edge of the disk ($\sim 2R_{\rm p}$) is much smaller than the original orbital timescales of the debris (Equation (2.1)), and therefore viscous processes in the disk have many (disk) orbital timescales over which to move debris inward. However, as has been found in several numerical works (Guillochon et al. 2014; Shiokawa et al. 2015; Bonnerot et al. 2016b; Hayasaki et al. 2016), circularization about the black hole might be very ineffective, resulting in viscous times that are potentially hundreds of times longer than the orbital period of the most-bound debris (Cannizzo et al. 1990; Guillochon & Ramirez-Ruiz 2015a; Dai et al. 2015). This would result in a central accretion disk with $R \approx 2R_{\rm p}$ that is starved of mass, with much of the mass being held aloft for long periods of time

in an elliptical superstructure (Ramirez-Ruiz & Rosswog 2009; Guillochon et al. 2014). While the exact details of how matter is received by the disk and then later accreted by the black hole remain elusive (Sądowski et al. 2016), the primary effect of the viscous slow-down is likely well-approximated as a "low-pass" filter on the fallback rate,

$$\dot{M}_{\rm d}(t) = \dot{M}_{\rm fb}(t) - M_{\rm d}(t)/T_{\rm viscous}, \tag{2.6}$$

where the elliptical disk that forms acts as a reservoir where a mass $M_{\rm d}$ remains suspended outside of the black hole's horizon for roughly a viscous time. The solution to this expression is

$$\dot{M}_{\rm d}(t) = \frac{1}{T_{\rm viscous}}\left(e^{-t/T_{\rm viscous}} \int_0^t e^{t'/T_{\rm viscous}} \dot{M}_{\rm fb}(t')dt'\right), \tag{2.7}$$

which shows that the accretion rate exponentially approaches the fallback rate after a viscous time. We implement the above expression in our viscous module, inputting the luminosities from our fallback module through the transform, which yields viscously-delayed luminosities that are used to compute light curves.

Photosphere

Regardless of the process or combination of processes responsible for generating the emission, the kinetic energy of the returning debris must eventually be dissipated in order to be observed. Even if some energy is deposited by circularization at large distances (Piran et al. 2015), the energy will be primarily dissipated by processes that

operate closest to the black hole simply because the velocities there are the greatest. However, this would imply most of the radiation would be emitted at very high energies (X-rays), and instead we observe many TDEs with significant (and sometimes dominant) optical/UV flux. A reprocessing layer, either static or outflowing (Miller 2015; Metzger & Stone 2016), can help explain the observed emission by reprocessing the luminosity generated by the various dissipation processes at play (Loeb & Ulmer 1997; Ulmer et al. 1998; Bogdanović et al. 2004; Guillochon et al. 2014; Jiang et al. 2016b; Coughlin & Begelman 2014; Strubbe & Quataert 2009). The reprocessing of the radiation has also been used to successfully explain the line ratios observed in PS1-10jh (Roth et al. 2016; Gaskell & Rojas Lobos 2014). In this work we assume a simple blackbody photosphere for the reprocessing layer, so that the observed flux becomes

$$F_\nu = \frac{2\pi h\nu^3}{c^2} \frac{1}{\exp(h\nu/kT_{\rm eff}) - 1} \frac{R_{\rm phot}^2}{D^2}, \tag{2.8}$$

with an effective blackbody temperature

$$T_{\rm eff} = \left(\frac{L}{4\pi\sigma_{\rm SB} R_{\rm phot}^2} \right)^{1/4}. \tag{2.9}$$

In the above equations, F_ν is the specific flux, $R_{\rm phot}$ is the photospheric radius, D is the distance from the source, L is the bolometric luminosity from our fit, and $T_{\rm eff}$ is the temperature of the photosphere. Most observations of TDEs have thermal temperatures that don't exhibit significant variation. For blackbody emission, the radius must increase as the luminosity (and $\dot{M}_{\rm fb}$) increase, and decrease as the luminosity decreases, in order

for the temperature not to change significantly as the luminosity evolves. This simple behavior also explains the rise in temperatures at late times as the photospheric radius decreases and the bulk of the observed radiation shifts to higher energies. To model this dependence we assume that the radius of the photosphere has a power law dependence on the luminosity and fit for both the power law exponent l and radius normalization $R_{\rm ph0}$,

$$R_{\rm phot} = R_{\rm ph0} a_p (L/L_{\rm edd})^l. \tag{2.10}$$

Here $a_{\rm p}$ is the semi-major axis of the accreting mass at peak $\dot{M}_{\rm fb}$. This provides a reasonable typical scaling for the radius of the photosphere, with a minimum photosphere size set by $R_{\rm isco}$ and a maximum photosphere size set by the semi-major axis of the accreting mass.

One of the appealing aspects of this photosphere model is that it remains agnostic towards the mechanism ultimately responsible for generating the luminosity, but does make a number of simplifying assumptions regarding the source function of the radiation. In particular, it assumes that all of the radiation is efficiently thermalized at the scale of the photosphere radius. The resultant spectrum is compatible with what one would expect from a "veiled" TDE (Auchettl et al. 2017), and, as such, this model cannot reproduce the x-ray emission that is observed in a small fraction of TDEs found in optical surveys (e.g. ASASSN-14li, Miller et al. 2015). In the future, we plan to include an accretion disk module which will be used to describe the x-ray emission that sometimes is observed to accompany optical/UV TDEs (Auchettl et al. 2017).

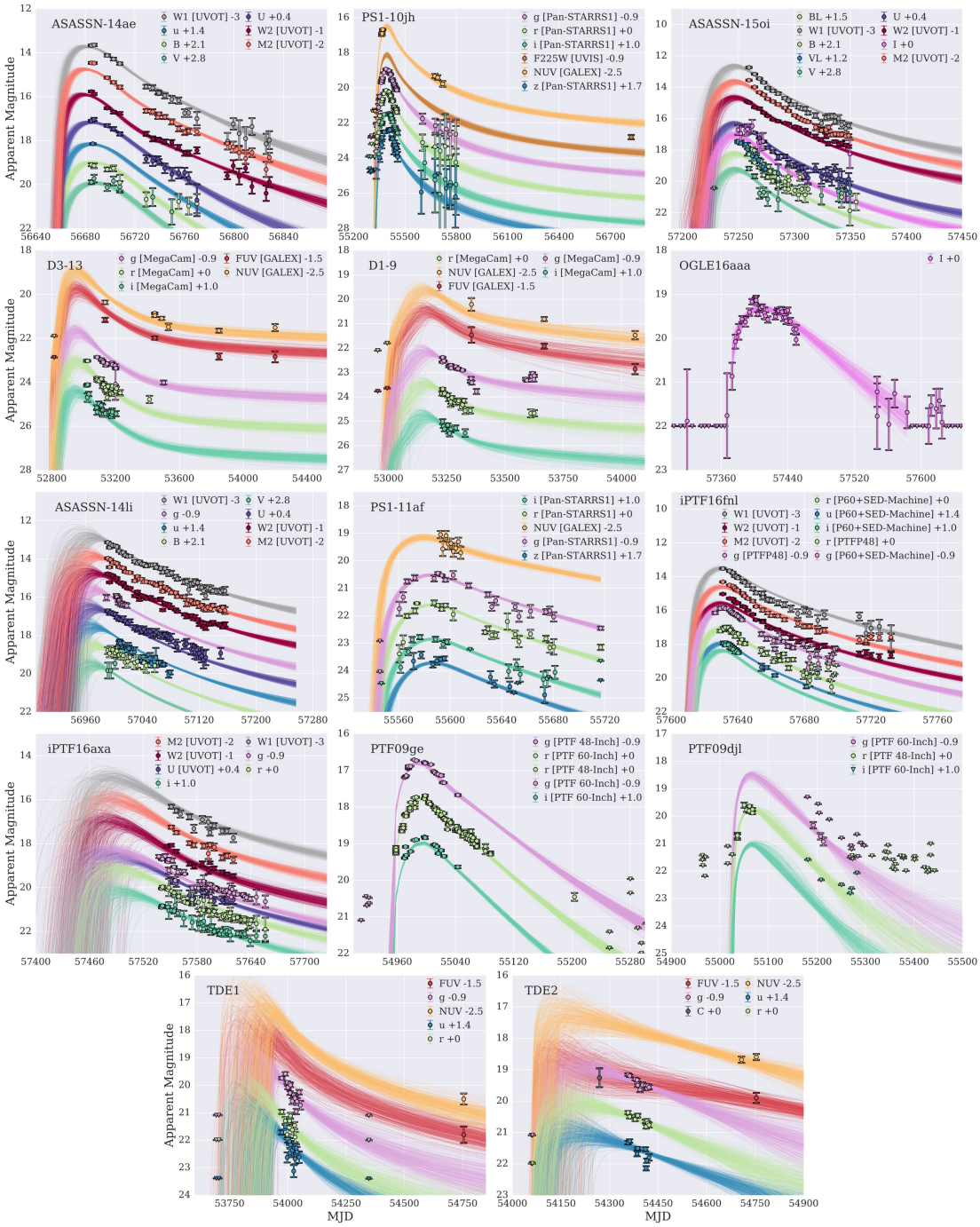

Figure 2.1: Ensembles of TDE light curves each constructed from the posterior parameter distribution. The multicolor detections and associated upper limits are plotted for all selected TDEs.

2.3 Light Curve Fits

The characteristics of the population of TDEs as a whole can be derived by fitting a significant fraction of the existing TDE candidates to a shared model. In what follows we describe the data used in this study as well as the results from the fitting procedure.

2.3.1 Data Selection

The data from our fits is public and can be found on the Open TDE Catalog[1]. There does not exist a single agreed upon test for classifying a transient as a TDE, and therefore multiple clues must be taken together to determine the likelihood that a transient is in fact the result of a TDE. First of all, astrometry must place the transient near the center of its host galaxy. Next, unique light curve features (blue optical/UV colors, minimal color evolution, and a large brightening above the quiescent level) are used to separate TDEs from other transients occurring in the cores of galaxies such as AGN flares (e.g., Gezari et al. 2009). Spectra of the events, in particular transient broad features of hydrogen and helium (Arcavi et al. 2014), are also used to separate the events from other phenomena, particularly supernovae. Finally, we theoretically expect the bolometric light curves to have a power law decline at late times (Rees 1988; Lodato 2012; Guillochon & Ramirez-Ruiz 2013), as opposed to an exponential decline that might be better associated with nuclear decay and thus a supernova origin.

In selecting data we were limited by the confines of our current model. For example, we currently do not fit x-ray radiation, and therefore we required events in

[1] https://tde.space

our sample to have bolometric luminosities dominated by emission in the optical/UV. In addition to this, our current model can only reproduce light curves with a single temporal component, and we are thus unable to fit events such as ASASSN-15lh that have a significant late time re-brightening that might arise from an emerging accretion disk (Margutti et al. 2017). From this subset of TDEs we first chose events which had either observations of the light curve peak or near-peak early time upper limits. The peak timescale of most TDEs is $\lesssim$ 1 year, therefore we defined near-peak upper limits to be within 1 year of the first observed data point. All of the TDEs in our sample except iPTF16axa, TDE1 and TDE2 fall into this category. We additionally included events with detailed observations of the decline ($\geq$ 3 data points in each band over the course of a peak timescale) in at least three optical/UV bands, even if these events did not have peak observations or near-peak upper limits (such as iPTF16axa, TDE1 and TDE2). With sufficient color information, `MOSFiT` is able to constrain the bolometric luminosity curve and therefore also the peak timescale.

Here we include a list of the events we fit: PS1-10jh (Gezari et al. 2012; Gezari et al. 2015), PS1-11af (Chornock et al. 2014), PTF09djl (Arcavi et al. 2014), PTF09ge (Arcavi et al. 2014), iPTF16fnl (Blagorodnova et al. 2017; Brown et al. 2018), iPTF16axa (Hung et al. 2017), ASASSN-14li (Holoien et al. 2016b; Brown et al. 2017), ASASSN-15oi (Holoien et al. 2016a), ASASSN-14ae (Holoien et al. 2014; Brown et al. 2016), OGLE16aaa (Wyrzykowski et al. 2017), D1-9 (Gezari et al. 2008), D3-13 (Gezari et al. 2008), TDE1 (van Velzen et al. 2011), and TDE2 (van Velzen et al. 2011).

2.3.2 Fitting Procedure

`MOSFiT` currently uses a variant of the `emcee` ensemble-based MCMC routine (Foreman-Mackey et al. 2013) to find the combinations of parameters that yield the highest likelihood matches for a given input model (Guillochon et al. 2017a), where model errors are fitted simultaneously with model parameters by the variance parameter σ. To quantify how well the various combinations of parameters in the model fit each light curve, `MOSFiT` uses the Watanabe-Akaike information criteria (Watanabe 2010) (WAIC), also known as the widely applicable Bayesian criteria. This is used in place of the total evidence of the model: for objective functions where the likelihood function is not analytic and separable (such as in this semi-analytic model), it is difficult to evaluate the evidence exactly. While the WAIC score does not directly scale with the evidence, it is correlated with it, and can be used to rank fits between models (see Section 7 of Gelman et al. 2014). The WAIC is evaluated as follows,

$$\mathrm{WAIC} = \overline{\log\, p_n} - \mathrm{var}(\log\, p_n), \tag{2.11}$$

where $\overline{p_n}$ is the mean log likelihood score and $\mathrm{var}(\log\, p_n)$ its variance.

In addition to measuring the goodness of fit, it is important to ascertain whether or not a fit has converged. To this end, we use the Gelman-Rubin metric, or Potential Scale Reduction Factor (PSRF, signified with $\hat{R}$) to gauge convergence (Gelman & Rubin 1992). This metric measures how well mixed each individual chain is as well as the degree of mixture between the different chains (for the definition, see Guillochon et al. 2017a).

For this multi-parameter model we used the maximum of the PSRFs computed for each parameter, so that the convergence of each fit was determined by the parameter with the slowest convergence. We attempted to run all of our fits until they reached a PSRF ≤ 1.2 (ensuring that the walkers are well-mixed within the regions of convergence (Brooks & Gelman 1998), however this was not possible for every fit. The 4 events with PSRF > 1.2 were refit multiple times, and continued to converge to the solutions we present here. For the work presented in this paper a minimum of 200 walkers and 30,000 iterations were used to recover the distribution of model fits.

2.3.3 Results

We show the results of the light curve fits in Figure 2.1, the best fit parameter values in Table 2.2, and the posterior distributions of the walkers in Figure 2.2. In Figure 2.1, the ensemble of light curves from the final walker positions are plotted. Although the model priors allow for long viscous times, the light curves of highest likelihood continue to closely follow the fallback rates. The viscous timescales and $t_{\rm peak}$ values are shown in Table 2.2. The preferred viscous delays are less than 1% of $t_{\rm peak}$ for all events modeled in this work; this preference is visible in the first column of panel plots in Figure 2.2. The minimal viscous delay of these events allows us to obtain precise black hole mass measurements as the luminosity evolution is still best described using the fallback rate, and the primary dependence of $t_{\rm peak}$ is upon $M_{\rm h}$ (as shown in Equation (2.5)).

In the absence of good photometry around peak, early time upper limits can help constrain the peak timescale and therefore the corresponding black hole mass, as

shown in the plots for events D1-9, D3-13, PTF09djl, ASASSN-14li, ASASSN-15oi and ASASSN-14ae. For events without early time information or near-peak upper limits we can still fit the data if there is detailed observations (in multiple bands) of the decline. The mass fallback rate and bolometric luminosity do not decline with a constant power law, and this helps `MOSFiT` find fits to events with well-sampled photometry but without early time data. Good band coverage allows `MOSFiT` to accurately pin down different sections of the SED and more accurately measure the bolometric luminosity. It also makes it possible to constrain the photosphere parameters R_{ph0} and l (the power law constant and exponent, as defined in Equation (2.10)).

For example, our initial fit to ASASSN-15oi was completed before we realized there existed an early time upper limit, however the black hole mass we measure with the addition of that upper limit is the same as what we found without it. The other parameters similarly maintained their previously measured values, the upper limit simply reduced the uncertainty in the measurements.

The light curves of the majority of the events in this sample have one clear peak and monotonically decrease afterwards, as is predicted by our current single-component model. These include PS1-10jh, PS1-11af, PTF09ge, PTF09djl, ASASSN-14ae, OGLE16aaa, D3-13, D1-9, iPTF16axa, and iPTF16fnl. These events are also seen to radiate most of their bolometric luminosity at UV/optical wavelengths. They resemble veiled TDEs, in which the accretion disk is likely obscured by an optically thick photosphere or wind (Auchettl et al. 2017). However, there are a few TDEs in this sample (ASASSN-14li, ASASSN-15oi) whose x-ray emission and late time light curves

are not as well described by our current single-component model and likely require a secondary component to explain their late-time behavior.

As shown in Figure 2.8, the radius of the reprocessing layer in our model decreases at late times. Once the photosphere has receded to the size of the accretion disk, we expect higher energy photons to start contributing and ultimately dominating the light curve. As the luminosity decreases, the radiation from the accretion disk is expected to soften, potentially shifting the peak of the emission back into the UV/optical bands. At the same time, as the photosphere recedes, less x-rays from the accretion disk are expected to be reprocessed, allowing us to observe them. These additional late-time components can change the decline of the light curve. Of this sample, it is possible that for ASASSN-14li (Brown et al. 2018), and ASASSN-15oi (Gezari et al. 2017) these additional components play a role in their late time light curves.

Although we did not model the origin of x-ray emission in this work, ASASSN-14li shows significant energy emitted at these wavelengths, which could be explained by the presence of a partially obscured accretion disk. In addition to this, the late time data shows that the decline of the UV light curve slows and the UV luminosity remains fairly constant from $\sim$ 350 days after discovery to the final observations at $\sim$ 600 days after discovery (Brown et al. 2018) (the late time host-subtracted data was not available at the time of this study and therefore we did not fit it). Similarly, new late time observations of ASASSN-15oi from $\sim$ 250 days after discovery show flat optical/UV luminosities. ASASSN-15oi also exhibits an increasing x-ray component during the same time period (Gezari et al. 2017; Holoien et al. 2018a). When we attempted to fit ASASSN-15oi's

late time optical and UV data with our model we found the quality of the fit worsened significantly, with the WAIC score dropping from 73 to 17. Therefore the fit we present here does not include the late time component of the light curve. Another potential example of a two-component TDE in the literature is ASASSN-15lh (Nicholls et al. 2015; Leloudas et al. 2016). If ASASSN-15lh is indeed a TDE, then it requires a secondary late time component to explain the behavior of its light curve.

TDE	$M_{\rm h}$ ($10^6 M_\odot$)	β	M_* ($M_\odot$)	γ	ϵ	$\log_{10}(\mathrm{R_{ph0}})$	l	$t_{\rm peak}$ (days)	$T_{\rm viscous}$ (days)	σ	WAIC	PSRF	Source
10jh	17^{+2}_{-1}	$0.899^{+0.006}_{-0.005}$	$0.101^{+0.002}_{-0.002}$	5/3	$0.09^{+0.03}_{-0.02}$	$0.8^{+0.1}_{-0.1}$	$1.4^{+0.1}_{-0.1}$	110^{+7}_{-2}	$0.08^{+0.85}_{-0.08}$	$0.11^{+0.01}_{-0.01}$	200	1.10	1, 2
11af	$3.7^{+0.5}_{-0.4}$	$0.90^{+0.03}_{-0.01}$	$0.101^{+0.009}_{-0.003}$	5/3	$0.020^{+0.005}_{-0.003}$	$1.4^{+0.1}_{-0.1}$	$1.4^{+0.1}_{-0.1}$	54^{+3}_{-3}	$0.2^{+1.4}_{-0.2}$	$0.06^{+0.01}_{-0.01}$	231	1.07	3
09djl	$2.6^{+1.0}_{-0.5}$	$0.86^{+0.06}_{-0.09}$	$0.11^{+0.13}_{-0.02}$	5/3	$0.1^{+0.1}_{-0.1}$	$1.1^{+0.8}_{-0.4}$	$2.1^{+0.8}_{-0.4}$	54^{+10}_{-7}	$0.2^{+2.9}_{-0.2}$	$0.01^{+0.02}_{-0.01}$	120	1.25	4
09ge	$3.6^{+0.8}_{-0.5}$	$1.1^{+0.1}_{-0.3}$	$0.10^{+0.07}_{-0.01}$	5/3	$0.008^{+0.003}_{-0.002}$	$3.5^{+0.2}_{-0.2}$	$1.97^{+0.10}_{-0.09}$	59^{+14}_{-4}	$0.04^{+0.58}_{-0.04}$	$0.09^{+0.01}_{-0.01}$	94	1.81	4
16fnl	$1.7^{+0.2}_{-0.2}$	$0.91^{+0.05}_{-0.02}$	$0.101^{+0.008}_{-0.004}$	5/3	$0.007^{+0.002}_{-0.002}$	$1.0^{+0.1}_{-0.1}$	$1.7^{+0.1}_{-0.1}$	37^{+2}_{-2}	$0.04^{+0.32}_{-0.04}$	$0.21^{+0.01}_{-0.02}$	142	1.12	5, 6
16axa	$2.5^{+1.3}_{-0.9}$	$0.94^{+0.08}_{-0.07}$	$1.0^{+0.8}_{-0.2}$	4/3	$0.02^{+0.03}_{-0.01}$	$0.8^{+0.2}_{-0.2}$	$0.6^{+0.1}_{-0.1}$	62^{+13}_{-9}	$0.2^{+3.4}_{-0.2}$	$0.21^{+0.02}_{-0.01}$	139	1.32	7
14li	9^{+2}_{-3}	$0.90^{+0.15}_{-0.04}$	$0.2^{+0.1}_{-0.1}$	5/3	$0.2^{+0.1}_{-0.1}$	$-0.2^{+0.2}_{-0.1}$	$1.9^{+0.4}_{-0.3}$	95^{+14}_{-15}	$0.1^{+2.1}_{-0.1}$	$0.14^{+0.01}_{-0.01}$	283	1.11	8
15oi	4^{+1}_{-1}	$0.91^{+0.06}_{-0.02}$	$0.11^{+0.04}_{-0.01}$	5/3	$0.018^{+0.010}_{-0.005}$	$1.3^{+0.3}_{-0.2}$	$2.1^{+0.1}_{-0.2}$	60^{+8}_{-7}	$0.04^{+0.53}_{-0.04}$	$0.20^{+0.02}_{-0.02}$	73	1.10	9
14ae	$1.3^{+0.1}_{-0.1}$	$1.04^{+0.03}_{-0.06}$	$1.00^{+0.02}_{-0.02}$	4/3	$0.006^{+0.003}_{-0.001}$	$1.8^{+0.1}_{-0.1}$	$1.3^{+0.1}_{-0.1}$	37^{+3}_{-2}	$0.05^{+0.52}_{-0.05}$	$0.12^{+0.02}_{-0.01}$	97	1.06	10
16aaa	$3.0^{+1.2}_{-0.8}$	$0.81^{+0.10}_{-0.09}$	$0.2^{+0.2}_{-0.1}$	5/3	$0.2^{+0.2}_{-0.1}$	$1.3^{+0.7}_{-0.6}$	$1.7^{+0.6}_{-0.4}$	67^{+13}_{-13}	$0.1^{+2.3}_{-0.1}$	$0.11^{+0.03}_{-0.02}$	38	1.16	11
D1-9	66^{+7}_{-10}	$1.2^{+0.2}_{-0.2}$	7^{+5}_{-3}	4/3	$0.11^{+0.16}_{-0.07}$	$-0.5^{+1.0}_{-0.8}$	$3.4^{+0.4}_{-0.8}$	212^{+42}_{-33}	$0.1^{+2.4}_{-0.1}$	$0.24^{+0.11}_{-0.06}$	96	1.44	12
D3-13	30^{+3}_{-3}	$1.8^{+0.1}_{-0.8}$	7^{+17}_{-4}	4/3	$0.2^{+0.1}_{-0.1}$	$-1.2^{+0.1}_{-0.1}$	$3.8^{+0.2}_{-0.4}$	131^{+71}_{-11}	$0.1^{+3.3}_{-0.1}$	$0.27^{+0.03}_{-0.03}$	37	1.10	12
TDE1	3^{+3}_{-1}	$0.84^{+0.13}_{-0.08}$	$0.1^{+0.3}_{-0.1}$	5/3	$0.2^{+0.2}_{-0.1}$	$0.2^{+0.3}_{-0.3}$	$0.7^{+0.3}_{-0.2}$	76^{+45}_{-25}	$0.2^{+5.8}_{-0.2}$	$0.20^{+0.03}_{-0.03}$	38	1.16	13
TDE2	$1.9^{+1.4}_{-0.6}$	$1.0^{+0.3}_{-0.1}$	$0.3^{+0.3}_{-0.1}$	5/3	$0.2^{+0.1}_{-0.1}$	$0.8^{+0.1}_{-0.2}$	$1.5^{+0.9}_{-0.5}$	50^{+36}_{-12}	$0.2^{+9.4}_{-0.2}$	$0.12^{+0.02}_{-0.02}$	53	1.19	13

[1]Gezari et al. (2012), [2]Gezari et al. (2015), [3]Chornock et al. (2014), [4]Arcavi et al. (2014), [5]Blagorodnova et al. (2017), [6]Brown et al. (2018), [7]Hung et al. (2017), [8]Holoien et al. (2016b), [9]Holoien et al. (2016a), [10]Holoien et al. (2014), [11]Wyrzykowski et al. (2017),[12]Gezari et al. (2008), [13]van Velzen et al. (2011)

Table 2.2: Here we list best fit parameters for all light curves with 1σ error bars.

parameter	error	scale
$M_{\rm h}$	± 0.2	$\log_{10}$
β	± 0.35	linear
M_*	± 0.66	$\log_{10}$
ϵ	± 0.68	$\log_{10}$
$R_{\rm ph0}$	± 0.4	$\log_{10}$
l	± 0.2	linear
$t_{\rm peak}$	± 15	linear
$T_{\rm viscous}$	± 0.10	$\log_{10}$

Table 2.3: We present estimates of the systematic error in each parameter. These estimates were obtained by running fits with an additional variable parameterizing the uncertainty in the mass-radius relation of the disrupted stars, and comparing the results to our original measurements. This mass-radius relation is likely our largest source of systematic error in measuring the mass of the black hole.

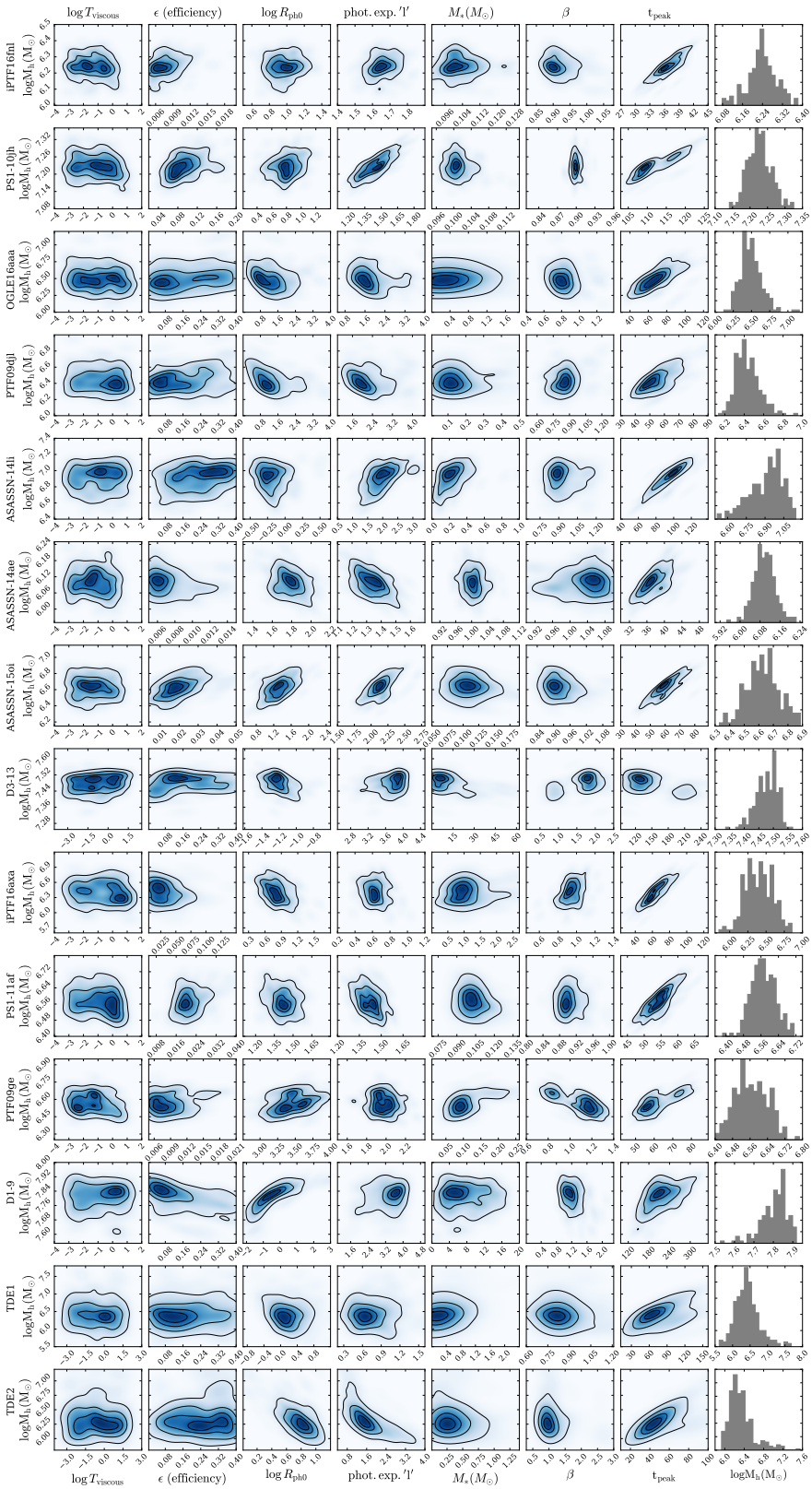

Figure 2.2: Caption on following page.

Figure 2.2: Posterior distributions of model parameters in the fit for each event as a function of $M_{\rm h}$. All logarithms are base 10. We include 0.5, 1, 1.5 and 2σ contours for the 2-dimensional distributions – these correspond to where 0.1175, 0.393, 0.675, and 0.865 of the 2D volume is contained. The plot shows that, for most events, $t_{\rm peak}$ (not itself a model parameter) correlates strongly with $M_{\rm h}$.

2.4 Black hole mass predictions

As discussed in the previous section, events with well-observed peaks and data in multiple bands have well-constrained black hole masses. The distributions of black hole masses for each event are shown in the last column of Figure 2.2, and the 68% confidence intervals are listed in Table 2.2. Figure 2.2 shows 2D histograms of all parameters plotted against black hole mass in order to see correlations between the different variables. The most obvious and consistent correlation is between the black hole mass and the time of peak. Nevertheless, we might expect other parameters to be mildly correlated with black hole mass as well. For example, the efficiency (ϵ), β, and the star mass all enter into the peak luminosity scaling relation with $M_{\rm h}$. However, when looking at columns 2, 5 and 6 in Figure 2.2, we see that none of these variables have a clear correlation with black hole mass–perhaps their combined influence dilutes their individual correlations with $M_{\rm h}$.

The masses of the black holes we fit are all inferred by other mass estimation methods to be between 10^5 and 10^8 solar masses. In Figure 2.3 we compare our results to mass measurements of the central black holes in the corresponding host galaxies using standard methods, and we find consistent results within reasonable errors (see Figure 2.5 for additional comparison with literature values). In this mass range, both the $M_{\rm h} - \sigma$ and $M_{\rm h} - L_{\rm bulge}$ relations suffer from significant uncertainty (see Section 2.5), therefore it is not surprising that masses derived using different scaling relations do not always agree within quoted errors. This makes the construction of an independent method even more valuable. We do note that our method results in systematically higher black hole

masses than the $M - \sigma$ relation. As we argue in Section 2.6, this provides a consistent picture on the nature of TDEs in which prompt flares, those that circularized quickly, are expected to be more frequent for higher mass black holes.

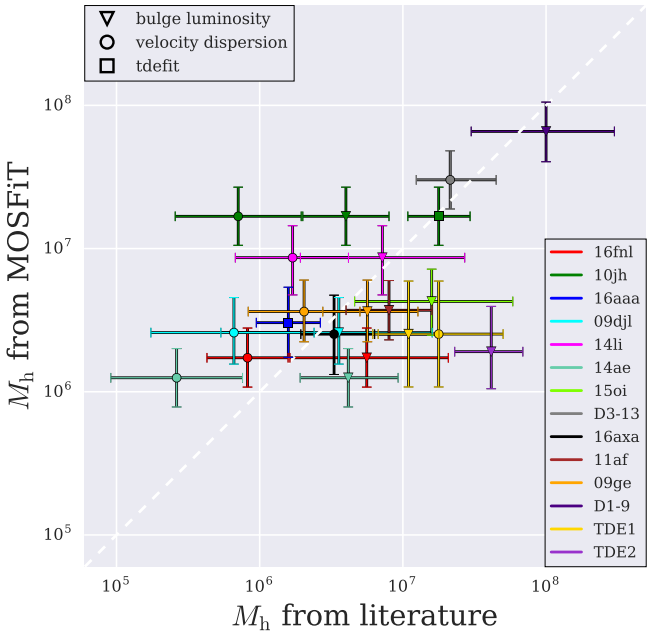

Figure 2.3: Comparison between the black hole mass estimates we derive from our model fits and those derived using the bulk properties of the host galaxy. The M_h measurements from galactic properties come from the following sources: Arcavi et al. (2014); Blagorodnova et al. (2017); Brown et al. (2018); Chornock et al. (2014); Gezari et al. (2008); Guillochon et al. (2014); Holoien et al. (2014, 2016b,a); Hung et al. (2017); Mendel et al. (2014); van Velzen et al. (2011); Wevers et al. (2017); Wyrzykowski et al. (2017). Measurements are averaged and errors are added in quadrature where multiple measurements using the same method exist for a single black hole. `MOSFiT` error measurements include systematic error, literature error measurements include the intrinsic scatter in the relevant relation.

The error bars from `MOSFiT`'s measurements of black hole masses in Figure 2.3 are quite small. Although `MOSFiT` marginalizes over the errors in all of our model's free parameters, it is likely that we are underestimating the total error because our model provides a simple approximation of a complicated physical phenomenon. For example,

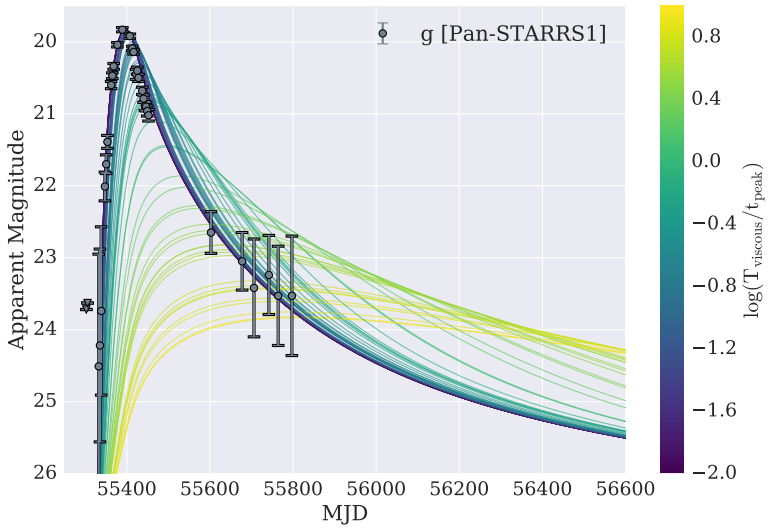

Figure 2.4: Example of the effect of a viscous delay on a TDE light curve. The plot shows g-band light curves for PS1-10jh with all parameters but the viscous time set to the best fit values (g-band is shown because it had good coverage over most of the light curve – all other bands are similarly affected). The best fit light curves are those with no noticeable viscous delays. The plot also shows that $T_{\rm viscous}/t_{\rm peak} \lesssim 0.1$ yields a light curve that is essentially identical to the case with no viscous delay. There were no viscous delays $\gtrsim 10$ days or $\gtrsim 10\%$ of the peak timescale derived in any of the presented fits.

changing the models for the disrupted stars from ZAMS polytropes with solar composition to more realistic MESA models will prevent the stellar mass of the disrupted star from being uniquely determined without additional knowledge about its evolutionary stage (and through that its radius). This will in turn affect the determination of the peak luminosity and peak timescale, allowing for those parameters to vary more and increasing the uncertainty in the black hole mass. We have accounted for this uncertainty in our systematic errors. Our systematic errors are listed in Table 2.3 and discussed in the following section.

2.4.1 Influence of stellar properties

The peak timescale of a TDE is primarily determined by the mass of the black hole, and by the mass and radius of the star. As described in Section 2.1, the effects of the mass and radius for a zero-age, solar metallicity star largely cancel out, allowing the peak timescale to be mostly sensitive to the mass of the black hole. However, varying the age and metallicity of the star can allow the mass and radius to influence the peak timescale to a greater degree. Therefore, the largest systematic uncertainty in our measurements of black hole masses likely comes from uncertainty in the mass-radius relation of the disrupted stars.

In our model we determined the radius of the stars as a function of their mass. We used the mass-radius relation for ZAMS solar metallicity stars given in Tout et al. (1996) for main sequence stars, and set the radii of brown dwarfs to be constant (see Section 2.2). To test how varying the metallicity and age of the stars might affect our measurements, we ran test fits with an additional *radius anomaly* parameter to characterize the uncertainty in the mass-radius relation at each stellar mass. We calculated radius values as a function of mass, metallicity and age for main-sequence stars using `MIST` (Dotter 2016; Choi et al. 2016; Paxton et al. 2011, 2013, 2015), and used the maximum and minimum radius values at each stellar mass to bound our *radius anomaly* parameter. This was also done for brown dwarfs using the radius values calculated in Burrows et al. (2011).

We chose a conservative implementation of the *radius anomaly* uncertainty parameter by using a flat prior. Instead of choosing our prior to disfavor unusual

age and metallicity combinations, every possible age and metallicity explored in `MIST` and Burrows et al. (2011) was weighted equally. Using the results from these fits we calculated additional systematic errors for each parameter. These error measurements can be found in Table 2.3. In general they are significantly larger than the statistical errors quoted in Table 2.2; for example, the systematic error in the black hole mass was found to be ~ 0.2 dex whereas statistical errors in black hole mass are typically $\lesssim 0.1$ dex.

To further test how changing the mass of the star changes the resulting fit, we performed fits of PS1-10jh while keeping the parameter for the mass of the star constant. We performed these tests for three different star masses: 0.1, 1, and 10 $M_{\odot}$. We found that all three tests achieved comparably good scores, implying that the mass of the star is a degenerate parameter that is difficult to measure accurately with our current model. However, the mass of the black hole does not change dramatically when fixing the stellar mass to different values–despite the uncertainty in the mass of the star we are still able to measure the mass of the black hole. The variation in the black hole mass between tests implies larger uncertainty than our fits in which we leave the stellar mass as a free parameter, however the variation is within the systematic errors we quote in Table 2.3. Although only slightly favored by the evidence from the light curve fits, lower mass stars are far more common (Kroupa et al. 1993) and thus it is likely that the lower stellar masses are closer to the true value. The results from these tests are shown in Table 2.6 and are described further in Section 2.6.3.

We note that we find a slight preference for stellar masses near $0.1M_{\odot}$ (7 events

prefer stellar masses between 0.09 and 0.2 $M_{\odot}$), which is near the peak in the initial mass function. In addition to low mass stars being more common, this preference is likely contributed to by the fact that below this mass the radius of the star no longer cancels out the effect of the mass of the star on the time of peak of the light curve (see Equation 2.5) – the mass continues to decrease while the radius remains relatively constant as the star transitions into the brown dwarf regime. For simplicity we assumed the radius was constant below $0.1M_{\odot}$ in our current model, although in reality it is likely the radius will actually slightly increase below this mass, see Burrows et al. (2011). This changing mass-radius relationship means that the shortest possible peak times are achieved at $M_{*} \sim 0.1M_{\odot}$, and thus masses near $0.1M_{\odot}$ are favored for events in which short peak times are desired.

2.5 Black Hole Mass Estimation

Without directly imaged stellar orbits (e.g. Sagittarius A*), it is very difficult to directly measure black hole masses, and therefore most estimations in the literature are derived using relations between a galaxy's large-scale properties and the size of the black hole at its center. The $M_{\rm h} - \sigma$ relation and the $M_{\rm h} - L_{\rm bulge}$ relation have proven instrumental to our understanding of black holes as a population, but both relations suffer from significant uncertainties.

The intrinsic scatter in the $M_{\rm h} - \sigma$ varies between $\sim 0.3 - 0.5$ dex (it is ~ 0.46 dex for the lower mass galaxies in Figure 2.5), and the scatter in the $M_{\rm h} - L_{\rm bulge}$ relation is similarly ~ 0.5 dex (McConnell & Ma 2013). The $M_{\rm h} - \sigma$ relation also changes with

galaxy morphology (Hu et al. 2009; Gadotti & Kauffmann 2009; Graham & hui Li 2009; Gültekin et al. 2009). For example, the relation is a factor of two different for early-type versus late-type galaxies, and differs by an additional factor of two depending on the central density profiles of the galaxies (McConnell & Ma 2013).

The dependence of the $M_{\rm h} - \sigma$ and $M_{\rm h} - L_{\rm bulge}$ relation on black hole mass itself has been explored extensively, suggesting that an evolving relationship with mass is likely necessary to minimize scatter. McConnell & Ma (2013) find that the $M_{\rm h} - L_{\rm bulge}$ appears to have a shallower slope for black holes below $\sim 10^8 M_\odot$, and Jiang et al. (2011) find that the relation differs by over an order of magnitude for black holes between $10^5 M_\odot$ and $10^6 M_\odot$. In a study of megamaser galaxies with $M_{\rm h} < 10^8 M_\odot$, Greene et al. (2010) find that the $M_{\rm h} - \sigma$ relation for larger elliptical galaxies does not hold for their sample of lower mass, maser galaxies. Unfortunately, very few black hole masses have multiple mass measurements, and those that do don't necessarily agree within their error estimates (Peterson 2015).

Ultimately, accounting for the aforementioned complications can further minimize the scatter about the best-fitting relationship, but these tuned models still make black hole mass predictions that are no better than a factor of ~ 2 at all black hole mass scales. While the black hole mass measurements presented in this paper are not always within a 68% confidence interval of mass measurements from the $M_{\rm h} - \sigma$ relation and the $M_{\rm h} - L_{\rm bulge}$ relation found in the literature, they fit comfortably within the inherent scatter present in both of these relations. In Figure 2.5 we overplot the black hole mass measurements from this work on the $M_{\rm h} - \sigma$ relation plot found in Xiao et al.

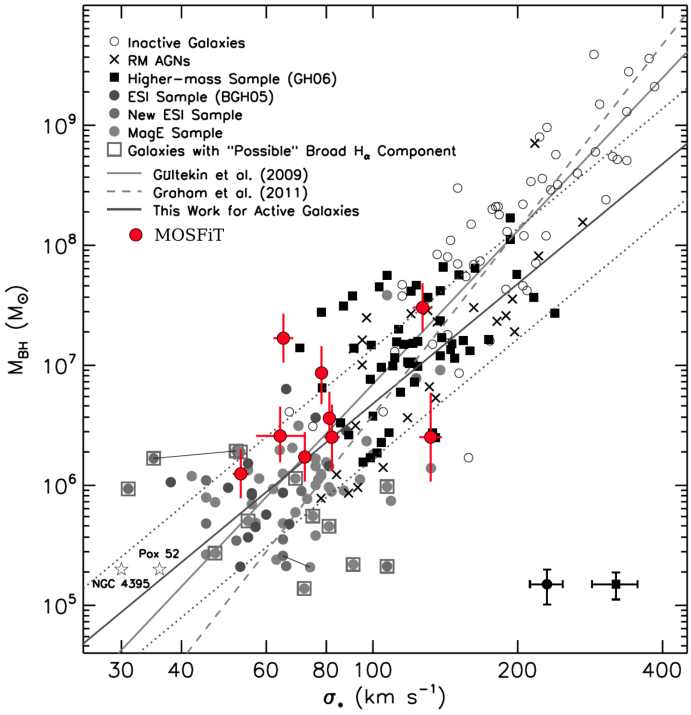

Figure 2.5: $M_{\rm h} - \sigma$ for a variety of black hole mass estimates (adapted from Xiao et al. 2011, see that work for details on the original points plotted). The red points show the mass estimates from this work, where the velocity dispersion measurements for our sample of black holes were accumulated from Thomas et al. (2013); Wevers et al. (2017); Blagorodnova et al. (2017); Gezari et al. (2017).

(2011), one of the few studies that include a significant number of black hole mass measurements below $10^7 M_\odot$. It becomes increasingly difficult to measure black hole mass through direct measurement methods as the mass of the black hole decreases. Most direct measurements of black holes in this mass range, such as the ones in Figure 2.5, come from AGN, as reverberation mapping does not require that the sphere of influence be resolved.

2.6 Discussion

2.6.1 Luminosity Follows Fallback Rate

In Section 2.3.3 we briefly discussed how the luminosity appears to closely follow the fallback rate and that none of the events necessitate a viscous delay. Figure 2.4 shows how varying the viscous timescale changes the light curve of PS1-10jh – it is clear that the data is best fit when $T_{\rm viscous}$ is a very small fraction of $t_{\rm peak}$.

For the luminosity to follow the fallback rate, the debris from the disruption must circularize promptly (or more precisely, while maintaining its initial mass-energy distribution) upon its return to pericenter (Guillochon et al. 2014). General relativistic effects are expected to play an important role for disruptions in which $R_{\rm p}$ is comparable to the gravitational radius $R_{\rm g} \equiv GM_{\rm h}/c^2$. Rapid circularization might be achieved through the effects of general relativity, which can strongly influence the trajectories of infalling material. GR precession effects can, for example, cause the stream of infalling debris to intersect itself (e.g., Dai et al. 2013), enabling a dissipation of kinetic energy, as seen in several recent hydrodynamical simulations (Hayasaki et al. 2013). This will naturally lead to rapid circularization.

If spin is included in the calculation, the stream deflects not only within its own orbital plane, but also out of this plane. The result is that the stream does not initially collide with itself (Stone & Loeb 2012) and circularization does not immediately occur. If dissipation is minimal, the stream is extremely thin (Kochanek 1994; Guillochon et al. 2014) and wraps around the black hole many times (Guillochon & Ramirez-Ruiz 2015b). In the case of inefficient cooling (Bonnerot et al. 2016a), the

stream can thicken over only a few passages around pericenter, and will intersect with itself more quickly. After a critical number of orbits, stream-stream interactions finally begin to liberate small amounts of gas. This eventually leads to a catastrophic runaway in which all streams simultaneously collapse onto the black hole, circularizing rapidly. For these events, the luminosity should still follow the original fallback rate so long as the mass-energy distribution of the debris remains unchanged (similarly to if rapid circularization had occurred), albeit after a fixed delay time post-disruption. Additionally, once circularization occurs the infalling material is likely to collect around the SMBH into a quasi-spherical layer. This layer is expected to quickly engulf the forming accretion disk, potentially leading to significant reprocessing of the emanated radiation.

In Figure 2.6 we see that the majority of the fits prefer highly relativistic encounters, which naturally leads to the luminosity following the fallback rate. As mentioned in the previous section, we also find slightly larger black hole masses than those derived using standard galaxy scalings. Larger black holes have larger $R_{\rm g}$ and can thus more easily cause relativistic disruptions. In Figure 2.6 we show that once $M_{\rm h}$ is a few times $10^7 M_\odot$, $R_{\rm g} \approx R_{\rm t}$ for $M_* \approx 0.1 M_\odot$ (the peak of the IMF), meaning that all disruptions in that parameter space are highly relativistic. In general, most of the fits prefer $R_{\rm p}/R_{\rm g} \lesssim 10$. If $R_{\rm p}/R_{\rm g}$ is calculated using the black hole masses from the $M-\sigma$ relation (the masses that are systematically smaller than what `MOSFiT` measures), $R_{\rm p}/R_{\rm g}$ increases from an average value of ≈ 12 to ≈ 25 for those disruptions (not all events in this selection have $M-\sigma$ measurements for their black holes).

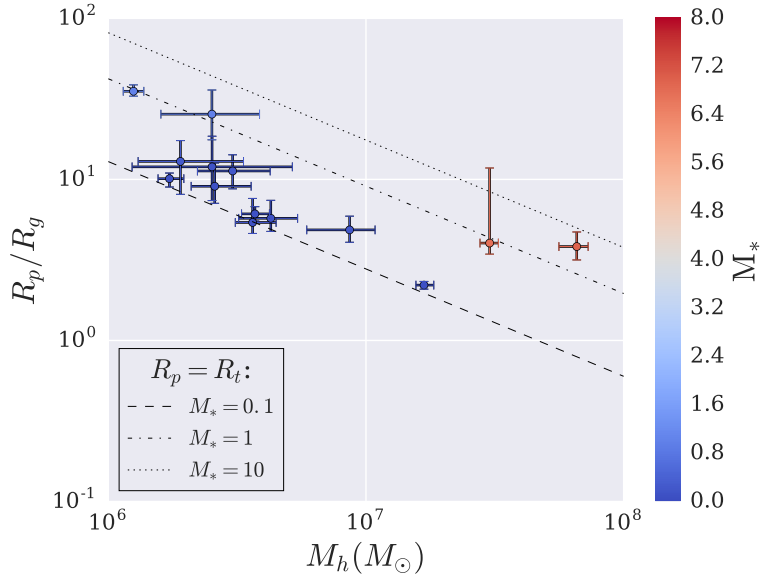

Figure 2.6: The dashed lines show $R_\mathrm{t}/R_\mathrm{g}$ as a function of M_h for differing M_*. Because $R_\mathrm{t}/R_\mathrm{g} \propto M_h^{-2/3}$, we expect that lines with slopes of $-2/3$ will map to stars of different masses. Here we have assumed the Tout et al. (1996) relations for $R_*(M_*)$. There is a dependence on the impact parameter as well, and here we have set $\beta = 1$ for the dashed lines, however most of the fits prefer β near 1 and, as the plot implies, they also prefer stars between 0.1 and 1 $M_\odot$.

It has previously been postulated that we should expect a large number of TDEs to be viscously delayed, around 75% for the black hole mass range probed by the TDEs in this paper (Guillochon & Ramirez-Ruiz 2015b). Our results imply that we are therefore missing a number of viscously delayed TDEs. It is natural to ask why we seem to be biased towards these prompt, relativistic events. The most obvious explanation is simply that events that fall into this category tend to be easier to detect, as viscous delays can drastically flatten the peak of the light curve, as shown in Figure 2.4.

2.6.2 Dynamic Reprocessing Layer

TDEs can result in highly super-Eddington mass fallback rates (De Colle et al. 2012), and therefore we expect excess debris surrounding the black hole to reprocess light from the various dissipation regions (Loeb & Ulmer 1997; Ulmer et al. 1998).

This is particularly true for the events discussed in this work, as most of them are near full disruption ($\beta_{\rm fd} = 1.8$ for 4/3 polytropes and $\beta_{\rm fd} = 0.9$ for 5/3 polytropes), with large fractions of the disrupted star remaining bound to the black hole, as shown in Figure 2.7.

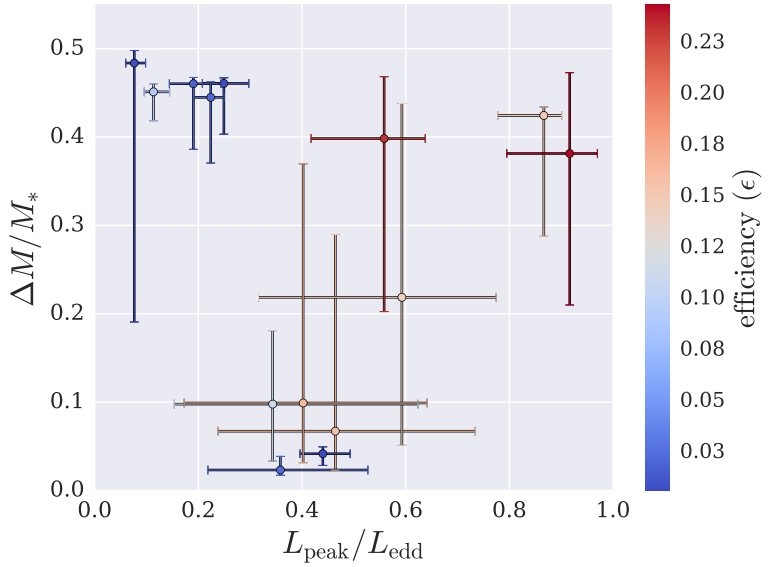

Figure 2.7: Fraction of the total stellar mass that remains bound to the black hole versus the fraction of the Eddington limit the peak luminosity reaches.

As our model caps the luminosity of each flare to be no greater than the Eddington limit, our maximum radiated luminosities do not exceed Eddington for any of the modeled flares. However, the fallback rate can exceed the Eddington mass fallback rate (assuming the Eddington mass fallback rate is defined using a constant efficiency,

TDE	$T_{\rm phot,\,MOSFiT}$ (10^3 K)	$T_{\rm phot,\,lit}$ (10^3 K)	source
PS1-10jh	35^{+4}_{-2}	29^{+2}_{-2}	1, 2
PS1-11af	22^{+1}_{-1}	19^{+1}_{-1}	3
PTF09djl	25^{+4}_{-5}	49^{+5}_{-5}	1, 4
PTF09ge	13^{+1}_{-1}	22^{+2}_{-2}	1, 4
iPTF16fnl	33^{+2}_{-2}	35^{+4}_{-4}	1, 5, 6
iPTF16axa*	17^{+2}_{-2}	30^{+3}_{-3}	1, 7
ASASSN-14li	63^{+7}_{-8}	35^{+3}_{-3}	1, 8, 9
ASASSN-15oi	33^{+3}_{-3}	20^{+2}_{-2}	10
ASASSN-14ae	22^{+1}_{-1}	21^{+2}_{-2}	1, 11
OGLE16aaa	23^{+6}_{-4}	> 22	12
D1-9*	110^{+33}_{-26}	55^{+10}_{-10}	13
D3-13*	217^{+4}_{-6}	10^{+1}_{-1}, 490^{+20}_{-20}	13
TDE1	34^{+7}_{-6}	29^{+2}_{-2}	1, 14
TDE2	28^{+1}_{-3}	18^{+1}_{-1}	14

[1]Wevers et al. (2017), [2]Gezari et al. (2012), [3]Chornock et al. (2014), [4]Arcavi et al. (2014), [5]Blagorodnova et al. (2017), [6]Brown et al. (2018), [7]Hung et al. (2017), [8]Holoien et al. (2016b), [9]van Velzen et al. (2016b), [10]Holoien et al. (2016a), [11]Holoien et al. (2014), [12]Wyrzykowski et al. (2017),[13]Gezari et al. (2008), [13]van Velzen et al. (2011)

*Temperatures for these events are taken from $\gtrsim 100$ days after the peak of the light curve

Table 2.4: Comparison of photosphere temperatures with literature values. The temperatures in this table were taken near the peak of the light curve with the exception of the three starred (*) TDEs: iPTF16axa, D1-9 and D3-13. The literature values for these events were measured $\gtrsim 100$ days after peak, and so the values quoted from `MOSFiT` were taken as close as possible to the times listed in the source papers for those events. We note that D3-13 has two temperature measurements listed that differ by over an order of magnitude – this is because Gezari et al. (2008) used two blackbodies to fit the optical and UV data for that event. Finally, we note that the value from the literature for ASASSN-14li is dominated by systematic uncertainty not included in the quoted error (Holoien et al. 2016b).

$\dot{M}_{\rm Edd} = \frac{L_{\rm Edd}}{\epsilon c^2}$). In our model, as black holes near their Eddington limit, we implement a soft cut on their luminosity, essentially decreasing the efficiency for the part of the fallback rate that would otherwise result in super-Eddington luminosities. This does

not change the average efficiency beyond the quoted errors. However, it does meant that as the luminosity approaches the Eddington luminosity, it becomes more difficult to discern how much mass the black hole is actually accreting as the luminosity depends little on the Eddington excess.

The peak luminosities of most events are $> 10\%$ of their Eddington luminosities, and the peak bolometric luminosity of the fitted events increases with black hole mass, suggesting the luminosities of the events are Eddington limited. Although this runs contrary to the inverse relationship between $L_{\rm peak}$ and $M_{\rm h}$ given by the peak luminosity scaling relation (Equation (2.4)), this is what we expect for Eddington limited events as $L_{\rm edd} \propto M_{\rm h}$.

Figure 2.8 shows the relationship between the radius and temperature of this reprocessing layer and the luminosity of the fits. In our fits where we have assumed that the size of the photosphere follows $\dot{M}$ to some power, the temperature we get from the emitting photosphere is comparable with that which has been derived from both fitting blackbodies to the photometry and from spectral observations, with peak values between $2 \times 10^4 - 10^5 K$ (see Figure 2.4).

Although we required the photosphere size to scale as a power law of $\dot{M}$, the parameter range used allowed the exponent of the power law to be zero, which would signify no correlation between $\dot{M}$ and $R_{\rm photo}$. Instead we found that for all fits the exponent was $> 1/2$ – the fits required that $R_{\rm photo}$ be a strong function of $\dot{M}$. A similar power law relationship was used to fit the photospheric radius of simulations of TDEs in Jiang et al. (2016b), and the power law exponent in that work was found to be ~ 1,

similar to what we find for some of the event fits presented here.

In Section 2.3.3 we discussed how our model for a growing and shrinking photosphere can help explain additional late time components in TDE light curves. This behavior can also help explain the minimal color evolution present in the light curves. Assuming that the size of the photosphere was set by the tidal radius or the last stable orbit (Loeb & Ulmer 1997; Ulmer et al. 1998), one might expect the temperature to fluctuate as the luminosity varied, as $T \propto L^{1/4}$. However, if the radius of the reprocessing layer increases with luminosity, then $T \propto L^{1/4}/R^{1/2} \propto L^{1/4}/L^{l/2} = L^{1/4-l/2}$ where l is a power law exponent relating L and R (see Equation (2.10)). As can be seen in Table 2.2, we find that most fits prefer $l > 1/2$. Instead of the temperature increasing with luminosity, it decreases slightly near peak and then gradually increases as the luminosity decreases (Figure 2.8). Because the photosphere temperature is at a local minimum near peak, it can easily match observations that find approximately constant temperature at those times.

This can be interpreted as the result of reprocessing the radiation by a layer of material with optical depth $\tau \sim 1$ in the accretion structures formed by the tidal disruption. The source of this material can be naturally explained by high-entropy material generated by the circularization process, of which only a fraction needs to be ejected to obscure the accretion disk (Guillochon et al. 2014). Just as prompt circularization allows the luminosity to follow the fallback rate, it might explain why the reprocessing radius follows the luminosity provided that the obscuring material drains into the black hole on timescales that are short enough to prevent a significant build-up of material.

Another possible explanation is that the reprocessing layer is generated by a wind or an outflow (Ulmer et al. 1998; Strubbe & Quataert 2009; Miller 2015; Metzger & Stone 2016). This is described recently in Jiang et al. (2016b), and we find that the temperature evolution seen in Figure 2.8 is reminiscent of the evolution they predict, although the exact power law relations we find between $\dot{M}$ and the photosphere properties show a wider variety of solutions. The Jiang et al. model also predicts temperatures that decrease near peak, because the photospheric radius of the outflow grows with luminosity, and then temperatures that subsequently increase after peak as the ejecta eventually becomes transparent.

2.6.3 Summary and Future Prospects

- Black hole masses can be accurately measured using tidal disruption events. While the relationship between the time of peak of a TDE and the disrupting black hole's mass was first noted in Rees (1988) – $t_{\rm peak} \propto M_{\rm h}^{1/2}$, it remained unclear until this work if the luminous output of a disruption could be used to measure masses accurately. And although the black hole mass can be estimated from $t_{\rm peak}$ alone, fitting multi-band light curves yields an increased precision of the measurement and makes it possible to learn about other key disruption parameters. Our measurements generally match previous values presented in the literature, as shown in Figure 2.3, but we do find some exceptions where the black hole masses acquired from light curve fitting disagree from those derived from galaxy scaling relations.

- All of the events in this sample have luminosity curves that almost directly follow

the fallback of the stellar debris. This requires that the mass-energy distribution remains frozen until it begins to radiate, which can be accomplished through rapid circularization (Hayasaki et al. 2013; Guillochon & Ramirez-Ruiz 2015a). When stream intersections occur close to the black hole, the debris is likely to circularize quickly. Because of this, more relativistic encounters with larger impact parameters and black hole masses can increase the likelihood that stream intersections will happen closer to the circularization radius. A lower radiative efficiency in the debris streams can also increase the likelihood that stream intersections occur close to the circularization radius (Bonnerot et al. 2016a). However, it is unlikely that all TDEs experience rapid circularization (Guillochon & Ramirez-Ruiz 2015a), and there is still likely to be a class of TDEs that are viscously delayed and are thus generally overlooked in UV/optical surveys.

- These events are Eddington limited and in most cases significant fractions ($\Delta M/M_* > 0.1$) of the disrupted stars are bound to the black holes (see Figure 2.7). In these cases there was likely a large amount of stellar debris surrounding the black hole after circularization that could reprocess light from the event.

- A reprocessing layer that evolves with the bolometric luminosity provides a good match to the optical and UV observations. This could be interpreted as high-entropy material that was generated during the circularization process and then quickly drained into the black hole on timescales short enough to avoid significant build-up. It could also be interpreted as an outflow of material that grows at early times and eventually becomes transparent (Jiang et al. 2016b; Metzger & Stone

2016). Both of these scenarios could hide the accretion disk from view at early times, preventing X-rays from escaping until the reprocessing layer recedes and/or becomes transparent.

- Our results suggest that we are (unsurprisingly) biased towards observing the brightest TDEs, which are biased towards the largest black holes when the luminosity is Eddington-limited (but below $\sim 10^8 M_\odot$ as most stars are swallowed whole after that point). We find that events in our sample exhibit rapid circularization with no viscous delays lowering the peak luminosity, have luminosities that peak at a significant fraction of their Eddington limits, and are on the high mass end of potential host black holes for tidal disruptions.

While we are able to reliably obtain black hole masses from our analysis of light curves, we find the star and orbit properties are more difficult to determine uniquely. This is likely because the timescale at peak is insensitive to the star's mass, and also because the amount of mass that falls back onto the black hole is degenerate with the efficiency of the radiative process, which we remained agnostic about in this work. As a result, we are often able to find local solutions of similar quality even for radically different efficiency/star mass combinations. While the light curve fits are similar, we suspect that higher efficiency, lower mass solutions are preferable given their improved odds of occurring: low mass stars are significantly more likely to be disrupted than high mass stars. This degeneracy could be broken by a more complete library of stellar disruptions that accounts for relativistic effects (such as black hole spin, Tejeda et al. 2017) and stellar evolution (which affects composition, rotation, and central concentration) on the

debris. Alternatively, the efficiency could be constrained by measuring the properties of the accretion disk and then using limits from these measurements to inform the priors on `MOSFiT`'s TDE model. This has been recently attempted for some events, including ASASSN-14li (Cao et al. 2018), PTF09djl (Liu et al. 2017), and PS18kh (Holoien et al. 2018b). We find that our measured efficiency for ASASSN-14li is significantly higher than the value calculated by Cao et al. (2018) from their modelling of the disk (they find $\epsilon \sim 4 \times 10^{-3}$). However, as our systematic uncertainties are large, it is possible the measurements are consistent (Cao et al. (2018) does not quote error values). Our measurements for the efficiency of PTF09djl are consistent with Liu et al. (2017). By determining the stellar properties uniquely (or constraining their range by breaking their degeneracy with the radiative efficiency), we could reduce our systematic error in our black hole mass estimates from ~ 0.2 dex, to the statistical error bars of an individual model, ~ 0.1 dex.

Our current model provides a solid basis for understanding events that radiate most of their energy in the optical/UV. In the future we plan to add an accretion disk component to our model, which will enable fits of TDEs that emit in the X-ray. We also plan to transition to a more realistic library of tidal disruption simulations (e.g. Law-Smith et al. in prep) that utilize MESA models of stars to account for their evolution. As explained above, we expect that this will break the current degeneracy between the mass of the star and the efficiency parameter and allow us to further refine our black hole mass estimates.

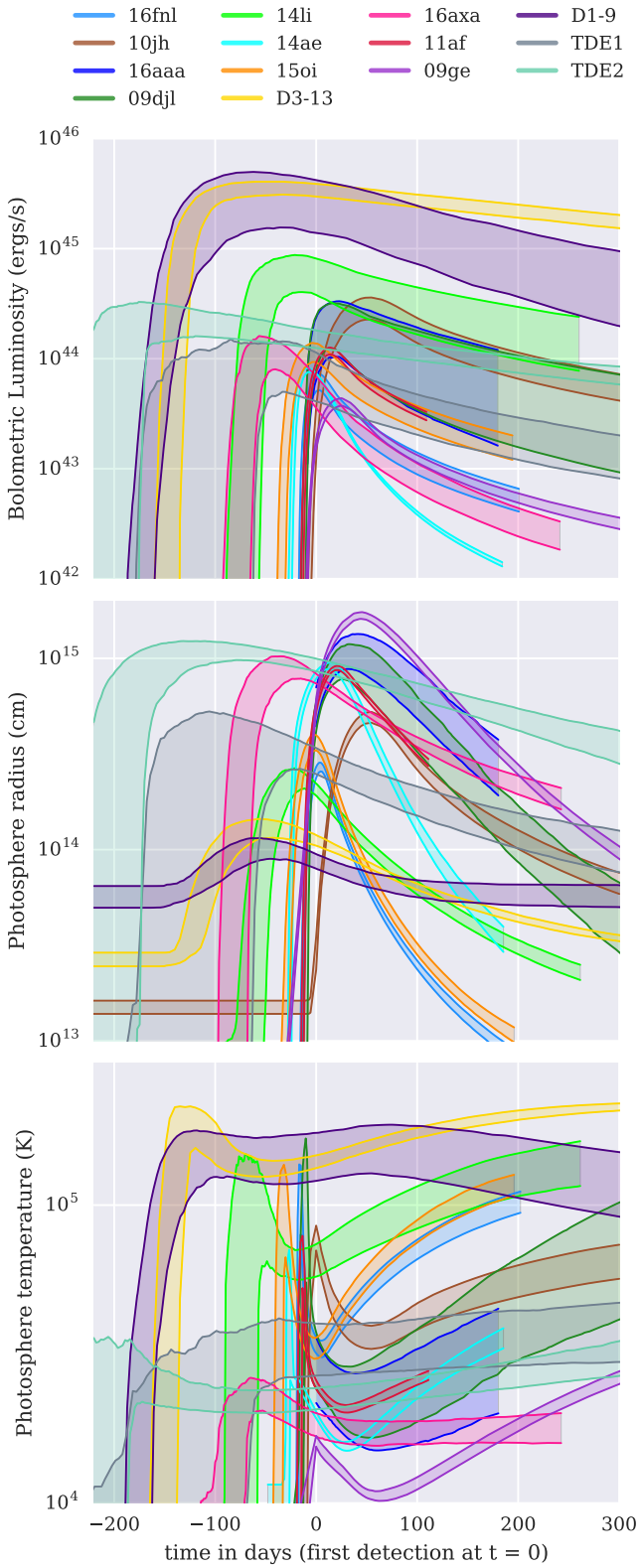

Figure 2.8: Caption on next page.

Figure 2.8: Bolometric luminosity, photosphere radius, and photosphere temperature curves as a function of time since discovery. Each event's curves are colored distinctly and the shaded regions represents the 68% confidence intervals. The photosphere is approximated as a power law of $L_{\rm bol}$ (see Equation 2.10), and the temperature plotted is the blackbody temperature of the photosphere.

2.7 Supplemental Data

TDE	$R_{\rm p}/R_{\rm g}$	$L_{\rm bol}/L_{\rm edd}$	$\Delta M/M_*$
iPTF16fnl	$10.1^{+0.8}_{-1.1}$	$0.25^{+0.05}_{-0.04}$	$0.46^{+0.01}_{-0.06}$
PS1-10jh	$2.2^{+0.1}_{-0.1}$	$0.11^{+0.03}_{-0.02}$	$0.45^{+0.01}_{-0.03}$
OGLE16aaa	11^{+3}_{-3}	$0.5^{+0.3}_{-0.2}$	$0.07^{+0.22}_{-0.04}$
PTF09djl	$9.1^{+3.6}_{-2.0}$	$0.6^{+0.2}_{-0.3}$	$0.2^{+0.2}_{-0.2}$
ASASSN-14li	$4.9^{+1.0}_{-0.8}$	$0.56^{+0.08}_{-0.14}$	$0.40^{+0.07}_{-0.20}$
ASASSN-14ae	35^{+3}_{-2}	$0.44^{+0.05}_{-0.04}$	$0.04^{+0.01}_{-0.01}$
ASASSN-15oi	6^{+2}_{-1}	$0.19^{+0.05}_{-0.05}$	$0.46^{+0.01}_{-0.07}$
D3-13	$4.0^{+7.8}_{-0.6}$	$0.87^{+0.03}_{-0.09}$	$0.42^{+0.01}_{-0.14}$
iPTF16axa	25^{+11}_{-8}	$0.4^{+0.2}_{-0.1}$	$0.02^{+0.02}_{-0.01}$
PS1-11af	$6.1^{+0.7}_{-0.6}$	$0.22^{+0.03}_{-0.03}$	$0.45^{+0.02}_{-0.07}$
PTF09ge	$5.4^{+2.2}_{-0.8}$	$0.08^{+0.02}_{-0.02}$	$0.48^{+0.01}_{-0.29}$
D1-9	$3.8^{+0.9}_{-0.7}$	$0.3^{+0.3}_{-0.2}$	$0.10^{+0.08}_{-0.06}$
TDE1	12^{+7}_{-5}	$0.4^{+0.2}_{-0.2}$	$0.10^{+0.27}_{-0.07}$
TDE2	13^{+5}_{-5}	$0.92^{+0.05}_{-0.12}$	$0.38^{+0.09}_{-0.17}$

Table 2.5: Tabulated values from Figure 2.6 and Figure 2.7.

$M_{\rm h}$ ($10^6 M_\odot$)	β	M_* ($M_\odot$)	γ	ϵ	$\log(\mathrm{R_{ph0}})$	l	$t_{\rm peak}$ (days)	T_{vis} (days)	WAIC	PSRF
$12.6^{+0.9}_{-1.1}$	$1.81^{+0.03}_{-0.01}$	10.0	4/3	$0.0004^{+0.0001}_{-0.0001}$	$0.28^{+0.06}_{-0.06}$	$0.77^{+0.05}_{-0.05}$	74^{+2}_{-2}	$0.3^{+3.5}_{-0.3}$	199.8	1.012
$8.6^{+0.7}_{-0.7}$	$1.81^{+0.03}_{-0.02}$	1.0	4/3	$0.0038^{+0.0006}_{-0.0005}$	$0.25^{+0.06}_{-0.05}$	$0.73^{+0.05}_{-0.03}$	73^{+2}_{-2}	$0.4^{+4.2}_{-0.4}$	193.5	1.033
17^{+2}_{-1}	$0.90^{+0.01}_{-0.01}$	0.1	5/3	$0.09^{+0.02}_{-0.02}$	$0.8^{+0.1}_{-0.1}$	$1.44^{+0.08}_{-0.09}$	111^{+4}_{-2}	$0.05^{+1.40}_{-0.05}$	200.4	1.034

Table 2.6: Comparison between test runs of PS1-10jh with M_* parameter set to different constant values: 0.1, 1.0, 10.0 $M_\odot$. While all runs converged with similar scores, we expect the run with $M_* = 0.1 M_\odot$ to be the most likely true solution as these stars are much more common and are more likely to be disrupted.

Chapter 3

An Energy Inventory of Tidal Disruption Events

3.1 Introduction

The luminosity of supermassive black holes (SMBHs) residing in the nuclei of most, if not all, galaxies is directly related to the rate at which they are supplied with matter. While active galactic nuclei are supplied by steady flows of fuel for thousands of years, tidal disruption events offer the unique possibility of investigating a single SMBH under feeding conditions that vary over timescales of weeks or months (e.g., Dai et al. 2018).

Nonetheless, the recent breakthroughs in observations of tidal disruption events have highlighted our incomplete theoretical understanding of these transients (e.g., Hung et al. 2017). The candidate flares rise and fall in brightness over a period of weeks to

months, with power-law decline rates that agree (at least for the first several months) with numerical predictions of the rates at which stellar debris falls onto the SMBH (e.g., Guillochon & Ramirez-Ruiz 2013). However, we still do not have a good understanding of how infalling material circularizes and accretes onto the SMBHs, or how or where the emission we observe is generated. Because the source of the emission appears to be obscured by an optically thick reprocessing layer throughout most of the observed light curve, our understanding of the inner processes generating the radiation remains incomplete (e.g., Roth et al. 2016).

The compilation of an energy inventory offers an overview of the integrated effects of the energy transfers involved in tidal disruption events. By estimating the efficiency of conversion of mass into electromagnetic radiation, it is possible to constrain whether the emission originates from accretion onto the black hole, or whether it originates at larger radii during the circularization of bound stellar debris.

Observational studies have shown that the energy estimated from the observations of TDEs does not add up to the total energy expected from the accretion of half of a solar mass of material, which corresponds to $\approx 10^{53}(\epsilon/0.1)(M_*/0.5M_\odot)$ ergs assuming a commonly used efficiency value of 0.1 (all but one of the events discussed in this work have energy estimates below 10^{53} ergs). To solve this *missing energy problem*, it has been suggested that if the luminosity is generated instead from circularization processes such as stream collisions, which occur at larger radii from the black hole, the mass-to-energy efficiency would decrease, lowering the total expected energy and reducing the apparent tension between theory and observations (Piran et al. 2015). Other papers

addressing this discrepancy have suggested that a large fraction of the rest mass energy is carried by outflows (Metzger & Stone 2016), or that additional energy is emitted either at higher frequencies that are not covered by existing observations (Lu & Kumar 2018), or at later times by an accretion disk with a very long viscous timescale (van Velzen et al. 2019). To aid this discussion we provide a robust calculation both of the total energy radiated during these flares and the associated conversion timescales.

Most observational studies of optical and UV TDEs include estimates of the bolometric luminosity at peak or at discovery. Some also include estimates of the radiated energy by integrating the bolometric light curve. For the transients discussed in this paper, the literature estimates of bolometric luminosity curves are calculated either by fitting a simple model to the observed light curve (Gezari et al. 2008, 2012; Hung et al. 2017), applying a bolometric correction to the optical/UV light curves (Chornock et al. 2014), or fitting thermal blackbody spectra to the photometric light curves (Holoien et al. 2014, 2016a,b; Hung et al. 2017; Blagorodnova et al. 2017).

While these are important steps towards estimating the total energy emitted by these flares, the data often does not have wide band coverage (many events have limited UV coverage), and generally does not extend for more than a few peak times, leading to large uncertainties in the estimates of the total energy. Here we use a different approach. We require the bolometric luminosity to follow the expected fallback rate of the stellar debris, allowing us to fit the light curve of each event using the Markov-Chain Monte Carlo (mcmc) fitting code `MOSFiT` (Guillochon et al. 2018; Mockler et al. 2019a). This allows for a robust estimate of the total energy radiated to be made not only

while observations were taken, but also at early and late times before the transient was discovered and after the observing campaign ended. The inventory, which is presented in Table 3.1, is arranged by individual events and components within energy and timescale categories, and includes energy estimates from the literature. The explanations for each entry are presented in Section 3.2. A guide on how the conversion efficiency of mass into electromagnetic radiation is estimated is detailed in Section 3.3. Finally, Section 3.4 discusses the implications of the compilation and how it offers a way to assess how well we understand the physical processes at play.

3.2 Calorimetry

To constrain the energy released in optical and UV tidal disruption events, we assume that the bolometric luminosity follows the mass fallback rate and fit an evolving blackbody to the optical and UV light curves. The assumption that the luminosity follows the fallback rate works well for the light curves of many optical and UV TDEs (Mockler et al. 2019a), and is the expected result if circularization is prompt and an accretion disk is formed on timescales less than the fallback timescale or if the emission is produced by circularization processes such as stream collisions (Bonnerot et al. 2016b; Piran et al. 2015; Bonnerot & Lu 2020).

By fitting a dynamic blackbody photosphere to the optical and UV bands we are approximating the emission as efficiently thermalized. This is the simplest approximation we can make for the reprocessing of the fallback luminosity, and because optically large emitting bodies cannot generally outperform a blackbody of the same size when

radiating into free space, this provides us with a robust estimate on the total radiated energy. The estimates of the total bolometric energy calculated using our model can be found in Table 3.1. For this work we have re-run the fits presented in Mockler et al. (2019a) with an expanded efficiency range, allowing the minimum efficiency to go down to 5×10^{-4}, to ensure we are not biasing our results to higher efficiency estimates. This additional freedom does not significantly change our estimates of the integrated energy, however it does change the median values for the efficiency and stellar mass parameters. We discuss this further in Section 3.3.

We compare the total bolometric luminosity calculated with our model (E_{bol}) to $L_{peak} \times t_{peak}$. Transient events are commonly characterized in the $L_{peak} - t_{peak}$ plane (Kasliwal et al. 2012), and $L_{peak} \times t_{peak}$ seems like a natural way to approximate the energy released by a transient. We find that in most cases $L_{peak} \times t_{peak}$ is less than 1/3 of the total emitted energy for TDEs. Therefore, we caution against using $L_{peak} \times t_{peak}$ when estimating the total energy released for TDEs. We note that throughout this paper we define $t_{peak} = t_{peak,\,ff}$ as the Δt between when mass first begins to return to the black hole and when the light curve peaks – the 'time of peak from first fallback'. This is less than t_{peak} as calculated from disruption, but can be more easily tied to observations, as mass needs to return to the vicinity of the black hole before stream collisions or accretion produce luminosity. On the other hand, $t_{peak,\,ff}$ will be larger than the peak timescale calculated using the first observation of the TDE, as our fits extrapolate back before the first observation to the approximate first fallback time using simulated mass fallback rates.

Table 3.1: Integrated bolometric energy, energy release timescales, and estimated efficiencies with 68% confidence intervals for all light curves included in this work.

TDE	$E_{bol,\,lit}$	E_{bol} (obs. times)	E_{bol} (full curve)	$\frac{E_{bol}\ (obs.)}{E_{bol}\ (full)}$	$\frac{L_p \times t_{p,ff}}{E_{bol}\ (full)}$	$t_{p,ff}$	$\frac{t_{50}}{t_{p,ff}}$	$\frac{t_{90}}{t_{p,ff}}$	avg. ϵ	ϵ at L_p	$\frac{L_p}{L_{Edd}}$	ΔM_{min}
	($\log_{10}$ergs)	($\log_{10}$ergs) (0.09 dex)	($\log_{10}$ergs) (0.11 dex)			(days) (15 days)	(0.24 dex)	(0.32 dex)	($\log_{10}$) (0.68 dex)	($\log_{10}$)	(0.17 dex)	($\log_{10}M_\odot$)
10jh	≥ 51.3	$51.4^{+0.1}_{-0.1}$	$51.6^{+0.1}_{-0.1}$	$0.68^{+0.02}_{-0.03}$	$0.32^{+0.01}_{-0.02}$	55^{+1}_{-1}	$3.3^{+0.4}_{-0.2}$	$37.4^{+27.9}_{-7.3}$	$-3.3^{+0.1}_{-0.0}$	$-3.3^{+0.1}_{-0.0}$	$0.15^{+0.02}_{-0.02}$	$-2.7^{+0.1}_{-0.1}$
D1-9	≥ 50.9	$52.3^{+0.2}_{-0.4}$	$53.0^{+0.2}_{-0.4}$	$0.21^{+0.03}_{-0.03}$	$0.36^{+0.08}_{-0.06}$	127^{+17}_{-12}	$2.6^{+0.5}_{-0.3}$	$8.5^{+6.1}_{-1.8}$	$-1.8^{+0.5}_{-0.6}$	$-1.9^{+0.4}_{-0.5}$	$0.33^{+0.22}_{-0.23}$	$-1.3^{+0.2}_{-0.4}$
D3-13	≥ 52.3	$52.3^{+0.1}_{-0.2}$	$52.9^{+0.2}_{-0.2}$	$0.20^{+0.01}_{-0.02}$	$0.43^{+0.04}_{-0.06}$	123^{+6}_{-7}	$2.4^{+0.2}_{-0.1}$	$6.6^{+1.9}_{-0.9}$	$-1.7^{+0.2}_{-0.3}$	$-1.8^{+0.2}_{-0.2}$	$0.31^{+0.16}_{-0.12}$	$-1.3^{+0.2}_{-0.2}$
14ae	≈ 50.2	$50.2^{+0.0}_{-0.0}$	$50.5^{+0.0}_{-0.0}$	$0.51^{+0.03}_{-0.03}$	$0.40^{+0.03}_{-0.03}$	18^{+2}_{-1}	$2.6^{+0.2}_{-0.1}$	$6.0^{+0.4}_{-0.5}$	$-3.3^{+0.2}_{-0.2}$	$-3.4^{+0.2}_{-0.1}$	$0.48^{+0.07}_{-0.09}$	$-3.7^{+0.0}_{-0.0}$
14li[1]	≈ 50.8	$51.1^{+0.2}_{-0.2}$	$51.6^{+0.3}_{-0.3}$	$0.35^{+0.07}_{-0.05}$	$0.24^{+0.07}_{-0.06}$	40^{+9}_{-8}	$4.4^{+2.0}_{-1.3}$	$23.6^{+27.2}_{-11.8}$	$-1.7^{+0.6}_{-0.8}$	$-1.9^{+0.6}_{-0.7}$	$0.46^{+0.12}_{-0.15}$	$-2.7^{+0.3}_{-0.3}$
15oi	≈ 50.8	$50.4^{+0.2}_{-0.2}$	$50.9^{+0.2}_{-0.3}$	$0.37^{+0.09}_{-0.05}$	$0.29^{+0.09}_{-0.06}$	31^{+5}_{-4}	$3.8^{+1.9}_{-1.2}$	$34.4^{+23.2}_{-22.5}$	$-3.0^{+0.8}_{-0.3}$	$-3.0^{+0.8}_{-0.3}$	$0.19^{+0.07}_{-0.06}$	$-3.4^{+0.2}_{-0.3}$
16fnl	$49.3^{+0.1}_{-0.1}$	$50.1^{+0.0}_{-0.0}$	$50.4^{+0.1}_{-0.1}$	$0.51^{+0.03}_{-0.04}$	$0.35^{+0.02}_{-0.04}$	20^{+1}_{-1}	$2.7^{+0.3}_{-0.1}$	$12.9^{+5.0}_{-2.9}$	$-3.3^{+0.1}_{-0.0}$	$-3.4^{+0.1}_{-0.0}$	$0.30^{+0.04}_{-0.04}$	$-3.8^{+0.1}_{-0.1}$
		$(49.5^{+0.0}_{-0.0})^2$	$(49.7^{+0.0}_{-0.0})^2$									
16axa	≈ 50.7	$50.3^{+0.2}_{-0.1}$	$50.4^{+0.2}_{-0.1}$	$0.78^{+0.05}_{-0.06}$	$0.27^{+0.04}_{-0.03}$	29^{+6}_{-4}	$3.9^{+1.1}_{-0.7}$	$31.1^{+18.6}_{-7.0}$	$-2.8^{+0.3}_{-0.4}$	$-2.8^{+0.3}_{-0.4}$	$0.10^{+0.05}_{-0.03}$	$-3.9^{+0.2}_{-0.1}$
11af	$50.6^{+0.0}_{-0.0}$	$50.7^{+0.0}_{-0.0}$	$50.9^{+0.1}_{-0.1}$	$0.62^{+0.05}_{-0.15}$	$0.35^{+0.04}_{-0.12}$	29^{+2}_{-2}	$2.8^{+2.3}_{-0.3}$	$14.1^{+25.7}_{-4.5}$	$-2.9^{+1.0}_{-0.4}$	$-3.0^{+1.0}_{-0.4}$	$0.26^{+0.05}_{-0.05}$	$-3.4^{+0.1}_{-0.1}$
PTF09ge	$52.0^{+0.1}_{-0.6}$	$50.5^{+0.0}_{-0.0}$	$50.6^{+0.0}_{-0.0}$	$0.64^{+0.02}_{-0.02}$	$0.27^{+0.02}_{-0.01}$	36^{+1}_{-1}	$3.9^{+0.3}_{-0.4}$	$30.8^{+2.3}_{-3.2}$	$-2.6^{+0.2}_{-0.3}$	$-2.6^{+0.2}_{-0.3}$	$0.09^{+0.02}_{-0.01}$	$-3.6^{+0.0}_{-0.0}$
09djl	–	$51.0^{+0.3}_{-0.2}$	$51.2^{+0.4}_{-0.3}$	$0.58^{+0.13}_{-0.12}$	$0.21^{+0.07}_{-0.06}$	26^{+4}_{-3}	$5.1^{+2.3}_{-1.2}$	$23.5^{+38.3}_{-11.2}$	$-1.6^{+0.4}_{-0.4}$	$-1.7^{+0.4}_{-0.4}$	$0.43^{+0.21}_{-0.18}$	$-3.1^{+0.4}_{-0.3}$
TDE2	–	$51.5^{+0.1}_{-0.1}$	$52.1^{+0.1}_{-0.1}$	$0.25^{+0.03}_{-0.03}$	$0.09^{+0.08}_{-0.05}$	40^{+36}_{-13}	$11.0^{+12.1}_{-5.2}$	$93.1^{+107.6}_{-43.1}$	$-1.1^{+0.4}_{-0.5}$	$-1.7^{+0.7}_{-0.5}$	$0.86^{+0.09}_{-0.33}$	$-2.1^{+0.1}_{-0.1}$
TDE1	–	$51.0^{+0.2}_{-0.2}$	$51.3^{+0.3}_{-0.2}$	$0.45^{+0.10}_{-0.11}$	$0.24^{+0.05}_{-0.04}$	52^{+23}_{-17}	$4.6^{+1.4}_{-1.2}$	$38.5^{+22.2}_{-15.1}$	$-1.9^{+0.7}_{-0.5}$	$-1.9^{+0.6}_{-0.5}$	$0.19^{+0.22}_{-0.11}$	$-2.9^{+0.3}_{-0.2}$
16aaa	≈ 52.7	$51.2^{+0.6}_{-0.4}$	$51.3^{+0.6}_{-0.4}$	$0.88^{+0.06}_{-0.09}$	$0.23^{+0.09}_{-0.09}$	33^{+10}_{-5}	$4.6^{+2.9}_{-1.7}$	$21.4^{+40.5}_{-11.0}$	$-1.6^{+0.7}_{-0.6}$	$-1.7^{+0.5}_{-0.6}$	$0.37^{+0.30}_{-0.26}$	$-3.0^{+0.6}_{-0.4}$

Table 3.1: **Notes for Table 3.1:** The transients in the table are organized as follows: The first 9 events have UV detections during the same time period as the optical detections. The events in bold have observations at or before the light curve peak. Systematic errors for parameters are listed at the top of their respective columns, throughout the text we include the systematic errors in the errors quoted for the parameters. Systematic errors for $t_{\rm peak}$ and efficiency (ϵ) are taken from Mockler et al. (2019a), additional errors were calculated using the method described in the same paper and are based on the uncertainty in the stellar mass-radius relation. **Column descriptions:** (1) transient names; (2) Bolometric energy estimates from the literature. The methods used to calculate these estimates are described below in this caption; (3) Bolometric energy estimates from the `MOSFiT` fits, integrated over the same time period used for the literature energy estimates in column 2. The literature energy estimate for PTF09ge is from late-time dust emission and therefore the `MOSFiT` energy estimate for column 3 for this event was integrated over the time period of the initial optical observations presented in Arcavi et al. (2014); (4) Column 2 divided by column 3; (5) The peak bolometric luminosity multiplied by the timescale from first fallback to peak luminosity, divided by column 3; (6) The Δt between when the first stellar debris falls back to pericenter ('first fallback') and the time of peak luminosity. This is necessarily less than the time from disruption to peak; (7) & (8) t_{50} and t_{90} are the respective times when 50% and 90% of the total energy is radiated. The first 5% and last 5% are excluded from the integral. In columns 7 & 8 they are scaled by the peak timescale calculated from first fallback; (9) The average observed efficiency, defined as $E_{\rm bol}/\Delta Mc^2$, where ΔM is the total amount of mass that is bound to the black hole; (10) The peak observed efficiency, defined as $L_{\rm peak}/\dot{M}_{\rm peak}c^2$; (11) Eddington ratio at peak luminosity; (12) The minimum amount of mass required to generate the integrated energy if the conversion from mass to energy were 100% efficient ($E_{\rm bol} = \Delta M_{\rm min}c^2$). **Notes on literature energy estimates:** The value for PS1-10jh was calculated by integrating the light-curve model using a lower limit for the temperature and luminosity (Gezari et al. 2012). The values for both D1-9 and D3-13 were calculated by integrating a $t^{-5/3}$ power law starting at $t_{\rm discovery}$ (after $t_{\rm peak}$) using the lower limits to the blackbody temperature and luminosity (Gezari et al. 2008). The value for PTF09ge was calculated from IR dust emission, motivating that there is additional radiated energy not observed in the initial optical and UV light curve (van Velzen et al. 2016a). The values for ASASSN-14ae, ASASSN-14li, ASASSN-15oi, iPTF16fnl, iPTF16axa, and OGLE16aaa were calculated by integrating the blackbody fits to the observed optical and UV light curves (Holoien et al. 2014, 2016b,a; Blagorodnova et al. 2017; Hung et al. 2017; Wyrzykowski et al. 2017). According to Holoien et al. (2016b), the blackbody fit for ASASSN-14li was 'dominated by systematic errors'. For PS1-11af, Chornock et al. (2014) calculated the radiated energy by using a constant bolometric correction to the light curve from a blackbody fit 10 rest-frame days after peak.

Table 3.1: **Discovery papers for TDEs in table:** PS1-10jh, D3-13 & D1-9: Gezari et al. (2012, 2008); ASASSN-14ae, ASASSN-14li, ASASSN-15oi: Holoien et al. (2014, 2016a,b); iPTF16fnl: Blagorodnova et al. (2017); iPTF16axa: Hung et al. (2017); PS1-11af: Chornock et al. (2014); PTF09ge & PTF09djl: Arcavi et al. (2014); TDE1 & TDE2: van Velzen et al. (2011); OGLE16aaa: Wyrzykowski et al. (2017).

[1]This event had significant additional X-ray emission contemporaneous with the optical and UV emission, however we only include an analysis of the energy emitted in optical and UV wavelengths in this work. The energy and efficiency estimates for this event are lower limits.

[2]Values in parentheses were calculated from fits without accounting for host extinction. iPTF16fnl preferred fits with high host extinction, and the literature calculations did not include host extinction (see Section 3.2 for more information).

In Table 3.1, we also compare our total bolometric energy estimates with those derived directly from fitting the observational data. First, we integrate our bolometric luminosity curve to only include the time ranges used in the literature calculations. We find that most of our calculations are similar to previous estimates (see columns 2 and 3 of Table 3.1 for the energy estimates, and the caption for a list of literature sources). We discuss the measurements that are inconsistent with the literature below.

For the transient iPTF16fnl, we calculate a significantly higher total energy when integrating over the same time period as the observations (we find $\log_{10}\mathrm{E_{bol}} = 50.1^{+0.1}_{-0.1}$, Blagorodnova et al. 2017 find $\log_{10}\mathrm{E_{bol}} = 49.3^{+0.1}_{-0.1}$). Our original fit preferred a relatively high value for the host extinction, $\mathrm{E_{B-V,\,host}} = 0.14^{+0.20}_{-0.09}$. We include host extinction as a parameter in the mcmc fit of the light curve, and use the O'Donnell (1994) extinction law for extinction at optical and UV wavelengths (Morrison & McCammon (1983) is used below the Lyman limit, but it is not applicable here). The literature calculation for iPTF16fnl does fit for host extinction, but unlike this work found the best fit to prefer no host extinction (using both Fitzpatrick (1999) and **?**. We fit iPTF16fnl a second time without correcting for any host extinction, and found a lower

value for the energy radiated during observations ($\log_{10}E_{bol} = 49.5^{+0.1}_{-0.1}$), consistent with Blagorodnova et al. (2017). However, this fit has a likelihood score that is about 10 points lower than the fit with host extinction (160 vs 173), therefore we use the fit that includes a host extinction correction in this work. We do include the energy estimates from the fit without a host extinction correction in Table 3.1, below the values for the fit that includes host extinction.

We expect most of the literature estimates of the total energy emitted by transients in our catalog to be less than the values we derive for the total energy (column 4 of Table 3.1). This is because we integrate out to much later times than is possible with existing observations, and we always include the peak of the transient even when the event was caught in the decay phase. There are, however, two events that have literature estimates of the total energy that are significantly higher than those presented in Table 3.1 (column 4). PTF09ge and OGLE16aaa both have literature estimates of the total bolometric energy that are higher than what we derive. In the case of PTF09ge, the literature value is calculated using IR emission measurements taken after the initial optical/UV light curve (van Velzen et al. 2016b). The fact that this method finds a higher value for the energy might imply that there is additional emission that was not captured by the initial optical and UV observations but was effectively reprocessed by dust. For OGLE16aaa, it is unclear why our calculation of the energy is lower than the one presented in the literature. According to Wyrzykowski et al. (2017), the literature estimate is derived using blackbody fits to the optical and UV light curve. While our original fit was only to the optical light curve, we re-fitted the event to also include the

sparse UV data and obtained a similar value for the total emitted energy, with a slightly reduced statistical error ($\log_{10}\mathrm{E_{bol}} = 51.4^{+0.3}_{-0.2}$ erg).

One of the liveliest debated issues in the TDE field concerns the nature of the luminosity decay after peak. This is in part because the fallback rates do not converge to the canonical $t^{-5/3}$ power law until well after peak, if they converge to it at all (e.g. Guillochon & Ramirez-Ruiz 2013). The $t^{-5/3}$ power law decay rate is derived by assuming that the derivative of the mass-energy distribution (dM/dE) is constant and the orbit can be approximated as parabolic[2]. This is a reasonable approximation for the material near the core of the star (the material least bound to the black hole) in a full disruption. However, as numerous papers have highlighted, this is never a good approximation at early times, and for many disruptions it is also not a good approximation at late times (e.g., Gafton & Rosswog 2019). Other power law decay rates have been predicted for the late-time emission from partial disruptions ($t^{-9/4}$, see Coughlin & Nixon 2019), and for disk emission ($t^{-5/12}$, see Lodato & Rossi 2011; Auchettl et al. 2017). These power laws do a better job of approximating the emission decay rates for the relevant flares at the relevant epochs, however, like the $t^{-5/3}$ power law, they have limited applicability. For this reason, we caution against approximating the entire decay rate of the emission as a single power law when calculating the total radiated energy. At the very least, the late-time asymptotic behavior must be treated separately from the early time emission near the peak of the light curve (van Velzen et al. 2019).

[2]The assumption of a parabolic orbit is reasonable for most tidal disruptions occurring in galactic nuclei, see Dai et al. (2013) for a thorough analysis of less eccentric disruptions.

From the evolution of the cumulative energy, we also derived t_{90} (t_{50}) values for all events, which we define here as the time frame during which 90% (50%) of the bolometric energy is accumulated, not including the first and last 5%. We clarify that we do not define t_{50} as the time frame when the middle 50% of the energy is emitted, as it is often defined for gamma-ray bursts, rather we define it as the time when the first 50% of the energy has been radiated (excluding the first and last 5%). Calculating these estimates required using the `MOSFiT` model to extrapolate the bolometric luminosity out past the observations. In Table 3.1 we list the values for $t_{50}/t_{\rm peak}$ and $t_{90}/t_{\rm peak}$ for each fitted event in Table 3.1. We find that t_{50} can occur anywhere from a month to more than a year after peak, while reaching t_{90} takes significantly more than a year and up to ≈ 10 years in some cases. This means that while observations of TDEs often extend out to t_{50}, they rarely extend out to t_{90}, contributing to the underestimation of the total energy radiated that we discussed above.

The compilation of the radiated energy inventory shown in Table 3.1 provides a robust lower limit on the integrated effects of the energy transfer involved in TDEs. The total observed isotropic energy (column 3 in Table 3.1) that is radiated at optical and UV wavelengths is usually larger than that emitted in X-rays during the main flare. This is predominantly due to the fact that νF_ν typically peaks closer to the UV than to the X-rays (at least near the peak of the light curve). However, we note that this is not always the case and it still possible that previous X-ray observations could have missed the time when the X-ray luminosity was highest, resulting in a underestimate for some of the events (Auchettl et al. 2017). It is possible that we are missing X-ray emission due

to inclination effects if our observational line of sight is edge on through the accretion disk, as opposed to closer to the poles (where jet emission would be beamed, Dai et al. 2018). There are also recent reports of an excess of late-time emission for some TDEs (van Velzen et al. 2019) and we discuss the contribution of this emission to the total energy inventory in Section 3.4.1.

3.3 Efficiency

Estimating the radiative efficiency is appropriate for our purpose of uncovering the energy transfer mechanisms in tidal disruption flares. The total efficiency (ϵ), as defined by $E_{\rm bol} = \epsilon M_{\rm bound} c^2$, parameterizes the conversion from rest mass to electromagnetic energy and provides a robust limit on the radiative efficiency. Here $M_{\rm bound}$ is the total mass bound to the black hole after the disruption, which is $\approx M_*/2$ for a full disruption.

As discussed in Section 3.2, we are able to provide a robust estimate of the total energy radiated during these events. However, more complicated modelling is required to estimate the efficiency of conversion from rest mass to electromagnetic energy. To calculate the radiative efficiency we first need a model that accurately estimates the mass supply into the vicinity of the black hole. As described in the previous section, we use the results from hydrodynamic simulations in order to provide an estimate of the rate of mass return to pericenter. The bolometric luminosity can then be simply written as $L_{\rm bol} = \epsilon \dot{M} c^2$. However, the magnitude of the mass fallback rate ($\dot{M}$) is also dependent on the mass ($M_{\rm h}$) and spin (a) of the black hole, the mass of the star ($M_\star$), and the

impact parameter of the disruption (β). Luckily, the mass of the black hole significantly changes the peak timescale (Mockler et al. 2019a) while the impact parameter noticeably alters the shape of the fallback curve (Guillochon & Ramirez-Ruiz 2013; Gafton & Rosswog 2019). As a result, the effects caused by changing these two parameters can generally be disentangled from the effects caused by altering the efficiency when fitting the light curves. It is, however, more difficult to break the degeneracy between the mass of the star and the efficiency, which leads to large systematic uncertainties in the determination of these parameters (Mockler et al. 2019a).

As we mentioned briefly in Section 3.2, we have re-run the fits presented in (Mockler et al. 2019a) with the efficiency prior range expanded by an order of magnitude, from $5 \times 10^{-3} - 4 \times 10^{-1}$ to $5 \times 10^{-4} - 4 \times 10^{-1}$. As the fits are to the same observational data as in (Mockler et al. 2019a), the light curves we obtain are very similar. With this added flexibility, many of the events prefer lower efficiencies and higher stellar masses than those presented in Mockler et al. (2019a).

However, we caution that the degeneracy between the efficiency and the stellar mass makes it difficult to pinpoint a particular stellar mass, and therefore it is not clear that these lower efficiency, higher stellar mass fits are more accurate than the previous fits run with a smaller efficiency prior range. For example, we note that in these new fits, two of the events with the lowest radiative efficiencies prefer very high stellar masses that are strongly disfavored by IMF functions (PS1-10jh prefers $M_* = 8.2^{+29.7}_{-6.4} M_\odot$ and ASASSN-14ae prefers $M_* = 5.4^{+22.0}_{-4.3} M_\odot$). Although there is significant uncertainty in the determination of the mass of the disrupted star and the associated radiative ef-

ficiency, we note that the degeneracy between them does not noticeably change the determination of the bolometric energy measured, as clearly shown in Figure 3.1. Additionally, the black hole masses remain consistent with previous estimates, as do the scaled impact parameters for all fits except iPTF16axa, which now prefers a full disruption rather than a partial disruption. iPTF16axa does not have measurements near peak or strong upper limits, and therefore the rise and the peak of the light curve are not well constrained, which is likely why both a full disruption and partial disruption can fit the light curve.

3.3.1 The mass distribution of tidally disrupted stars

We probe the degeneracy between stellar mass and radiative efficiency by taking the best fit walker distributions derived in Mockler et al. (2019a), and varying the efficiency and stellar mass parameters over the following ranges: $0.0001 < 1$; $0.01 M_{\odot} < M_{\star} < 100 M_{\odot}$. This makes it possible to visualize a large region of likelihood space for these parameters, and the resulting likelihood distributions for a subset of the transients are shown in Figure 3.1. For the plot we chose transients that covered a wide range in parameter space, and have limited the number plotted because adding additional events would overlap. For a given total radiated energy, we find that there is a clear degeneracy between stellar mass and efficiency. However, the spread in total radiated energy is, as expected, small.

Most common theories of tidal disruption rates foresee the disrupted stars coming from within the radius of influence of the SMBH (e.g., Frank & Rees 1976). Each star within this region is expected to trace out a complicated orbit under the

combined influence of all other stars and the SMBH itself. In these crowded regions, two-body interactions alter the distribution of stars on long timescales and, as a result, we expect the disrupted stars to come from near the peak of the IMF (see top panel in Figure 3.1). If this is the case, we expect the radiative efficiencies to be $\gtrsim 10^{-2}$.

Recently, there have been several theories put forward to explain the surprising finding that tidal disruption events preferentially occur in an unusual sub-type of galaxies known as E+A galaxies (Arcavi et al. 2014; French et al. 2016; Law-Smith et al. 2017b; **?**). These theories include an overdensity of stars near the SMBH (Stone et al. 2018; Law-Smith et al. 2017b; **?**), the presence of a SMBH companion (Arcavi et al. 2014; Li et al. 2015), and star formation in eccentric disks around SMBHs (Madigan et al. 2018). Common to all of these theories is the idea that stars deep in the potential well of the SMBH interact with one another coherently, resulting in rapid angular momentum evolution (Rauch & Tremaine 1996). Within this formalism, higher mass stars could, in principle, be preferentially disrupted (compared to the IMF), and as such, systematically lower radiative efficiencies might be possible (Figure 3.1).

3.3.2 The efficiency of super-Eddington accretion

Radiative efficiency can be temporarily reduced near the peak of the flare if the mass accretion rate exceeds the Eddington limit of the SMBH. In this case much of the returning debris must either escape in a radiatively driven wind or be accreted inefficiently (Ramirez-Ruiz & Rosswog 2009; Strubbe & Quataert 2009). In the second case, a sizable fraction of the mass would be fed to the black hole far more rapidly than it could be accepted if the radiative efficiency were high. This can add to the difficulty

of measuring the efficiency of conversion from the rest mass energy to luminosity. For example, in Dai et al. (2018), the authors ran a state of the art simulation of a super-Eddington accretion disk around a massive black hole with a spin of 0.8 and a mass fallback rate of $\approx 15\dot{M}_{\rm Edd}$ and found a reduced mass to luminosity efficiency of 2.7%. According to the same model, events with significant optical emission required the observer to be viewing the event along the direction of the disk to allow for sufficient reprocessing of emission. As such, their mass to observed luminosity efficiency was even lower than 2.7% (the majority of emission was beamed along the polar direction). This is much lower than the expected Novikov-Thorne efficiency of 12.2% for a black hole with a spin of 0.8 (Novikov & Thorne 1973).

The `MOSFiT` TDE model approximates the effect of the super-Eddington regime on the observed luminosity with a soft cut on the luminosity as it approaches $L_{\rm Edd}$, reducing the efficiency of conversion between $\dot{M}$ and $L_{\rm bol}$ near $L_{\rm Edd}$ (Mockler et al. 2019a). The average efficiency and the efficiency at peak derived from our model are listed in Table 3.1, column 9. As expected, the peak efficiency is generally lower than the average efficiency, most noticeably for flares with peak luminosities near the Eddington limit. We note that using the peak efficiency to estimate either the total radiative efficiency or the total energy radiated during these events will lead to an underestimation in these quantities.

The maximum possible peak efficiency of a tidal disruption event is dependent on the Eddington limit of the SMBH, however it is also dependent on the mass of the disrupted star and the impact parameter of the disruption. In Figure 3.2, the dashed

lines show L_{peak}/L_{edd} for full disruptions of different stellar masses, assuming a peak efficiency of 10%.

For example, black holes below $\approx 10^7 M_\odot$ will be super-Eddington at 10% peak efficiency for (full) disruptions of stars above $\approx 0.3 M_\odot$. This implies that most of the black holes in our sample can only reach peak efficiencies of 10% if they disrupt low mass stars, or they break the Eddington limit. On the other hand, as the mass of the black hole increases past $10^7 M_\odot$, the Schwarzschild radius begins to encroach on the tidal radius for main-sequence stars. Once the Schwarzschild radius grows larger than the tidal radius, most disruptions will occur within the black hole's event horizon, and there will be no observable flares.[3]

In Figure 3.2 these disallowed regions of parameter space are shaded in gray, providing additional constraints on the stellar masses for the tidal disruption flares around the largest black holes in this sample. The most massive black hole in this sample, the black hole in the host galaxy of D1-9 (J022517.0-043258), can only disrupt stars $\gtrsim 0.6 M_\odot$. The total energy released in the flare around this black hole is also quite large, and requires the conversion of $0.5 M_\odot$ of mass to energy if the efficiency is $\sim$ 10%, and a correspondingly larger amount of mass for lower efficiencies (from Table 3.1, 10^{53}ergs $\approx 0.1 \times 0.5 M_\odot \times c^2$). Therefore, both the mass of the host black hole and the luminosity of the flare suggest that the disrupted star for the TDE D1-9 was above the peak of the IMF, and likely $\gtrsim 1 M_\odot$.

[3]The exact value of the maximum black hole mass able to produce an observable flare depends on the spin of the black hole and the stellar structure of the star. It also depends on whether or not partial disruptions are included in the calculation, as stars can be partially disrupted at larger radii than are required for full disruptions. This calculation must be done using general relativity, as the tidal forces at a given radius are noticeably different in GR for high mass black holes (Servin & Kesden 2017)

While there is scatter in the Eddington fraction for this sample of TDEs, with values varying between $\sim$ (0.1 − 0.9) L_{peak}/L_{edd}, the median of the distribution is $0.3^{+0.3}_{-0.2}$ L_{peak}/L_{edd} (the median value calculated from the fits in Mockler et al. (2019a) was $0.3^{+0.4}_{-0.2}$). This is similar to the median Eddington fraction derived for AGN (Kollmeier et al. 2006). However, if observed TDE rates are driven by the brightest events, we might expect most of the flares to be pushing up against their black holes' respective Eddington limits (Kochanek 2016).

Very high Eddington ratios would likely produce flattened light curves that would no longer appear to follow the shape of the mass fallback rates near the peak of the light curve (or wherever the mass fallback rate is super-Eddington), due to the significant mass wasted during super-Eddington accretion. Most of the events in this sample (and all of those with well-sampled observations at peak) appear to follow the shape of the expected mass fallback rates and do not push up against the Eddington limit. We note that the fit for TDE2 does prefer a particularly high Eddington fraction (≈ 0.9) and its light curve is flatter than the rest of the sample, as shown in Figure 1 of Mockler et al. (2019a). Unfortunately, as there are no observations at peak for TDE2, that section of the light curve is extrapolated and has large uncertainties, making it is difficult to determine the accuracy of the flattened portion of the light curve.

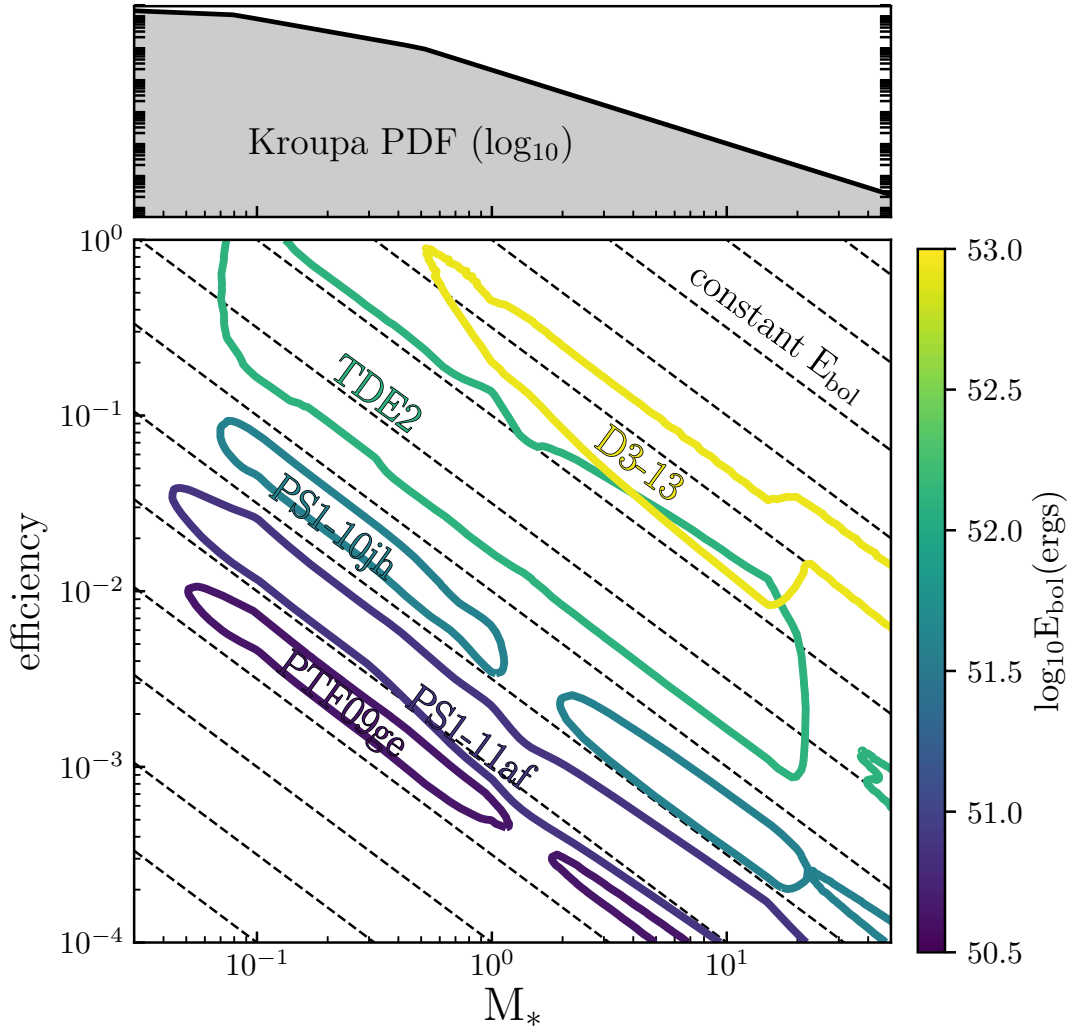

Figure 3.1: The role of stellar mass in TDEs. *Bottom Panel*: The likelihood contours for stellar mass and efficiency parameters derived for five TDEs with a spread of bolometric energy values. The contours have been calculated by taking the parameter values from the converged walker distributions from the `MOSFiT` fits, varying the efficiency parameter between $0.0001 - 1$ and the stellar mass between $0.01 - 100$, and recalculating the likelihood of each parameter combination. We kept the values from the converged walker distributions constant for all parameters except for M_* and efficiency. The contours were arbitrarily chosen as $\log_{10}\text{likelihood}_{\text{max}} - 30$ as this contour value clearly shows the stellar mass - efficiency degeneracy for all plotted fits. Also shown are dashed lines denoting constant bolometric energy. The lines show constant E_{bol} for a given M_{accreted}/M_*. Impact parameter (and therefore M_{accreted}/M_*) vary from TDE to TDE, therefore the value of these lines can vary from event to event. However, the general trend of increasing E_{bol} as one moves up and to the right in the plot is clearly shown in the data. *Top Panel*: The Kroupa IMF is plotted for comparison (Kroupa 2001).

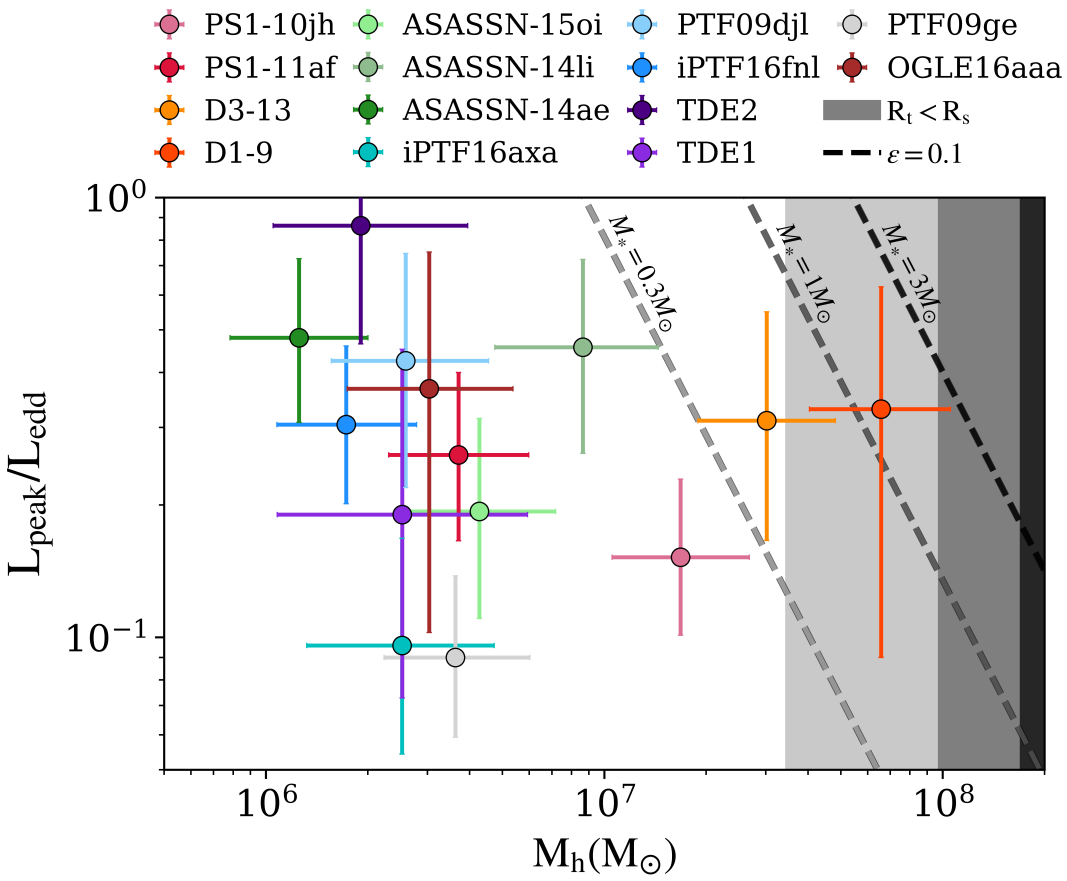

Figure 3.2: Using dashed lines, we plot the Eddington ratio for simulated flares using several stellar masses and assuming an efficiency of 0.1 at peak (a typical AGN efficiency that would produce super-Eddington flares for most TDEs). The shaded regions show were $R_t < R_s$ – the approximate point where stars will be disrupted inside the black hole's event horizon (the lightest shading corresponds to $0.3M_\odot$, the medium shading to $1M_\odot$, and the darkest shading to $3M_\odot$). Eddington limited accretion has a maximum efficiency determined by the accretion radius, mass accretion rate, and Eddington limit, and the median value of the Eddington ratio for this sample is $L_{peak}/L_{edd} = 0.3^{+0.3}_{-0.2}$.

3.4 Discussion

3.4.1 Late-time energy release

As we have shown in Mockler et al. (2019a), the luminosity evolution of tidal disruption events broadly follows the fallback rate of debris. As shown in column 8 of Table 3.1, t_{50} of the radiated energy occurs long after $t_{\rm peak}$ for the majority of the fitted events (t_{50} occurs later than 100 days after peak for 7 of the 14 events, and $t_{50} > 3 \times t_{\rm peak}$ for 9 of the 14 events). As a result, a significant fraction of the total energy is available to be emitted at late times. To check our estimates of the total bolometric energy released in these events, we need observations out to at least t_{50}.

A recent search by van Velzen et al. (2019) for late-time emission from TDEs at times $\gtrsim 10 \times t_{\rm peak}$ found that 10 transients were still emitting at FUV wavelengths (the optical emission had faded below host levels). The same study found that power law fits to early-time FUV emission under-predicted the late-time FUV emission for PTF09ge, PTF09djl, ASASSN-14ae, iPTF16fnl, PS1-10jh, and ASASSN-14li, implying that at these frequencies and at times $\gtrsim 10 \times t_{\rm peak}$, the emission was decaying at a slower rate than predicted by the extrapolations of power law fits to observations near peak.

To compare the observed late-time emission to predictions from the `MOSFiT` model, we let $L_{\rm bol} = \epsilon \dot{M} c^2$, and used the photosphere evolution determined from our fits to the early light curve (with a minimum photosphere radius = $R_{\rm circ}$) to get estimates of the FUV emission at late times ($\gtrsim 10 \times t_{\rm peak}$). This assumption that the photosphere evolution can be extrapolated from early times is likely inaccurate at very late times

($\gtrsim 10 \times t_{\rm peak}$), however we use it to compare with the predictions made by extrapolating the power law fit to the early light curves. We find that our estimates of the late time νL_ν values sometimes under-predict and other times over-predict the observed values, as shown in Figure 3.3. The early time photosphere evolution no longer provides a good description for the late-time emission, and we find that like van Velzen et al. (2019), we also under-predict the FUV luminosity for PTF09ge, PTF09djl, iPTF16fnl, ASASSN-14ae, ASASSN-14li, and PS1-10jh. In general, the discrepancies between our predictions and observations are smaller than those calculated in van Velzen et al. (2019), and our predictions are within an order of magnitude of the observed values for all events except PTF09djl.

In the bottom panel of Figure 3.3 we also compare the predicted $L_{\rm bol}$ from our model to the value derived by van Velzen et al. (2019) by fitting blackbody fits to the late-time observations. The values from our model come from assuming that the efficiency of conversion from mass to energy remains constant at late times, and $L_{\rm bol}$ continues to follow the mass fallback rate. The predicted values for $L_{\rm bol}$ are consistent with the blackbody fits within the quoted uncertainties for most events (the uncertainties are quite large as $L_{\rm bol,\,obs}$ is derived from observations in FUV bands only). There is enough energy in our `MOSFiT` predictions to produce the observed FUV luminosity, and for the transients with measured FUV luminosities that are only a factor of a few different from the model predictions, it is likely that a different blackbody radius could reproduce the FUV luminosity. However, for the events with the largest discrepancies between the observations and the model predictions (e.g. PTF09djl), it is clear that a

simple reprocessing model fails to provide a reasonable description of the observed FUV luminosity.

One way to get better constraints on the energy released at late times is to obtain X-ray limits. Two of the events with late-time FUV measurements also have X-ray detections from Jonker et al. (2020). Both PTF09ge and ASASSN-14ae were detected by *Chandra*, strengthening the case made by van Velzen et al. (2019) that the bolometric luminosity of these events remains higher than expected from extrapolations of early time light curves (assuming the X-ray emission does not result from an underlying AGN). As we discuss in Section 3.2, there is further evidence that PTF09ge was more energetic than its initial UV/optical light curve suggests. The bolometric energy estimated from IR dust emission is significantly higher than the estimate from blackbody fits to the light curve (see Table 3.1 and van Velzen et al. (2016a)), which suggests the presence of additional high energy emission missed in the initial observations.

In van Velzen et al. (2019), the authors point out that the late-time FUV observations from flares around larger mass black holes are closer to their predictions from early light curve extrapolations than the observations from smaller mass black holes. The smaller mass black holes required the addition of a second, shallower power law to match the data. However, the timescale of evolution of the light curve is strongly dependent on the black hole mass. Therefore, it is necessary to scale the light curve by the black hole mass in order to effectively compare them. In fact, two of the most extreme under-predictions to observations are for the transients whose late time observations were taken after the largest number of peak timescales (PTF09djl and PTF09ge).

Taken in this context, because the timescales of mass fallback are lengthened for larger mass black holes, the fact that van Velzen et al. (2019) find more dramatic light curve evolution around smaller mass black holes is likely due to the fact that their mass fallback rate (and therefore their reprocessing layers and accretion rates) evolve on shorter timescales.

3.4.2 Comparison to AGN

While it is an important first step towards understanding how energy is generated in TDEs, this work leaves a number of important questions regarding the radiation physics of TDEs and exactly how and where the TDE emission is generated.

The simplest model for TDE emission is thermal radiation from an accretion disk at $R_{\rm t}$, however it fails to accurately describe the observations. It predicts temperatures that are too high by a factor of about 5, and an optical luminosity more than an order of magnitude too dim (e.g., Gezari et al. 2008). This suggests that X-rays from accretion are being reprocessed into the optical part of the spectrum by a debris envelope with a much larger effective photosphere, perhaps 10-100 times $R_{\rm t}$. The origin of the extended gas remains unknown. It has been suggested that a large quasi-static envelope can be supported by radiation pressure (e.g., Loeb & Ulmer 1997). An alternative explanation is that the extended gas instead results from strong accretion disk outflows (e.g., Strubbe & Quataert 2009). Other works have suggested that the luminosity is not powered by accretion at all, but by shocks produced as material falls back, collides, and circularizes at large radii (e.g., Piran et al. 2015). In the absence of radiation transfer studies, it is difficult to distinguish between the proposed theories

of the origin of TDE emission, and several basic questions about the spectrum formation in these environments remain open. As discussed in Section 3.3, estimating the efficiency of conversion between $\dot{M}$ and $L_{\rm bol}$ helps us understand the nature of the processes producing the emission. The theoretically expected efficiencies for accretion disks around non-spinning and maximally spinning super-massive black holes are 0.057 and 0.42 respectively (Novikov & Thorne 1973). Observational studies of AGN have found the mean accretion efficiency for AGN to be $\approx 0.08 - 0.1$ with large variation between individual AGN (Marconi et al. 2004; Davis et al. 2011). It is likely that the efficiency at peak for TDEs is lower than the average efficiency for AGN, simply because many TDEs approach their Eddington limit at peak (as discussed in Section 3.3). However, we might expect the efficiency averaged over the full TDE evolution to be comparable to AGN if the majority of the luminosity is coming from accretion.

In Figure 3.4 (left panel) we compare the average efficiencies estimated by our model with the efficiencies measured for AGN in Davis et al. (2011). There is significant spread in the measured efficiencies for the TDEs in our sample, and we find that while many of the efficiencies we estimate are consistent with AGN efficiencies within the large associated uncertainties, the lowest efficiencies in our sample are much lower than those expected from AGN. We also note that the radii of the innermost stable orbits ($\rm R_{isco}$) for the two most massive events in our sample are larger than the tidal radii for the disruptions of $1 M_{\odot}$ stars. For an accretion disk to form effectively, the disruption would likely need to occur outside of $\rm R_{isco}$, or a significant fraction of the debris will plunge directly into the black hole (Gafton & Rosswog 2019). In principal, this constraint can

help narrow the range of possible stellar masses for TDEs, however in this case, D1-9 and D3-13 prefer masses $\gtrsim 1 M_{\odot}$ in both the fits with the expanded efficiency range used in this paper and the original fits in Mockler et al. 2019a. We note that the trend of increasing efficiency with increasing AGN black hole mass in Davis et al. (2011) has been argued to be due in part to selection effects, however the plotted estimates are thought to be relatively accurate (Laor & Davis 2011; Raimundo et al. 2012).

In Figure 3.4 (right panel) we plot the average efficiencies of our TDE sample versus the circularization radius in units of gravitational radius. We find that most of the efficiencies derived are also consistent within the errors to the maximum possible efficiencies from stream collisions, yet many of the events are in tension with the expected efficiencies from the stream collision model. Assuming gas remains approximately virialized, the maximum fraction of the rest mass energy available for dissipation (and therefore the maximum possible radiative efficiency) at a given radius from the black hole is $\approx 0.5 \times v_{\rm orb}^2/c^2 = 0.5 \times R_{\rm g}/R_{\rm conv}$, where $v_{\rm orb}$ is the orbital velocity for a circular orbit at a given radius, $R_{\rm g}$ is the gravitational radius, and $R_{\rm conv}$ is the radius at which the rest mass energy is dissipated. This is a very conservative limit, and in reality the efficiency from stream collision is likely much lower (as we will discuss in the following paragraphs). Therefore, if most of the early time emission came from stream collisions or circularization processes instead of from accretion, these processes would need to occur close to the black hole for many of the transients in this sample ($\lesssim 100 R_{\rm g}$ for half of the events, see Figure 3.4), and they would need to be very efficient at converting kinetic energy to radiation.

A natural size scale for the accretion disk is the circularization radius ($R_{\rm circ}$). The circularization radius is calculated from the tidal radius and the impact parameter, $R_{\rm circ} = 2R_{\rm p} = 2R_{\rm t}/\beta$, and defines the radius of a circular orbit with the same angular momentum as an eccentric orbit with pericenter radius '$R_{\rm p}$'. The smallest possible radius at which stream collisions could occur is the pericenter radius, however the expected stream collision radius for the most bound debris is always larger than the circularization radius for full disruptions of main sequence stars by Scharwzschild black holes. The radius at which streams collide is dependent on the orbit of the bound debris, which can be approximated using the mass and radius of the star, the mass (and spin) of the black hole, and the impact parameter of disruption (Jiang et al. 2016a; Dai et al. 2015).

For example, given a Schwarzschild $5 \times 10^6 M_\odot$ black hole, $\rm R_{coll} \approx 6 R_{circ}$ for a $0.3M_\odot$ or $1M_\odot$ star, and $\rm R_{coll} \approx 17 R_{circ}$ for a $10M_\odot$ star assuming critical disruptions of both stars ($\beta = 0.9$ for the $0.3M_\odot$ star, $\beta = 1.8$ for the 1 and 10 $M_\odot$ stars; Guillochon & Ramirez-Ruiz 2015a). We see that $\rm R_{circ}$ provides an approximate size scale for the transition between where accretion processes occur and where stream collisions occur.

We conclude that, because stream collisions will generally occur at radii greater than the circularization radii, it is only energetically feasible for events powered by stream collisions to reach the maximum efficiency at the circularization radius (denoted by the dashed line in the right panel of Figure 3.4) if their conversion efficiencies between kinetic energy and radiated energy are larger than 50%. In Jiang et al. (2016a), the conversion rate between kinetic energy and radiated luminosity for stream collisions is

found to be $\approx 2-7\%$ (or $\approx 4-14\%$ of 1/2 of the total kinetic energy – the fraction available to be radiated if the material is virialized), emphasizing that realistic efficiencies for stream collisions are likely much less than 50%.

About half of the events in this sample have efficiency estimates that are comparable to the maximum efficiency at the circularization radius, while the other half have efficiency estimates that are closer to 2-7% of the KE at the circularization radius (of course there are still large systematic uncertainties, as discussed in Section 3.3). We note that the degeneracy in $M_* - \epsilon$ does not significantly change this result, as using a higher/lower efficiency requires a lower/higher stellar mass and the circularization radius increases with stellar mass. Using a lower efficiency requires using a larger circularization radius, and vice versa, moving events diagonally in the $\epsilon - R_{\rm circ}$ plane. More precisely, $R_{\rm circ} \propto M_*^{1/3} R_* \propto M_*^{1/3+\xi}$ – the stellar radius, R_*, can be approximated as $R_* \propto M_*^{\xi}$ with $2/3 \gtrsim \xi \gtrsim 1$ for most zero age main sequence (ZAMS) stars (Tout et al. 1996). Therefore, as you increase/decrease efficiency and decrease/increase M_*, you move along lines in $\epsilon - R_{\rm circ}$ space that are approximately parallel to $\epsilon \propto 1/R_{\rm circ} \propto v_{\rm circ}^2/c^2$. Of course, if the 'scaled' impact parameter is constant (the approximate fraction of mass bound to the black hole remains the same), then the physical impact parameter (β) will change as one changes stellar structure. However, for main sequence stars it will generally not change the circularization radius by more than a factor of ≈ 2, except in the case of super-critical disruptions ($R_{\rm circ} \propto 1/\beta$, and a full disruption of a lower mass ZAMS star occurs at $\beta \approx 0.9$, while a full disruption of a solar mass ZAMS star occurs at approximately $\beta \approx 1.8$).

It remains possible that some fraction of TDEs are powered by stream collisions early on in their light curves, while others are powered by accretion. While it is likely that the flares with the highest measured efficiencies originate at small radii close to the black hole, and the flares with the lowest measured efficiencies originate further from the gravitational radius, it is clearly necessary to reduce the uncertainty in these efficiency estimates before we can derive more stringent conclusions.

3.4.3 Summary and Future Prospects

- In TDEs, a significant fraction of the total energy is radiated at late times. This is because the luminosity is observed to follow the mass fallback rate of stellar debris onto the SMBH. Estimates of the energy radiated during initial observations constitute $\lesssim 50\%$ of the total estimated radiated energy for the majority of the events in our sample (see Table 3.1).

- The late time luminosity ($\gtrsim 10$ peak timescales) extrapolated by assuming the luminosity continues to follow the fallback rate is consistent with the blackbody bolometric luminosities estimated from observations in van Velzen et al. (2019) for 8 out of the 9 events in both samples, but the associated uncertainties are extremely large (see Figure 3.3). In their work, van Velzen et al. (2019) argue that in order to explain the FUV luminosity, the total energy released at late times is significantly larger than the blackbody estimate suggests. If this is proven true with X-ray observations, our conclusion that the energy estimated during UV/optical observations is $\lesssim 50\%$ of the total radiated energy is highly conservative. This

would mean that the corresponding radiative efficiencies need to be larger than those estimated here.

- The efficiency (ϵ) of conversion from mass to radiated energy is somewhat degenerate with the mass of the disrupted star (see Figure 3.1). Calculating this efficiency requires untangling the amount of mass feeding the black hole from the luminosity of the event. The mass fallback rates used in the `MOSFiT` model are self-similar over large ranges of stellar masses (Mockler et al. 2019a), hindering our attempts to isolate the effects of the stellar mass from those of the efficiency on the observed light curve.

- The efficiency (ϵ) of conversion from mass to radiated energy for tidal disruption flares are consistent with AGN efficiencies and, in most cases, with stream collision efficiencies (see Figure 3.4).

- We find that near the peak of the transient light curve, the mass fallback rate is often close to, or greater than, the Eddington mass fallback rate, resulting in peak luminosities that are a significant fraction of the Eddington limits of the black holes (see Figure 3.2). This often requires that the efficiency is reduced near the peak of the light curve (see Dai et al. (2018) for simulation work addressing this efficiency 'suppression'). Therefore estimates of the efficiency comparing the peak bolometric luminosity to theoretical mass fallback rates will likely under-predict the average value of the efficiency.

We have shown that for a TDE with a well-resolved light curve, the num-

ber of potential combinations of star and SMBH properties is significantly reduced. However, when attempting to estimate the conversion efficiency from mass to electromagnetic radiation from a well-resolved light curve, the largest model uncertainty in our measurement comes from the degeneracy between the efficiency and the mass of the disrupted star. Our current mass fallback rates rely on polytropic solutions to stellar density profiles. An important step towards improving our stellar mass estimate is to use mass fallback curves that are based on more accurate stellar structures. There have been several promising developments in this area, as multiple groups have recently produced simulations of disruptions using realistic (MESA) stellar profiles. These studies highlight measurable differences in the shape of the fallback rate curve, particularly for higher mass ($\geq 3M_{\odot}$) stars (Golightly et al. 2019; Ryu et al. 2020; Law-Smith et al. 2020). It is our hope that incorporating this information into our models in future work will make it easier to constrain the mass of the disrupted star, and thus the associated radiative efficiency. Interestingly, Law-Smith et al. (2019) have shown that the composition of the debris that falls back to the black hole changes with time and is dependent on the mass and age of the star. It is thus of paramount importance to improve our understanding of how these composition anomalies might imprint themselves on the observed TDE spectra, so that we can better constrain the stellar mass of the disrupted star. This will enable a better characterization of both the mass to energy efficiency and the properties of the nuclear star clusters that surround the disrupting SMBHs.

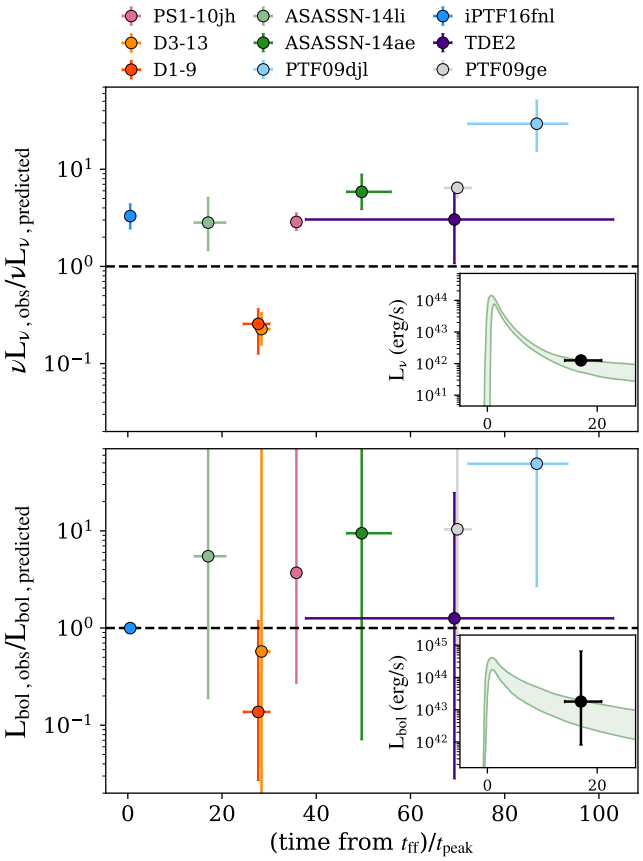

Figure 3.3: We compare the predicted values for νL_ν and L_{bol} from `MOSFiT` to the observed FUV luminosities and corresponding L_{bol} estimates from van Velzen et al. (2019). The 'predicted' values are calculated by extrapolating the `MOSFiT` fits out to the relevant observation times. The x-axis is in units of time from first mass fallback normalized by the peak timescale (this removes the influence M_h has on the light curve timescale). The uncertainties in the model luminosities come from the fits to early-time data (as shown in the inset light curves). The model uncertainties are then added in quadrature with the uncertainties from the observations. *Top Panel:* νL_ν is calculated at $\gamma = 1500$Å. $\nu L_{\nu,\,observed}$ is derived from HST observations with the F125LP and F150LP filters (for 10jh, D3-13, D1-9, 09djl, and 09ge) and from Swift observations in the UVOT filters (for 14li, 14ae, and 16fnl). The `MOSFiT` extrapolation set the minimum photosphere radius to R_{isco}. *Bottom Panel:* To calculate $L_{bol,\,predicted}$, the model efficiency was assumed to be constant at late times. $L_{bol,\,observed}$ was estimated from blackbody fits to observations in the filters listed above. There is significant uncertainty in the estimate of $L_{bol,\,observed}$ due to the lack of SED coverage. 16fnl has a late-time observation in just one filter, therefore $L_{bol,\,observed}$ was calculated using the temperature estimated from blackbody fits at early times and we are thus unable to accurately estimate the associated uncertainties for this measurement. *Inset Plots:* We plot νL_ν and L_{bol} light curves for 14li to give the reader an idea of how the discrepancies between the model and the observations shown in this plot map to a typical light curve. The green shaded curves are the model fits to the early time data, the black points are the late time observations. The x-axes units are the same as for the larger plots.

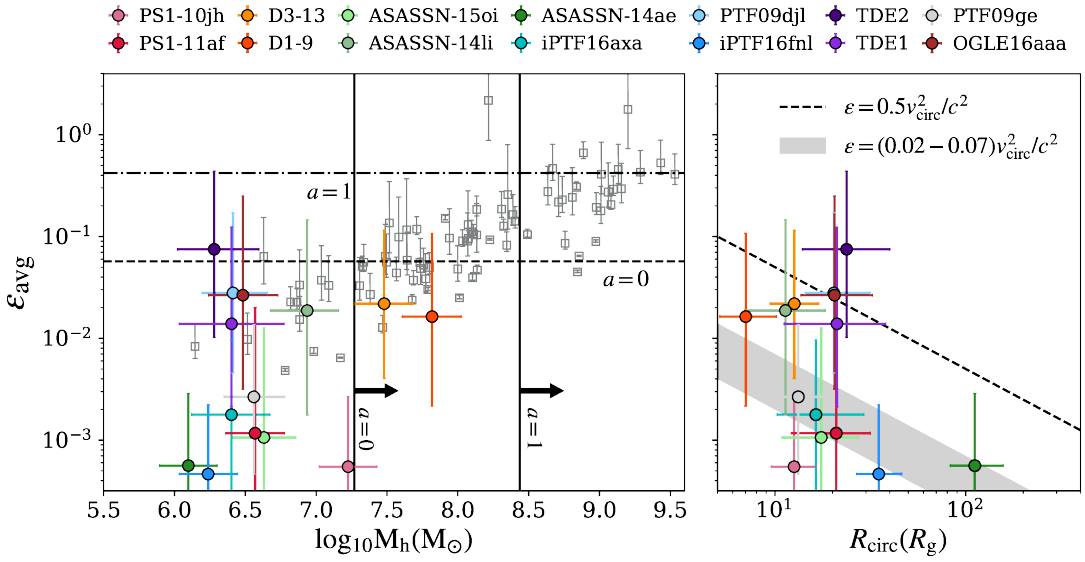

Figure 3.4: *Left Panel:* We compare the average efficiencies (integrated over the full light curve) of our sample of TDEs with AGN efficiencies from Davis et al. (2011) as a function of black hole mass. Our data is plotted as colored circles, while the AGN data from Davis et al. (2011) is plotted as gray squares. The trend of increasing efficiency with increasing black hole mass in the AGN data has been argued to be due at least in part to selection effects (Raimundo et al. 2012; Laor & Davis 2011). We plot two vertical lines denoting where $R_t < R_{isco}$ for a $1M_\odot$ ZAMS star disrupted by black holes with spins of $a = 0$ and $a = 1$ respectively ($R_{isco} = 3R_s$ if $a = 0$, $R_{isco} = 0.5R_s$ if $a = 1$). *Right Panel:* We plot the average efficiencies of our sample versus the circularization radius in units of gravitational radii, with a dashed line denoting the maximum efficiency of conversion between kinetic energy (KE) and radiated energy at a given radius (assuming the gas is virialized post-collision). While the dashed line is the maximum theoretical efficiency of stream collisions at a given radius, simulations by Jiang et al. (2016a) found the stream collision efficiency to be much lower – the radiated energy was $\approx 2-7\%$ of the total KE. If these collisions occur at the circularization radius, we might expect the efficiencies to fall within the gray shaded region in the plot. However, the collision radius of the most bound debris will be much larger than the circularization radius unless the disruption is very deep and the black hole is very large, therefore the efficiency of the stream collisions will likely be much lower ($R_{coll} \approx 6 \times R_{circ}$ for the most bound debris in a full disruption of a solar mass star by a $5 \times 10^6 M_\odot$ Schwarzschild black hole) (Jiang et al. 2016a; Dai et al. 2015; Guillochon & Ramirez-Ruiz 2015a).

3.5 Supplemental Data

Here we include the `MOSFiT` light curves (Figure 3.5) and the `MOSFiT` blackbody fits (Figure 3.6) analyzed in this work. We note that while these fits are quite similar to the fits in Mockler et al. (2019a), there are a few differences as described above in Section 3.3.

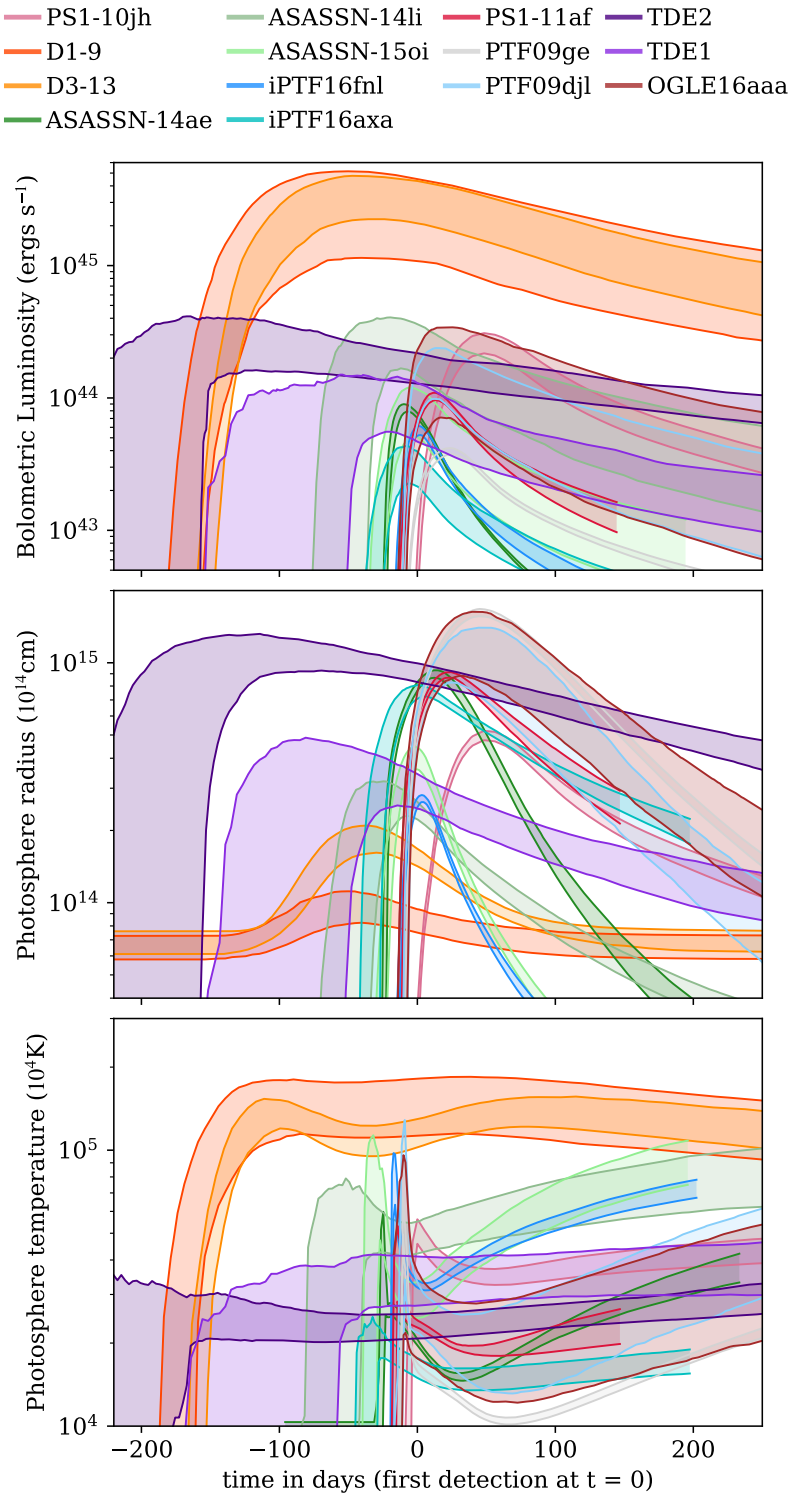

Figure 3.5: Bolometric luminosity, blackbody radius and temperature curves from `MOSFiT` fits to the events in this sample. Time is in rest-frame days from the first observation.

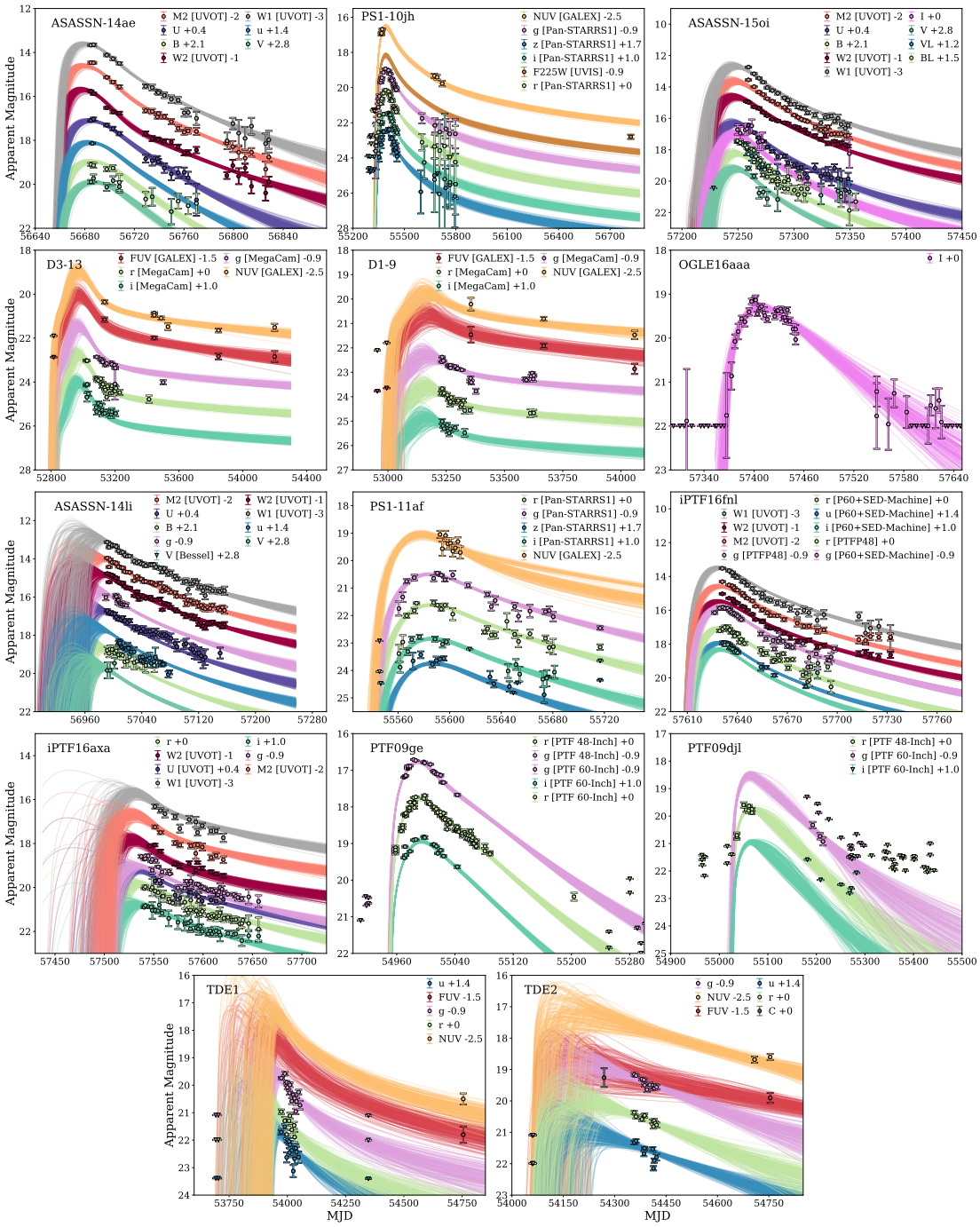

Figure 3.6: Light curves for `MOSFiT` fits used in this paper.

Chapter 4

The Preferential Disruption of Moderately Massive Stars

4.1 Introduction

The gravitational influence of a super-massive black hole dominates the kinematics of stars within a nuclear cluster. Each star within this dense region traces out an intricate trajectory under the combined influence of the SMBH and the other stars. Stellar dynamics is capable of describing the resulting stellar motions as point masses moving under the influence of gravity until these encounters move a star onto a nearly radial orbit. If a star wanders close to the tidal radius it is ripped apart by the SMBH's gravity (Rees 1988). When that happens, the internal structure of the star has to be taken into consideration and we must switch to a hydrodynamic description to follow the evolution of the disrupted stellar debris. A fraction of the debris eventually falls

back, circularizes, and accretes onto the SMBH. This accretion powers a flare which is a clear sign of the presence of an otherwise quiescent SMBH. As we show here, it can also provide a compelling fingerprint of the properties of the disrupted star.

It has only been in the last decade – with the advent of numerous wide field transient surveys – that we have started to collect photometric and spectroscopic data on a myriad of tidal disruption events (TDEs; e.g., van Velzen et al. 2020, and references therein). The discovery of TDE flares has generated widespread excitement, as we can use them to study the masses of SMBHs in quiescent galaxies (Mockler et al. 2019b; Wen et al. 2020; Ryu et al. 2020), the populations and stellar dynamics in galactic nuclei (Kochanek 2015, 2016; Yang et al. 2017), and the physics of black hole accretion (Dai et al. 2018; Bonnerot & Lu 2020; Andalman et al. 2020). The observed rates of TDEs hold important discriminatory power over both the dynamical mechanisms operating in galactic nuclei and the nature of their underlying stellar populations. Both the underlying stellar populations and the dynamical mechanisms that feed stars into disruptive orbits remain uncertain, particularly after the surprising observation that TDEs preferentially occur in an unusual sub-type of galaxies known as E+A galaxies (Arcavi et al. 2014; French et al. 2016; Law-Smith et al. 2017b).

Models of tidal disruption light curves can be used to estimate the parameters of disruption, such as the mass of the black hole and star, and the efficiency of the conversion from accreted mass to observed luminosity (Mockler et al. 2019b; van Velzen et al. 2019; Ryu et al. 2020; Zhou et al. 2021). However, when modeling the light curve, there is a large degeneracy between the efficiency of conversion from mass to energy and

the mass of the disrupted star (Mockler & Ramirez-Ruiz 2021).

Helping constrain the nature of disrupted stars can break the degeneracy between the mass and efficiency as well as provide invaluable insights into the stellar populations and the dynamical processes in galactic nuclei. Recent measurements of metal lines in the UV spectra of a subset of TDEs has provided us with a unique opportunity to uncover the metal content of the reprocessing material. Assuming that the emitting gas originates from the stellar debris, the mass and evolutionary state of the disrupted star can be constrained independently. Measurements of nitrogen-to-carbon UV line ratios are particularly useful for estimating the corresponding abundances in the emitting gas. As the CNO cycle creates a surplus of nitrogen-rich and carbon-deficient material (Kochanek 2015; Gallegos-Garcia et al. 2018; Law-Smith et al. 2019), TDEs from evolved stars could naturally explain enhanced N/C abundance ratios as derived from N^{2+}/C^{2+} line ratios. This argument is particularly robust when considering the UV N III and C III lines, as these elemental transitions have similar critical densities and excitation energies, and involve ions with similar ionization energies (Yang et al. 2017).

In this paper we focus on ASASSN-14li (Holoien et al. 2016b; Cenko et al. 2016; Brown et al. 2017), iPTF15af (Blagorodnova et al. 2019; Onori et al. 2019), and iPTF16fnl (Blagorodnova et al. 2017; Brown et al. 2018), three TDEs whose spectra all have relatively high nitrogen-to-carbon abundance ratios as derived from UV N III/C III line ratios (Yang et al. 2017). For completeness we also include an analysis of ASASSN-18pg (AT2018dyb), which has particularly prominent nitrogen lines in its

optical spectra, but no UV spectra, and therefore the corresponding N/C abundance ratios are more difficult to constrain.

This paper is structured as follows. In Section 4.2 we estimate the location of the nitrogen enriched gas as derived by the equivalent line widths and compare it to the expected location of debris from the disrupted star in order to show whether or not the emitting gas could have originated from the undigested stellar matter as opposed to material present before the flare. In Section 4.3 we show that the super-solar nitrogen abundances single out the disruption of moderately massive ($\gtrsim 1-2M_{\odot}$) stars. To understand this over-representation of moderately massive (or super-solar) stars, in Section 4.4, we study the host galaxies of these TDEs. The host galaxies of all three TDEs are E+A or quiescent Balmer-strong galaxies, suggesting a recent episode of star formation. Finally, in Section 4.5 we present our conclusions and discuss several theories that might explain the over-abundance of high mass disruptions.

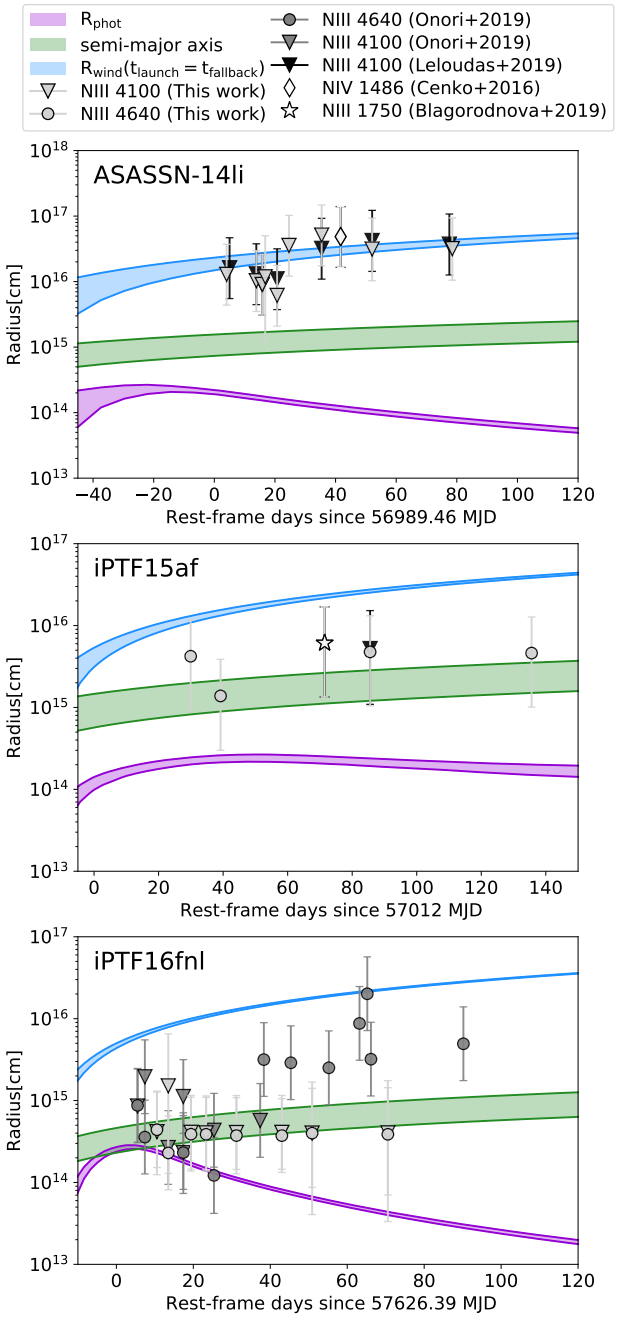

Figure 4.1: The various size scales of gas around the black hole originating from the disrupted star. The blackbody photosphere is plotted in purple, the semi-major axis of debris returning at a given time is plotted in green, and the wind radius (assuming a constant, 0.1c velocity wind launched at first fallback) is plotted in blue. We note that the semi-major axis plotted is a minimum – at any given time, debris that is still orbiting will have larger semi-major axes than debris that has just returned to the black hole. The nitrogen lines appear to emanate from between the photosphere and the wind radius, consistent with originating from the disrupted star. The lines for ASASSN-14li are furthest from the SMBH, but consistent with a wind scenario (see text).

4.2 Lessons learned from light curves and spectra of TDEs

The broad line region (BLR) in many AGN is thought to be produced by gas at distances from light hours to light years away from the SMBH (Blandford & McKee 1982; Vestergaard 2002; McLure & Jarvis 2002). This wide range of scales is in contrast to the debris disk assembly following a TDE. Rather than gas spiraling in from sub-parsec scales, the debris disk forms from the inside out and has an initial characteristic scale of tens of AU (Guillochon et al. 2014). Despite these differences, similar physical mechanisms to those operating in steady-state AGN may also be at work in TDEs. While it is still debated whether the material responsible for the BLR is in the form of a disk wind or clouds, the irradiated gas is thought to be bound to the SMBH with information on the structure and kinematics of this region commonly derived from the broad emission line profiles (e.g., Pancoast et al. 2014a,b, 2018).

Through comparison with the processes responsible for producing the BLR of steadily-accreting AGN together with the commonly held belief that the line width FWHM is related to the rotational motion of the gas, in this Section we infer the location of the nitrogen emitting gas and investigate whether the TDE debris has sufficient time to reach this distance by the time the first spectrum was observed in these events.

Light curve fitting provides rough constraints on the evolution of stellar debris surrounding the SMBH. By estimating the blackbody photosphere, the orbits of infalling debris and the possible launch times for winds with the `MOSFiT` transient fitting code[4], we are able to estimate the size scales of gas structures expected to exist around

[4]the publicly available Modular Open Source Fitter for Transients (`MOSFiT`) uses Markov-Chain Monte Carlo processes to fit analytical and semi-analytical models to multi-band transient light curves,

the SMBH after the TDE occurs (Mockler et al. 2019b). We can then compare these size scales to the virial radii estimated using the FWHM of the nitrogen lines in the TDE spectra. We measured the FWHM for the N III λ4100 and N III λ4640 lines for all events included in this work (see Appendix 4.6.2), and also included the values measured previously in the literature in Figure 4.1. As there is often significant uncertainty in measuring the line widths, including multiple measurements gives a better picture of the systematic uncertainty.

Hydrodynamic simulations of stellar disruptions show the bound debris spreading out in elliptical orbits with size scales dependent on the relative binding energy of the debris to the black hole (Guillochon et al. 2014). If the nitrogen-enriched gas does originate from the disrupted star, we expect it to lie somewhere between the blackbody photosphere radius and the outer edge of an accretion-driven or collisionally-induced wind launched by the return of the most bound material. Most TDEs have peak luminosities within a factor of a few of their Eddington limit (Mockler & Ramirez-Ruiz 2021), and these high luminosities are expected to power strong winds, which efficiently carry mass far from the SMBH (Dai et al. 2018). Additionally, simulations of accretion disk formation show that the super-Eddington mass inflow rates suggest significant mass ejection (Ramirez-Ruiz & Rosswog 2009), and the circularization process can also produce strong, shock-driven winds reaching velocities between $\approx 0.01 - 0.1$c (Lu & Bonnerot 2020).

In Figure 4.1 we plot the virial radii of the nitrogen gas alongside the blackbody photosphere evolution, the semi-major axis of the orbiting bound debris (which increases

extracting the most likely parameter distributions (Guillochon et al. 2018).

with time), and the outer edge of a wind launched at a velocity of 0.1c at the time of first fallback (when debris first returns to the black hole after the star is disrupted). We find that the locations of the nitrogen lines are consistent with debris originating from the disrupted star and its inferred location lies between the photosphere radius and the edge of a fast wind. The nitrogen lines for ASASSN-14li are the farthest from the SMBH, yet consistent with the a wind scenario. This is consistent with other data and modeling of ASASSN-14li. Alexander et al. (2016) and Kara et al. (2018) measured a wind moving at $\gtrsim$0.1c, and van Velzen et al. (2016b) suggest the decay rate of the radio luminosity matches that of a decelerating, mildly relativistic wind.

We note that it is possible the line broadening is due to transport effects instead of kinematics. For example, Roth & Kasen (2018) found that line transport through gas with high optical depths to electron scattering could also broaden lines in TDEs and reproduce observed FWHM velocities. If the measured FWHM values are due to electron scattering or other transport effects and not kinematics, the lines would have to originate at smaller radii (near the edge of the photosphere). This would reduce the similarity with AGN broad line regions, however, the gas could still originate from the stellar debris.

4.3 Lessons learned from composition

The events included in this paper are part of a sub-class of "nitrogen-rich" TDEs that has been assembled in the last few years (Brown et al. 2018; Cenko et al. 2016; Blagorodnova et al. 2019; Holoien et al. 2020; Hung et al. 2017; Hung et al. 2019,

2020, 2021; van Velzen et al. 2021). These events have broad optical N III lines in addition to the more commonly observed He and H emission lines. For at least some events in this sub-class, the N III lines have been theorized to be due to the super-solar nitrogen abundances present in the material of disrupted stars, which is then dispersed and subsequently irradiated by the central SMBH. The reader is referred to Section 4.5 for a discussion on the demographics of TDEs and the fraction of events with clear nitrogen signatures.

The connection between the line strengths and the relative abundances is dependent on the gas conditions where the lines are produced, which are difficult to measure and likely vary within the line-emitting regions as the density and temperature changes with distance to the SMBH. This is the case, for example, when trying to interpret the helium-to-hydrogen line ratios as an indication of the disruption of helium enhanced stars (Roth et al. 2016).

Measurements of nitrogen-to-carbon UV line ratios are, on the other hand, particularly robust for estimating the corresponding abundances in the emitting gas. This is because the N III (λ1750) and C III (λ1908) line transitions have similar critical densities and excitation energies, and involve ions with similar ionization energies (Yang et al. 2017). This means that the line ratio of N III/C III does not depend strongly on the gas conditions of individual TDEs, unlike optical line N strengths. As such, the UV line ratio N III/C III can be used to estimate the abundance ratio of N/C. While a number of TDEs have broad nitrogen lines measured in their optical spectra, the three events discussed in this paper (ASASSN-14li, iPTF15af, and iPTF16fnl) are the

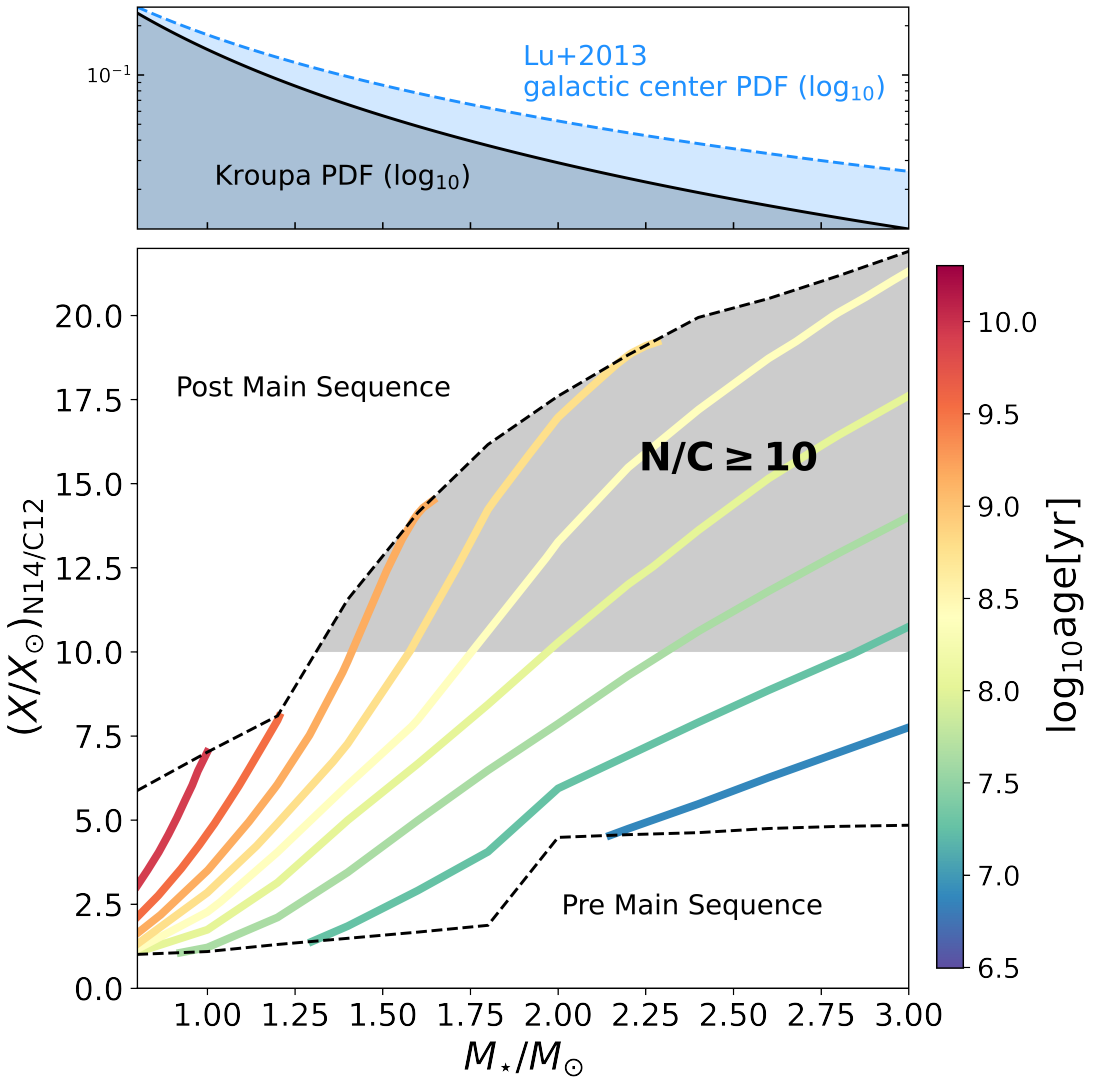

Figure 4.2: Mass versus N/C composition for the tidal debris of main sequence stars. Lines of constant age are plotted in rainbow colors. The shaded gray region denotes stars with N/C $\geq$ 10. The smallest stars that reach this N/C abundance are 1.3 $M_{\odot}$. We focus on stars below $3M_{\odot}$ as they are much more prevalent, however we include higher mass stars in our calculations. We use the fallback models calculated by Gallegos-Garcia et al. (2018), and plot the value of the composition at $t_{fallback} = 0.1 \times t_{fallback,\ peak}$.

only TDEs that have nitrogen lines measured in their UV spectra that can be used to robustly estimate the N/C abundance ratios. All three events occurred relatively close by ($z \leq 0.08$), making them good candidates for HST spectroscopy. They have

luminosities and black hole masses consistent with the general population of observed TDEs. We note that there are 10 TDEs with broad nitrogen lines measured in their optical spectra that do not have HST UV spectra. For comparison, we analyze one of these events (ASASSN-18pg) in Appendix 4.6.1.

In Yang et al. (2017), the authors used the UV N III and C III line ratios measured for ASASSN-14li, iPTF15af, and iPTF16fnl to estimate N/C abundances. They explored the dependence of the abundance ratio calculation on parameters such as the input spectral energy distributions (SEDs), the gas density, and the ionization parameter (U).

Yang et al. (2017) found a strict lower limit of N/C$\geq$10 for ASASSN-14li. This event has the lowest N/C line ratio of any of the three transients, and because of the insensitivity of the line ratio to both U and the shape of the SED, it is argued by Yang et al. (2017) to provide a reasonable lower limit for iPTF15af and iPTF16fnl as well.[5]

The constraints derived on the N/C composition of the stellar debris associated with ASASSN-14li, iPTF15af, and iPTF16fnl can help constrain the masses of the disrupted stars. In Figure 4.2, we plot the stellar mass as a function of the fallback debris composition for main sequence stars at a range of stellar masses and ages. We use the composition dependent mass fallback rates calculated in Gallegos-Garcia et al. (2018) to estimate the maximum N/C abundance ratios that could reasonably be present at the time the UV spectra were taken. The N/C abundance ratio in the debris increases with time, as material that originated closer to the core of the star with higher N/C

[5]ASASSN-14li was brighter than iPTF16fnl, and comparable in luminosity to iPTF15af (Holoien et al. 2016b; Jiang et al. 2016; Blagorodnova et al. 2017; Blagorodnova et al. 2019).

abundance ratios is less bound to the black hole and takes longer to return.

In our calculations, we use the composition of the debris at the time the fallback rate drops to 0.1 of its peak value, which occurs at approximately 10 peak timescales for most full disruptions. This is after the UV spectra were taken; however, we want to be mindful of possible mixing across stellar layers. Hydrodynamical simulations show that mixing can decrease the time for nitrogen-enhanced debris to return to the black hole by a factor of $\approx 2-4$ (Law-Smith et al. 2019). All of the UV HST measurements used in this paper were taken within $\approx$ 2 peak timescales after disruption for their respective transients, and so it is reasonable to use the N/C abundance derived by Gallegos-Garcia et al. (2018) after 10 peak timescales as a strict upper limit to the abundance and, correspondingly, a strict lower limit to the mass of the disrupted star.

Using these models of the composition of fallback debris we find, as expected, that low mass stars at all ages never reach high enough N/C abundance ratios to be compatible with the observed line ratios. We find that the minimum stellar mass with a high enough N/C ratio is $\approx 1.3 M_{\odot}$ (see the gray shaded region in Figure 4.2), which provides us with a strict lower limit. Yet, stars with masses close to $1.3 M_{\odot}$ would need to be near the end of their main sequence lifetimes to have N/C$\geq$10. Stars with masses equal to or above $1.3 M_{\odot}$ are relatively rare – we have plotted the Kroupa IMF and the Lu et al. (2013) galactic center IMF in the top panel of Figure 4.2. In addition to being less common at birth, these stars also have shorter lifetimes than their lighter siblings. Therefore, as the nuclear stellar population ages, high mass stars become subsequently less common if they are not effectively replenished. In Section 4.4 we

analyze the age distributions of the stars residing in the corresponding host galaxies and estimate the disruption probability of stars with N/C≥10 under the assumption that such populations might be representative of the stellar populations present in the nuclei of the galaxies. The validity of this assumption is revisited in Section 4.5.

4.4 Lessons learned from host galaxies

4.4.1 Host galaxy types

Arcavi et al. (2014) and French et al. (2016) reported on the surprising observation that TDEs preferentially occur in an unusual sub-type of galaxies known as E+A galaxies. E+A (or K+A) galaxies are so called due to Balmer absorption features in their spectra (characteristic of an A star) which appear superimposed on an (E)arly-type galaxy population (or old K star; Dressler & Gunn 1983). These galaxies are rare: they comprise only 0.2% percent of the local population, yet host 20% of the optically and UV-detected TDE candidates with measured host galaxy properties to date (Law-Smith et al. 2017b; French et al. 2020). The Balmer absorption in E+A galaxies points to a significant starburst population with ages $10^8 - 10^9$ years, while low Hα indicates a lack of ongoing star formation (Figure 4.3). For this reason, they are also called post-starburst (PSB) galaxies. Galaxies with slightly weaker Balmer absorption, likely due to a smaller recent star formation episode, are generally classified as quiescent Balmer-strong (QBS) galaxies. Following French et al. (2020), we define galaxies with $\mathrm{H}\delta_\mathrm{A} - \sigma(\mathrm{H}\delta_\mathrm{A}) > 4$Å as E+A/post-starburst and galaxies with $\mathrm{H}\delta_\mathrm{A} > 1.31$Å as quiescent Balmer-strong. In both cases we require Hα EW < 3Å. Interestingly, the hosts

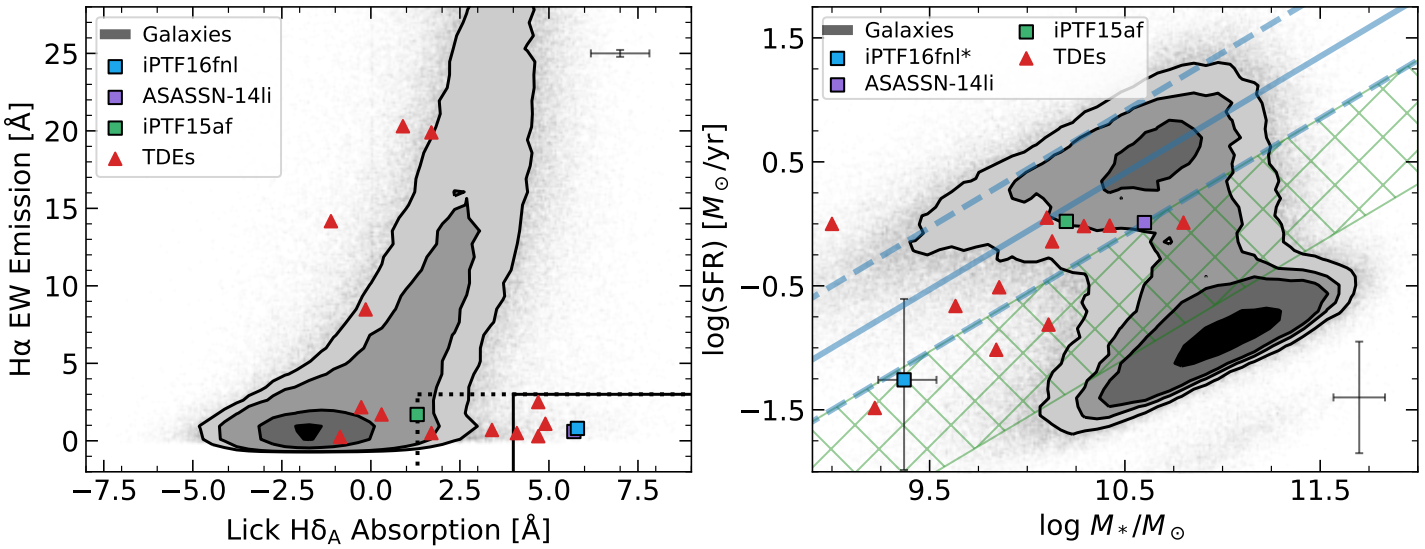

Figure 4.3: The gray contours represent galaxies from the SDSS reference catalog described in Law-Smith et al. (2017b). TDE host galaxies are represented by red triangles, with our sample of 3 TDEs plotted separately using colored squares. **Left panel:** Hα equivalent width as a function of Lick HδA absorption for TDES including those studied in this paper (French et al. 2016; Law-Smith et al. 2017b; French et al. 2020; Dodd et al. 2021). Galaxies inside the solid line box are categorized as E+A/PSB galaxies while galaxies inside the dotted line box are defined as QBS galaxies. **Right panel:** the star formation rate as a function of the total stellar mass. The star forming main sequence is plotted as a blue solid line, the dashed lines represent $\pm$0.5dex, the scatter in the star formation rate measurements used in this plot. Following Law-Smith et al. (2017b) and Pandya et al. (2017), we define the green valley as the region between 1σ and 3σ below the star forming main sequence (plotted in green hatching).

*The SFR for iPTF16fnl has not been measured, and so to estimate a range of likely values we took the range of SFR's for galaxies in our catalog with similar values of HαEW, Hδ_A and stellar mass. In particular, we included galaxies within 1σ in stellar mass and 2σ in Hα EW and Hδ_A (as these galaxies are rare, and there were no galaxies within 1σ).

of the three TDEs with super-solar nitrogen abundances studied here are all quiescent Balmer-strong galaxies, with two of them being E+A or post-starburst. For simplicity we will refer to all of these galaxies with recent starbursts as 'post-starburst', except when the distinction is important to the meaning of the text. TDE host galaxies also have relatively high central concentrations of stellar light, as measured by the steepness of their brightness profiles (Law-Smith et al. 2017b), which is commonly argued to roughly indicate centrally enhanced stellar densities.

As such, nitrogen-rich (N/C $\geq$ 10) TDEs require the disruption of moderately massive ($\geq 1.3 M_{\odot}$) stars, and they appear to occur in the centers of galaxies where two conditions are met: the presence of a relatively recent starburst episode and a large concentration of stellar mass in the central regions. The mechanism by which these moderately massive stars in galactic nuclei are ferried to the very close vicinity of the SMBH remains an open question. There have been several theories put forward to explain the enhanced TDE rate in post-starburst galaxies, from an over-density of stars close to the SMBH (Law-Smith et al. 2017b; Stone et al. 2018), to the presence of SMBH binaries (Chen et al. 2011; Arcavi et al. 2014; Li et al. 2015), to star formation in eccentric disks around SMBHs (Madigan et al. 2018). What these theories share in common, is that the disrupted stars come from within the radius of influence of the SMBH. Deep in the potential of the black hole, stars gravitationally interact with one another coherently, in contrast to two-body relaxation, resulting in rapid angular momentum evolution (Rauch & Tremaine 1996). This rapid evolution allows for moderately massive stars to be disrupted before they can significantly evolve. In what follows

we assume that the stellar populations of galaxy nuclei resembles that of the host in order to make inferences about the rate enhancement required to explain the inferred N/C abundance ratios.

4.4.2 Stellar population content in TDE hosts

To estimate the number of stars that can produce nitrogen-rich tidal disruptions (defined here as tidal debris with N/C$\geq$ 10), we first calculate the relative number of moderately massive main sequence stars present in the corresponding hosts. As shown in Figure 4.2, if we can calculate the masses and ages of the stellar population, we can determine what percentage of the stellar population could have a significant nitrogen enhancement if disrupted. As all three of the events in our sample reside in post-starburst galaxies, we investigate whether the recent starbursts can help explain the disruption of moderately massive stars.

We make use of the star formation histories derived in French et al. (2017) for the host galaxies of ASASSN-14li and iPTF15af, together with a Kroupa initial mass function (Kroupa 2001) to get the masses and ages of the overall stellar populations in these galaxies (we also vary the IMF to better represent galactic nuclei, as described below). We do a separate analysis of the stellar population in iPTF16fnl, as this galaxy does not have as detailed of constraints on its star formation history. Following French

et al. (2017), we use

$$\Psi \propto te^{-t/\tau_{\rm o}}; \qquad t < 10^{10} - t_{\rm y}$$
$$\propto te^{-t/\tau_{\rm o}} + \beta e^{-(t+t_{\rm y}-10^{10})/\tau_{\rm y}}; \qquad t \geq 10^{10} - t_{\rm y},$$

to jointly model the old stellar population's star formation history combined with the young stellar population's recent starburst. We assume a linear-exponential star formation rate for the old stellar population, beginning 10 Gyr ago ($t = 0$) with a characteristic timescale $\tau_{\rm o} = 1$Gyr. The young starburst is modelled as an exponential decline in star formation rate that started $t_{\rm y}$ years ago with a characteristic timescale $\tau_{\rm y}$ as determined by fits to spectroscopic observations. The normalization factor between the old and young starburst, β, ensures the total fraction of stars from the young starburst is consistent with the corresponding burst mass fraction determined from observations. The host of ASASSN-14li (iPTF15af) has $t_{\rm y} = 473^{+373}_{-67}$ Myr ($t_{\rm y} = 595^{+108}_{-191}$ Myr), $\tau_{\rm y} = 25 - 200$Myr ($\tau_{\rm y} = 25 - 100$Myr) and a burst mass fraction $= 0.055^{+0.016}_{-0.016}$ (burst mass fraction $= 0.005^{+0.002}_{-0.002}$), as derived by French et al. (2017).

We then use the relative likelihood of disruption based on each star's mass and radius. Higher mass stars and more evolved stars are slightly easier to disrupt, as they are less dense, which translates to a more extended tidal radii, $R_{\rm t}$. We use the rate estimate described in MacLeod et al. (2012) to determine the corresponding mass weighting:

$$\frac{dr}{dM_*} \propto R_{\rm t}^{1/4} \frac{dn}{dM_*} \propto \frac{R_*^{1/4}}{M_*^{1/12}} \frac{dn}{dM_*} \tag{4.1}$$

As described above, the stellar population, dn/dM_*, is calculated using the star formation rates estimated in French et al. (2017). We use `MIST` (Dotter 2016; Choi et al. 2016; Paxton et al. 2011, 2013, 2015) to calculate the mass-radius relation as a function of stellar mass and age (with the zero age main sequence metallicity set to solar metallicity using the Asplund et al. (2009) value of Z = 0.0142). For simplicity we first proceed under the assumption that the diffusion coefficients for a given SMBH environment are mass independent and that any changes in the tidal disruption rate arises solely based on differences in the mass-dependent cross section (see Section 4.5 for further discussion).

4.4.3 On the preferential disruption of $\geq 1.3M_\odot$ stars

After weighting the stellar populations by the relative likelihood of disruption as a function of stellar mass, we are able to integrate over the range of stellar masses and ages that can produce the observed N/C line ratios. As such, we can calculate the fraction of stars that satisfied these constraints under the assumption that the overall stellar population of the host is representative of that of the nuclei.

In Figure 4.4 we plot the relative number of stars as a function of mass and age, and include contours defining the region where the N/C abundances are $\geq$ 10. Most of the stars were formed $\approx$ 10 Gyrs ago while the recent starbursts in the hosts can be seen around 300 - 500 Myrs ago, where there is a significant increase in the number density of stars. In the host of ASASSN-14li, the percentage of stars in the entire stellar population that can produce tidal debris with N/C$\geq$ 10 is $0.028^{+0.008}_{-0.008}$% (the gray shaded region), although it rises to $8.2^{+1.4}_{-2.9}$% if we only consider stars in the

young starburst (the hatched region). In the host of iPTF15af, the percentage of stars is $0.0045^{+0.0009}_{-0.0009}\%$ in the entire stellar population, and $7.1^{+1.8}_{-0.7}\%$ when only considering stars within the recent starburst.

In brief, the percentage of stars in the entire galactic population with sufficiently high N/C abundances to explain the observations is, as expected, very small. However, it increases significantly if the population of disrupted stars resembles those produced solely by the recent starburst. This would help to explain the observations without requiring a model that preferentially disrupts moderately massive stars (as we discuss further in Section 4.5).

It is also possible that the Kroupa IMF does not provide an accurate description for the distribution of stars in galactic nuclei. Lu et al. (2013) measured the properties of the stellar population in the galactic center and found it to be best described by a top-heavy IMF. They find a best fit power law 'α' index of $1.7^{+0.2}_{-0.2}$, compared to the Kroupa value of $\alpha = 2.3$ (Kroupa 2001). Substituting $\alpha = 2.3$ for $\alpha = 1.7$ for stars $\geq 0.5 M_{\odot}$, we find that the percentage of stars with N/C ≥ 10 increases by a factor of ≈ 2. This brings the percentage to $0.06^{+0.02}_{-0.02}\%$ for the host galaxy of ASASSN-14li, and to $0.009^{+0.002}_{-0.002}\%$ for the host galaxy of iPTF15af. Again, if we only look at the stars belonging to the recent starburst in each galaxy, the percentages are $15.2^{+2.9}_{-5.4}\%$ for the host of ASASSN-14li and $13.2^{+3.3}_{-1.3}\%$ for the host of iPTF15af.

Although there are no measurements of the star formation history for the host galaxy of iPTF16fnl, we can use the average age measured for the stellar population of the host to estimate the fraction of stars that fit our criteria. Two papers have measured

the age of the host. Blagorodnova et al. (2017) estimates an age of 650^{+300}_{-300} Myr while Brown et al. (2018) estimates an age of $1.29^{+33}_{-0.3}$ Gyr. We estimate the percentage of stars with N/C $\geq$ 10 for both ages, and find a range of 2.7-8.6% using the Kroupa IMF, and 4.6-15.3% using the Lu et al. (2013) galactic center IMF. This of course assumes all stars in the galaxy formed at this age and as such it provides a strict upper limit.

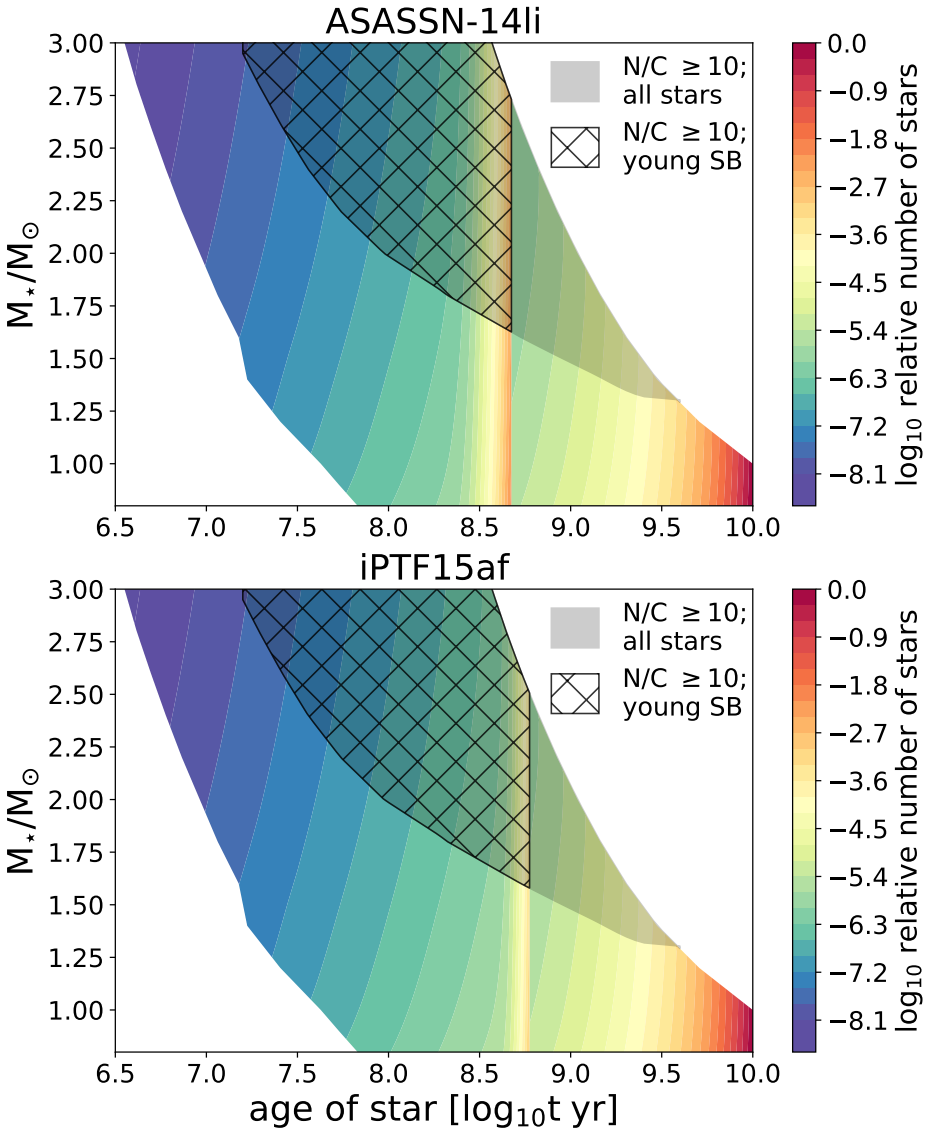

Figure 4.4: The relative number of main sequence stars in the host galaxies of ASASSN-14li and iPTF15af are plotted. We use the star formation rates for these galaxies as calculated by French et al. (2017) to determine the relative population of young and old stars. We also weight the stellar population using the expected mass-dependent disruption cross section. We then calculate the N/C ratio in the tidal debris of each of these stars, using the formalism developed by Gallegos-Garcia et al. (2018). In the host of ASASSN-14li, the percentage of stars with N/C$\geq$ 10 is $0.028^{+0.008}_{-0.008}$% in the entire stellar population of the host, and $8.2^{+1.4}_{-2.9}$% in the recent starburst. In the host of iPTF15af, the percentage of stars with N/C$\geq$ 10 is $0.0045^{+0.0009}_{-0.0009}$% in the entire stellar population, and $7.1^{+1.8}_{-0.7}$% in the recent starburst.

4.5 Discussion

4.5.1 Assessing the ubiquity of N-rich TDEs

To determine the rarity of these moderately massive stellar disruptions, defined here as disruptions with $M_* \geq 1.3 M_\odot$, we must look at the entire TDE population. We have observations of ≈50 confirmed TDEs (Auchettl et al. 2018; van Velzen et al. 2021). Only six TDEs have HST UV spectra, and of those, the three TDEs discussed in this paper (≈6% of the population) have high N/C abundance ratios as inferred from their UV spectra. There are ~ 10 other TDEs that have nitrogen lines present in their optical spectra but lack UV spectra (such as ASASSN-18pg). It is certainly possible that these events are also nitrogen-rich, which makes the derived fraction of 6% a strict lower limit. Nevertheless, 6% is well in excess of the fraction of stars that could produce these nitrogen abundances ($\approx 0.0005\% - 0.06\%$) if the populations of disrupted stars is selected randomly from the total stellar population of the host. The fraction of stars able to produce these nitrogen abundances drastically increases if the disrupted stars are drawn from the recent starburst population. Motivated by this, we look more closely at the percentage of moderately massive disruptions among TDEs in galaxies with recent starbursts, instead of simply looking at the percentage of of these disruptions among all TDEs.

In a recent review paper, French et al. (2020) found that of the 41 TDE candidates with derived host galaxy properties, 5 of them were discovered in post-starburst galaxies and 13 were discovered in either quiescent Balmer-strong or post-starburst galaxies. This implies that 2/5 (40%) of TDEs observed in post-starburst galaxies and

3/13 (23%) of TDEs observed in quiescent Balmer-strong galaxies have enhanced nitrogen abundances, as inferred by their UV spectra. This is still higher than the fraction of stars that could produce the measured nitrogen abundances in these galaxies, even if all of the disrupted stars came from the recently formed population of stars ($\approx 7-15\%$ for iPTF15af and ASASSN-14li). What is more, this is a lower limit, given that there is not UV spectra for the other events in QBS galaxies. As such, this implies an enhanced disruption rate of moderately massive stars (key to determining the mechanism responsible for transporting stars near the SMBH).

4.5.2 Theories for TDE enhancement

Several theories have been put forward to explain the enhanced TDE rate in post-starburst galaxies, and it is possible that these might also help explain the overabundance of moderately massive stellar disruptions in post-starburst galaxies. The TDE enhancement can be ascribed to a dynamical mechanism that preferentially transports and disrupts moderately massive stars and/or to an overabundance of moderately massive stars in galactic nuclei.

Star formation in galactic nuclei

One possible explanation is that the general stellar population of stars in a starburst galaxy is not representative of that in its nucleus. For example, Norton et al. (2001); Yang et al. (2008) found that in E+A galaxies the Balmer absorption features become more prominent as one moves radially inward. Building on this work, Pracy et al. (2012, 2013) found that the young stellar populations in nearby E+A galaxies have

centrally concentrated gradients. This matches what simulations predict for a starburst caused by a gas-rich merger, as cold gas is funnelled into the center of the galaxy, triggering a nuclear starburst (Mihos & Hernquist 1994; Bekki et al. 2005; Hopkins & Hernquist 2009). Interestingly, we also observe elliptical galaxies with blue cores (Menanteau et al. 2001; Pipino et al. 2009), and dwarf galaxies that possibly experienced nuclear starbursts Sánchez-Janssen et al. (2019), which indicates that the disruption of moderately massive stars can still take place in galaxies with no apparent star formation. The reader is referred to the discussion of the TDE ASASSN-18pg in Appendix 4.6.2.

As previously discussed in Section 4.4, an increased fraction of young stars in the cores of these galaxies can help explain the overabundance of TDEs arising from the disruption of moderately massive stars. However, in some cases, there are not enough super-solar stars to explain observations even when assuming that all of the stars in the core are from the galaxy's most recent starburst. In Section 4.4 we also showed that a further enhancement can be produced if the IMF of stars in galactic nuclei is top-heavy (compared to a Kroupa IMF), as inferred for the Milky Way's galactic center (Lu et al. 2013) and predicted in extreme star forming environments (Larson 2005; Hennebelle & Chabrier 2008; Bate 2009). Unfortunately, it is difficult to study this observationally – the lowest mass stars we are currently able to observe in our own galactic center are $\gtrsim 2M_{\odot}$ (Hosek et al. 2019). If we assume, for example, a low-mass cutoff of $\gtrsim 0.5M_{\odot}$ in addition to using a top-heavy IMF slope and assuming that stars in galactic nuclei are drawn from the young stellar galactic population, then the percentage of stars with N/C abundances $\gtrsim 10$ that are available to be disrupted in the hosts of iPTF15af and

ASASSN-14li would increase to around $\approx 20\%$. This would be in close agreement with observational constraints. JWST will be key for testing these theories as it should be able to resolve $\approx 0.3 M_{\odot}$ stars in the Arches cluster near the galactic center (Hosek et al. 2019).

It is also possible that stars in galactic nuclei are younger than those associated with the overall starburst episode. The Arches cluster in the galactic center, for example, underwent recent star formation (around 2-5 Myr ago, Paumard et al. 2006; Negueruela et al. 2010; Gennaro et al. 2011; Lu et al. 2013), and measurements of the star formation history in the galactic center are consistent with quasi-continuous star formation (Schödel et al. 2020). The conditions in the galactic nuclei are thought to be similar to the conditions in highly star forming starburst episodes (Ginsburg et al. 2016). This would obviously increase the number of moderately massive stars available for disruption, although it would not necessarily increase the percentage of stars with high N/C abundances, as stars below $\approx 2 M_{\odot}$ take ≈ 100 Myr to develop such enhancements (see Figure 4.4).

Dynamical mechanisms leading to TDEs

Another potential explanation for the observed TDE enhancement is that the leading dynamical mechanisms at work in these galactic nuclei are preferentially increasing the rate of high mass disruptions. Mass segregation has been observed in star clusters for stars above $\approx 5 M_{\odot}$ (Hillenbrand & Hartmann 1998; Gennaro et al. 2011), although it is unclear whether this can be solely explained by two-body relaxation or if the actual star formation process needs to be altered (Parker et al. 2011; Dib et al.

2018; Plunkett et al. 2018). Two-body relaxation is commonly assumed to be responsible for moving stars onto loss-cone orbits (Wang & Merritt 2004; Stone & Metzger 2016), and for galaxies where it is the dominant mechanism for producing TDEs, some mass segregation is to be expected (Allison et al. 2009). Calculating the dynamics of a non-homogeneous population of stars requires N-body simulations, and there is not a simple analytical adjustment to the rates as a function of stellar mass. Simulations have found that the highest mass stars generally follow a Bahcall-Wolfe density profile ($r^{-\alpha}$; $\alpha \approx 1.75$, Bahcall & Wolf 1977), while the total stellar mass follows a shallower profile ($\alpha \approx 1.5$, Baumgardt et al. 2004; Vasiliev 2017). Direct N-body simulations of multi-mass star clusters containing intermediate-mass black holes by Baumgardt et al. (2004) found that α increased from 0.7 for $\approx 0.1 M_\odot$ stars to 1.7 for $\approx 1 M_\odot$ stars, so that the average mass of stars in the core was $\approx 0.6 M_\odot$ and their simulations show a clear preference for the disruption of $\gtrsim 0.6 M_\odot$ stars. Yet, it remains unclear if mass segregation in galactic nuclei could explain the observed preference for moderately massive stellar disruptions.

Another dynamical alternative is that these galactic nuclei host eccentric nuclear disks (such as the one in Andromeda, Tremaine 1995). Madigan et al. (2018) and Wernke & Madigan (2019) found that eccentric nuclear disks, which could originate in galaxy mergers (Hopkins & Quataert 2010), can dramatically increase the rate of tidal disruption events. Galaxies that experienced recent starbursts are good candidates for recent galaxy mergers, as mergers funnel gas to the centers of galaxies and drive up star formation (Barnes & Hernquist 1991). Additionally, Foote et al. (2020) found that

radial mass segregation takes place within eccentric nuclear disks, implying that they would naturally produce a higher fraction of high mass stellar disruptions than would be predicted from the underlying stellar population. Therefore, eccentric nuclear disks would not only increase the total rate of disruptions in post-merger galaxies, but could also help explain the relative rate of disruptions of moderately massive stars.

Two other dynamical mechanisms that could help increase the rate of tidal disruptions in post-merger galaxies are the Kozai-Lidov (KL) mechanism and the eccentric Kozai-Lidov (EKL) mechanism (Chen et al. 2011; Li et al. 2015). These mechanisms are a natural consequence of the presence of a SMBH binary assembled after a galaxy merger. A star orbiting one of the SMBHs will be perturbed by the second SMBH, and this perturbation can cause the stellar eccentricity and inclination to undergo periodic oscillations, potentially ending in the star being disrupted. Both the KL and EKL mechanisms have been explored as ways to increase the total number of disruptions in post-starburst galaxies (Stone et al. 2018; Mockler et al. 2021). Both mechanisms can help increase the rate of TDEs after a merger, but their efficacy depends on stars within the sphere of influence of the SMBH binary being effectively replenished through, e.g., regulated star formation. Neither of these mechanisms preferentially disrupt higher mass stars on their own, however if they are combined with top-heavy star formation or the formation of nuclear disks, it is possible they could explain both the enhanced rate of TDEs in post-starburst galaxies and the overabundance of moderately massive disruptions in these galaxies.

Regardless of the true mechanism (or mechanisms) for increasing the rate of

moderately massive tidal disruptions, we expect our understanding of nuclear stellar clusters will continue to be challenged and enhanced by TDE discoveries.

4.6 Supplemental Data

4.6.1 TDE ASASSN-18pg

The TDE ASASSN-18pg has optical nitrogen lines observable through much of its evolution (Leloudas et al. 2019). We find that these nitrogen lines are consistent with originating from the tidally disrupted star (Figure 4.5, top panel), although without UV spectra it is difficult to determine how the line strength is connected to the star's composition. Unlike the other TDEs analyzed in this paper, ASASSN-18pg was not discovered in a post starburst galaxy but in an elliptical one (Figure 4.5, bottom panels). We note that there are $\approx$ 10 TDE candidates (including ASASSN-18pg) that have nitrogen measured in their optical spectra but lack UV spectra. Four of these have host galaxy classifications, and of these, one occurred in a post starburst galaxy and three were found in quiescent galaxies. If the associated nitrogen lines are due to the disruption of a moderately massive star, then this implies that the cores of these quiescent galaxies contain younger stars. This is consistent with the seminal results from Menanteau et al. (2001) showing that some quiescent galaxies have blue cores.

4.6.2 Nitrogen emission line analysis

To constrain the size scales of the nitrogen rich material, we take advantage of the publicly available optical spectra for ASASSN-14li (Holoien et al. 2016b; Cenko

et al. 2016; Brown et al. 2018), iPTF15af (Blagorodnova et al. 2019; Onori et al. 2019), iPTF16fnl (Blagorodnova et al. 2017; Brown et al. 2018) and ASASSN-18pg (Leloudas et al. 2019; Holoien et al. 2020). Here we constrain the radii and evolution of this gas using the full-width half max (FWHM) of the nitrogen emission lines detected in these events. As discussed in e.g., Holoien et al. (2020); Charalampopoulos et al. (2021), line profile fitting can be complicated due to the broadness of the lines, blending of nearby emission lines, the signal to noise of the spectra, and the different methods of analysis presented in the literature. As such, rather than taking solely taking the FWHM of these lines from the literature, we re-analyse the spectra of each source using a consistent method as presented below.

As we are most interested in the emission lines of these events, we first model the continuum emission of each spectrum using the Astropy package, *specutils*[6]. The spectra is smoothed using a median filter to minimise any extreme variations in the spectra. The continuum is then fitted using a low-order Chebyshev polynomial of the 1st kind. To obtain the normalised spectra which we use for our analysis, we divided our smoothed spectra by our best fit continuum model. This method allows us to better determine the evolution of these lines in terms of their equivalent width and strengths relative to continuum. As we do not correct our spectra for host contribution, we note that this method may not fully remove host emission and this is one of the main sources of our systematic errors. Note that Holoien et al. (e.g., 2020) suggest that the uncertainty in identifying and removing continuum emission can correspond to over 25% of the error estimate.

[6] https://specutils.readthedocs.io/en/stable/

To constrain the FWHM of the nitrogen lines (and other lines present in the spectrum between 3900Å and 5200Å), we fit each emission line profile using a simple Gaussian, similar to what is done in the literature (e.g., Hung et al. 2017; Blagorodnova et al. 2019; Leloudas et al. 2019). For N III (4640 Å), which is blended with He II (4686 Å), we fit both lines simultaneously. While additional components or the use of a Lorentizian model may be more physically motivated or better describe the data (see Charalampopoulos et al. 2021, for more discussion), a simple Gaussian model is sufficient for our purposes.

To perform this fit, we use Markov Chain Monte Carlo (MCMC) methods. Here we let the amplitude of the emission profile, standard deviation, and the wavelength of the center of the peak vary, but set uniform priors for each parameter to ensure convergence. Using the best fit values, we derive the velocity width or FWHM (and the velocity shift from the rest wavelength) for each line and derive 90% confidence error intervals for these parameters. In Figure **??** we show examples of the best fit models derived from our analysis of each event, while in Table 4.1 we list the best fit FWHM for each nitrogen line and their uncertainties. We find that our method produces similar results to those found in the literature (see Figure 4.1 and 4.5).

Table 4.1: The derived emission line widths of N III 4100Å and N III 4640Å for each tidal disruption event in our sample.

TDE	Spectrum	Data of observation	Days since TDE discovery	N IIII 4100 FWHM (km/s)	N IIII 4100 FWHM uncertainty	N III 4640 FWHM (km/s)	N III 4640 FWHM uncertainty
ASASSN-14li	APO 3.5m	2014-12-02	10	3300	81	6317	4069
ASASSN-14li	MDM 2.4m	2014-12-09	17	–	–	6019	406
ASASSN-14li	MDM 2.4m	2014-12-10	18	–	–	5740	1805
ASASSN-14li	APO 3.5m	2014-12-12	20	3691	66	6085	237
ASASSN-14li	FLWO 1.5m	2014-12-14	22	3939	19	6074	1054
ASASSN-14li	FLWO 1.5m	2014-12-15	23	3444	2192	6047	835
ASASSN-14li	FLWO 1.5m	2014-12-19	27	4776	16	6070	491
ASASSN-14li	MDM MODS 2.4m	2014-12-23	31	1984	23	2812	42
ASASSN-14li	Magellan Baade	2015-01-03	42	1652	19	1865	46
ASASSN-14li	LBT MODS	2015-01-20	59	2113	277	1508	26
ASASSN-14li	MDM 2.4m	2015-02-11	81	–	–	7572	463
ASASSN-14li	LBT MODS	2015-02-16	86	2099	251	3367	881
ASASSN-14li	MDM 2.4m	2015-03-11	109	–	–	–	–
ASASSN-14li	LBT MODS	2015-04-17	146	–	–	2209	27
iPTF15af	Keck LRIS	2015-01-22	7	–	–	13009	267
iPTF15af	FLOYDS North	2015-02-01	17	–	–	22728	2024
iPTF15af	Keck LRIS	2015-02-23	67	–	–	12240	176
iPTF15af	Keck LRIS	2015-05-16	121	–	–	12448	73
iPTF15af	Keck LRIS	2015-06-13	149	–	–	12422	862
iPTF15af	Keck LRIS	2017-11-15	1035	–	–	12447	392
iPTF16fnl	Nordic Optical Telescope	2016-08-31	5	10238	2750	9960	1133
iPTF16fnl	Nordic Optical Telescope	2016-09-03	8	5377	3617	13802	473
iPTF16fnl	Nordic Optical Telescope	2016-09-09	14	10332	103	10603	373
iPTF16fnl	Nordic Optical Telescope	2016-09-13	18	10404	43	10618	296
iPTF16fnl	Nordic Optical Telescope	2016-09-21	26	10359	366	10815	1455
iPTF16fnl	Nordic Optical Telescope	2016-10-03	38	10338	76	10819	255
iPTF16fnl	Nordic Optical Telescope	2016-10-11	46	10440	6686	10453	4485
iPTF16fnl	Nordic Optical Telescope	2016-10-31	66	10406	7058	10621	5226
AT2018dyb	SOAR Goodman	2018-07-17	6	10994	294	6066	2632
AT2018dyb	Nordic Optical Telescope	2018-08-03	23	11076	1062	10295	5057
AT2018dyb	Nordic Optical Telescope	2018-08-13	33	9519	404	9413	820
AT2018dyb	Nordic Optical Telescope	2018-08-18	38	8949	373	9518	1384
AT2018dyb	Nordic Optical Telescope	2018-09-01	52	7520	433	12008	4046
AT2018dyb	Nordic Optical Telescope	2018-09-15	66	6875	273	16784	7261
AT2018dyb	Nordic Optical Telescope	2018-10-02	83	6439	2192	19905	10359
AT2018dyb	Nordic Optical Telescope	2018-10-18	99	10981	6954	7597	4030

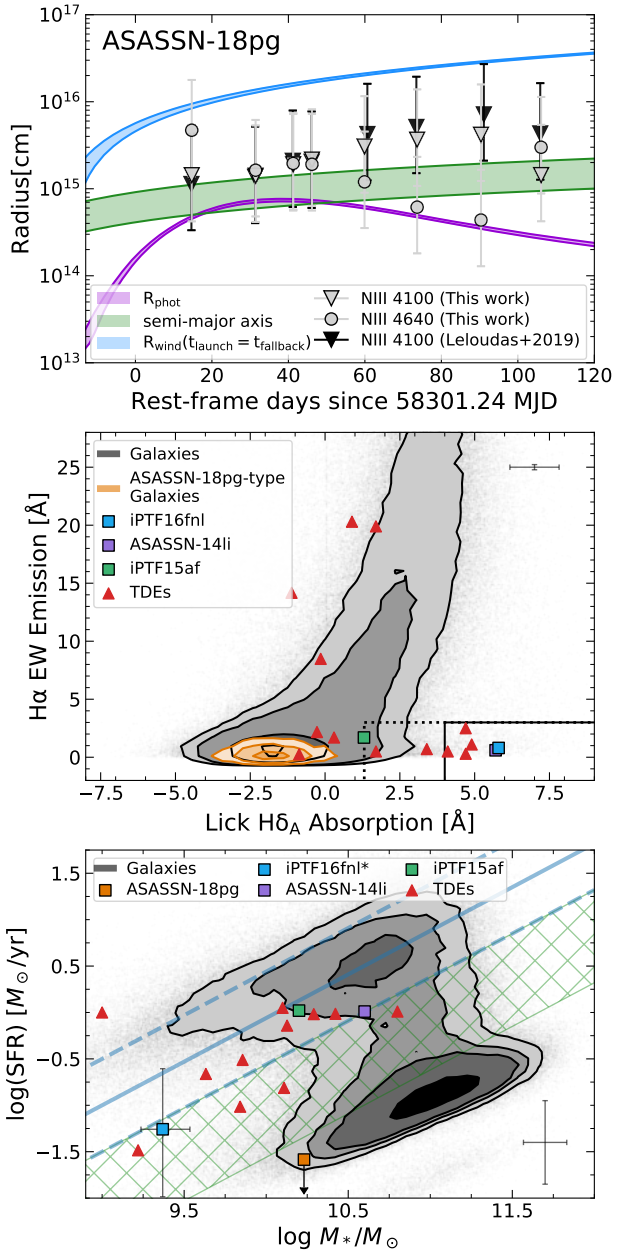

Figure 4.5: Analogous to Figures 4.1 and 4.3, see relevant figure captions for further description. **Top panel:** The blackbody photosphere is plotted in purple, the semi-major axis of debris returning at a given time is plotted in green, and the wind radius is plotted in blue. **Middle panel:** Hα equivalent width as a function of Lick HδA absorption. Galaxies inside the solid line box are E+A/PSB, galaxies inside the dashed line box are QBS. Because there are not measurements of Hα EW or Lick HδA for the host of 18pg, we estimated their likely range by taking the distribution of these parameters for galaxies with similar values of M_* and SFRs. We used galaxies within 1σ in stellar mass that had star formation rates consistent with the upper limit for the host of 18pg. **Bottom panel:** The star formation rate as a function of the total stellar mass.

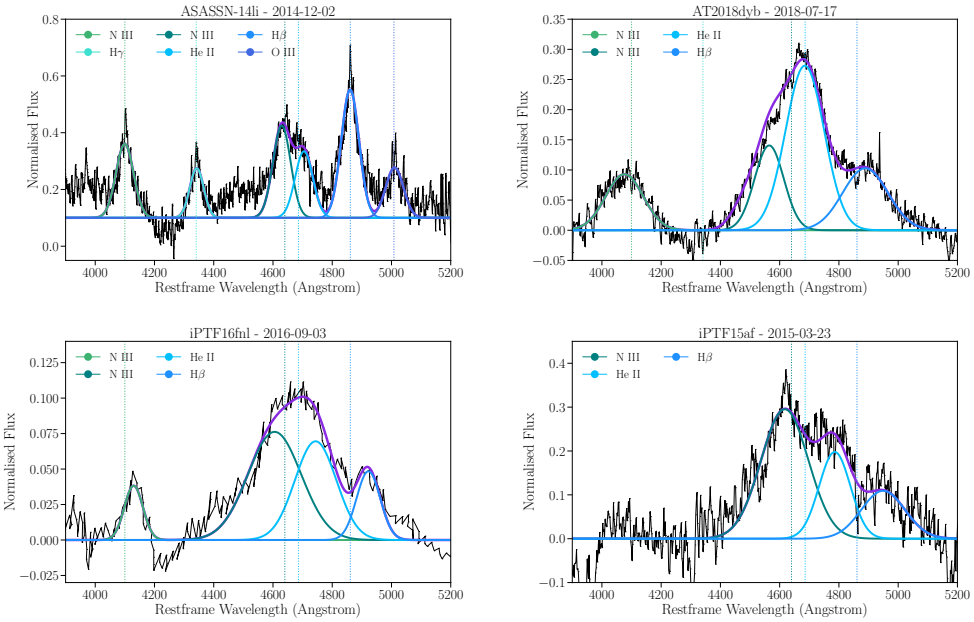

Figure 4.6: Example best fit models obtained by simultaneously fitting multiple Gaussians in the spectrums of ASASSN-14li (taken using APO 3.5m on 2014-12-02), AT2018dyb (taken using SOAR on 2018-07-17), iPTF16fnl (taken using the Nordic Optical Telescope on 2016-09-03) and iPTF15af (taken using Keck LRIS on 2015-05-23), respectively. The central wavelengths of each emission lines (assuming zero velocity) are marked by vertical dotted lines.

Chapter 5

The enhancement of TDEs from SMBH binaries

5.1 Introduction

After two galaxies merge, the central supermassive black holes (SMBHs) will eventually sink to the bottom of the merged galaxy's potential, where they will form a binary system in the nucleus of the galaxy. While the two SMBHs coexist, they will induce orbital perturbations in each others' nuclear star clusters which can send stars on high eccentricity, nearly radial orbits towards one of the black holes and lead to increased rates of tidal disruptions events (e.g. Ivanov et al. 2005; Chen et al. 2011; Wegg & Nate Bode 2011; Li et al. 2015; Sari & Fragione 2019) Tidal disruption events (TDEs) occur when a star passes close enough to a black hole that the tidal force from the black hole overwhelms the self-gravity of the star (e.g. Rees 1988; Evans &

Kochanek 1989). The star is ripped apart and the stellar debris is accreted by the black hole, producing a flare similar in brightness to supernovae that encodes properties of the star and black hole in its light curve and spectra (e.g. Evans & Kochanek 1989; Lodato et al. 2009; Mockler et al. 2019a; Yang et al. 2017; Law-Smith et al. 2017a; Mockler et al. 2022). Theoretical tidal disruption event rates have most often been calculated using the dynamics of two-body relaxation. In this picture, a star will experience random kicks to its angular momentum through interactions with other stars, and if it is very unlucky, one of these kicks will send it radially towards the black hole, where it will be tidally disrupted (e.g. Stone & Metzger 2016). However, in a SMBH binary, 3-body interactions can produce TDEs much faster than two-body relaxation processes (e.g. Ivanov et al. 2005; Chen et al. 2011; Wegg & Nate Bode 2011; Li et al. 2015).

In this paper we study how hierarchical 3-body interactions between the SMBH binary and stars orbiting the smaller black hole can excite the eccentricities of the stars and increase the rates of tidal disruption events. In particular, we focus on the effect of the secular orbital perturbations known as the eccentric Kozai-Lidov (EKL) mechanism (Kozai 1962; Lidov 1962; Naoz 2016). The eccentric Kozai-Lidov mechanism differs from the Kozai-Lidov mechanism in that it includes the octupole order terms in the expansion of the secular, hierarchical three-body equations (see Naoz 2016, for a review). Physically, this allows the z-component of the angular momentum to change with time (the quadrupole Kozai-Lidov solution requires it to remain a conserved quantity), which can lead to higher eccentricities, orbit-flipping, and chaotic behavior. It is known that SMBH binaries and the EKL mechanism can lead to increased rates of TDEs. However,

most previous work on this subject has either focused on the stars surrounding the larger SMBH (e.g. Ivanov et al. 2005; Chen et al. 2011; Wegg & Nate Bode 2011), or an extreme mass ratio inspiral (EMRI) transients instead of TDEs (e.g. Naoz et al. 2022; Mazzolari et al. 2022). Past work has also shown that other dynamical mechanisms suppress EKL oscillations for stars around the larger black hole, and the majority of TDEs that are produced around the larger black hole come from chaotic orbital crossings (Chen et al. 2011). This is generally not the case for the stars around the smaller black hole, largely because the EKL perturbations due to the more massive black hole produce stronger excitations in the stars' orbital eccentricities. Here we expand on work by Li et al. (2015) and explore the effect of the EKL mechanism on the rates of TDEs around the smaller black holes in SMBH binaries.

5.2 Method

5.2.1 Physical processes

We consider a SMBH binary $m_1 < m_2$, separated by a semi-major axis $a_{\rm bin}$, and with an eccentricity $e_{\rm bin}$. Throughout the paper, the subscripts '1', '2', and '*', denote the inner black hole, the outer black hole, and the star respectively. The subscript 'bin' refers to the black hole binary. Surrounding each SMBH is a nuclear star cluster, and for the purposes of this paper we will focus on the stars surrounding m_1. Because $m_1 < m_2$, we can think of the nuclear star cluster of m_1 as embedded in the larger cluster around m_2. The smaller SMBH m_1 will retain stars within its Roche lobe. Each star in the cluster around m_1 can be modeled as part of a hierarchical three-body system

made up of an inner binary pair – m_* and m_1 – and an outer binary pair – m_1 and m_2. The stars surrounding m_1 follow approximately Keplerian orbits, but over time their orbits can be secularly perturbed by m_2 through the eccentric Kozai-Lidov (EKL) mechanism (e.g. Naoz 2016).

The EKL mechanism describes the coherent perturbations from m_2 on the stars orbiting m_1. These perturbations exchange angular momentum between the outer SMBH binary (m_1 and m_2) and the inner binaries made up of stars orbiting m_1. This produces excitations in the eccentricity and inclination of the stars orbiting m_1, and the eccentricity excitations can lead to the production of a large number of tidal disruption events (e.g. Li et al. 2015). To model these systems and determine the rate of tidal disruption events, we solve the solve the secular, hierarchical three-body equations following Naoz et al. (2013), including up to the octupole order terms ($\mathcal{O}(a_*/a_{\rm bin})^3$). The EKL mechanism is limited by the constraint that the system maintain a hierarchical configuration such that,

$$\epsilon = \frac{a_*}{a_{\rm bin}} \frac{e_{\rm bin}}{1-e_{\rm bin}^2} < 0.1 \tag{5.1}$$

There are other dynamical mechanisms that can alter the orbit of the star, and these can enhance or suppress EKL excitations. We are interested in regions of parameter space where the quadrupole Kozai-Lidov timescale is shortest, as these are the regions where the EKL mechanism dominates. The timescale for Kozai-Lidov perturbations, as described by Antonini et al. (2015), is:

$$t_{\rm KL} = \frac{16}{15} \frac{a_{\rm bin}^3 (1-e_{\rm bin}^2)^{3/2} \sqrt{(m_1+m_*)}}{\sqrt{G} a_*^{3/2} m_2} \tag{5.2}$$

The other dynamical processes competing for the largest effect on the stellar orbital parameters are general relativistic precession due to the potential of the disrupting black hole,

$$t_{\rm GR1} = \frac{2\pi a_*^{5/2} c^2 (1-e_*^2)}{3G^{3/2}(m_1+m_*)^{3/2}} \tag{5.3}$$

and Newtonian precession due to the potential of the stellar cusp,

$$t_{\rm NT} = 2\pi \left(\frac{\sqrt{Gm_1/a_*^3}}{\pi m_1 e_*} \int_0^\pi {\rm d}\psi \, M_*(r) \cos\psi \right)^{-1} \tag{5.4}$$

Here ψ is the true anomaly of the inner orbit, $r(\psi) = a_*(1-e_*^2)/(1+e_* cos\psi)$ from Kepler's equation. The function $M_*(r)$ is the integrated stellar mass within $r(\psi)$ – we will discuss the density profiles used to calculate this in Section 5.2.2. If precession due to GR or the stellar potential is strong enough, it can prevent EKL perturbations from building up coherently and exciting the eccentricity and inclination of the star. This has been previously explored by Li et al. (2015), and also by Chen et al. (2011). The timescales $t_{\rm GR1}$ and $t_{\rm NT}$ can be important at small radii, however t_{KL} increases with radius from m_1 as stars move closer to the perturbing black hole (m_2). Therefore it is more difficult for the EKL mechanism to excite the eccentricities of stars at smaller semi-major axes, but at larger radii, where there are many more stars, the EKL mechanism often dominates and can produce many TDEs. For this work we chose to isolate the effects of the EKL mechanism and focused on systems where the EKL timescale $t_{\rm KL}$ is shorter than $t_{\rm GR1}$ and $t_{\rm NT}$ for the majority of stars surrounding the smaller black hole.

We do include GR precession in our modeling, and while it is possible that it

suppresses the number of disruptions at small radii close to m_1, we find that the EKL mechanism acts much faster than GR precession for the majority of the stars around m_1 in the systems we are modeling, as expected. We do not include NT precession in our models, however Li et al. (2015) include it in their calculations for similar systems, and we find that our results are consistent with theirs (see Section 5.3). This is not surprising given that we chose our setups such that the timescale for NT precession is longer than the timescale for EKL excitations for the majority of the stars.

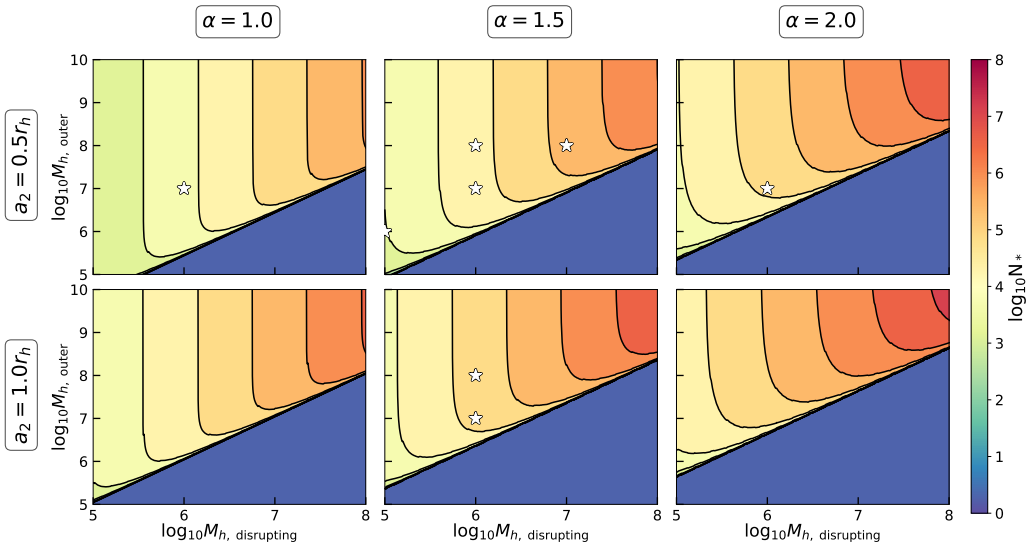

Figure 5.1: Analytical exploration of the parameter space showing the number of stars susceptible to the EKL mechanism. This was calculated by determining the range of semi-major axes for each parameter combination where the EKL timescale is the shortest dynamical timescale. All of our systems have $e_{\mathrm{bin}} = 0.5$. While we compared with a variety of different dynamical timescales[7], the two competing timescales were $t_{\mathrm{GR},\,1}$ and t_{NT}, the timescale for GR precession due to the disrupting black hole and Newtonian precession due to the stellar potential respectively.

5.2.2 Model description

To determine the most useful parts of parameter space to model, we first calculated the relative number of stars we expected to be strongly affected by the EKL mechanism for a variety of parameter combinations. This exploration of parameter space is shown in Figure 5.1, where we have plotted contours based on the number of stars whose shortest dynamical timescale is $t_{\rm KL}$ for each parameter combination.

Figure 5.1 clearly shows why we focus on the smaller black hole in our simulations. As the mass of the disrupting black hole increases with respect to its companion, the number of stars whose shortest dynamical timescale is $t_{\rm KL}$ decreases dramatically. This is because the EKL mechanism is much more effective when the perturbing black hole is larger than the disrupting black hole. When the perturbing black hole is smaller, $t_{\rm KL}$ grows longer than the timescale for Newtonian orbital precession due to the cusp of stars surrounding the black hole, and is also often longer than the timescale for GR orbital precession due to the disrupting black hole. As discussed in the previous section, orbital precession due to these mechanisms can interfere with the coherent excitation of the eccentricity induced by the EKL mechanism (e.g. Chen et al. 2011).

Using Figure 5.1 as our guide, we chose a variety of parameter combinations for our simulations that we expected to produce observable tidal disruption events. The parameters we varied are: the mass of the disrupting and perturbing black holes (m_1 and m_2), their mass ratio ($q = m_2/m_1$), and the power law constant of the density profile for the stellar cusp (α). The mass of m_1 was set to a range of reasonable values for tidal disruption events: $10^5, 10^6$, and 10^7 solar masses. Black holes above $\sim 10^8 M_\odot$

will swallow most stars whole, and disrupt them within their event horizons. Black holes below $10^5 M_\odot$ can and do disrupt stars, however almost all confirmed observed TDEs have occurred around black holes above $10^5 M_\odot$, and therefore we focus on these masses for the purposes of this paper. We use mass ratios $q = m_2/m_1$ of 10 & 100, and this determines the mass of m_2.

To explore the effect of the shape of the stellar cusp on tidal disruption rates, we use a spherical density distribution and vary the steepness of the slope. We use the density distribution described in O'Leary et al. (2009) and used in Li et al. (2015):

$$\rho_*(r) = \frac{3-\alpha}{2\pi}\frac{m_0}{r^3}\left(\frac{GM_0(m_0/M_0)^{1-2/k}}{\sigma_0^2 r}\right)^{-3+\alpha} \tag{5.5}$$

The density profile is written as a power law of semi-major axis, with the integrated stellar mass normalization fixed by the $M-\sigma$ relation. The constants $M_0 = 1.3\times10^8 M_\odot$, $\sigma_0 = 200\mathrm{kms}^{-1}$, and $k = 4$ are the best-fit values for the $M-\sigma$ relation in **?** ($M_h/M_\odot = M_0(\sigma/\sigma_0)^k$). We vary the power law exponent 'α' between 1-2 to explore how the steepness of the stellar cusp affects TDE rates.

We set the eccentricity of the black hole binary to an intermediate eccentricity of $e_{\rm bin} = 0.5$ and its semi-major axis to half of the sphere of influence of the disrupting black hole ($a_{\rm bin} = 0.5 r_{h,\,1}$). This puts the SMBHs at separations of $\sim$ 1pc ($a_{\rm bin} = 0.2 - 1.9$pc for $m_1 = 10^5 - 10^7 M_\odot$) – a regime where the EKL mechanism is highly effective, however the SMBH binary's hardening timescale is still long enough that we do not have to worry about the binary's orbit changing significantly over the course of our simulations. At these radii, the SMBH binary's hardening timescale is mainly

dependent on the effectiveness of loss-cone diffusion, which is likely $\gtrsim 100$ million years (e.g. Kelley et al. 2017), much longer than the EKL timescales for the majority of the stars in our simulation setups.

For each set of parameter combinations, we ran 1000 numerical simulations of the 3-body interactions with different initial conditions for the star. The priors for the star's initial conditions were determined as follows: The semi-major axis of the star was drawn randomly from the density distribution, with a maximum radius determined by the hierarchical condition of the system (see Equation 5.1). The star's eccentricity was drawn from an isothermal distribution, and the mutual inclination was drawn from an isotropic distribution (uniform in $\cos(i)$). The argument of periapsis and the longitude of the ascending nodes were drawn from a uniform distribution between $0 - 2\pi$.

The simulations were run until either the star was disrupted or the system was evolved for 10^9 years (by which point the TDE rate from the EKL mechanism had long since dropped off, see Figure 5.4). Our disruption criteria was that the star passed within $2R_t$ of the black hole (impact parameter $= \beta = 0.5$). This ensured that we captured partial disruptions as well as full disruptions, and we discuss trends with the impact parameter in Section 5.4.

Table 5.1: Simulation parameters and results

run #	m_1 ($\log_{10}M_\odot$)	m_3 ($\log_{10}M_\odot$)	α	a_1 max (au)	N_*	TDE fraction	N_{TDE}
0	5.0	6.0	1.50	6002	5134	0.20 - 0.44	1011 - 2280
1	6.0	7.0	1.00	18980	14081	0.16 - 0.46	2235 - 6445
2	6.0	7.0	1.50	18980	51307	0.17 - 0.42	8979 - 21446
3	6.0	7.0	1.75	18980	97664	0.17 - 0.38	16701 - 37308
4	6.0	7.0	2.00	18980	182705	0.15 - 0.33	27588 - 60841
5	6.0	8.0	1.50	18980	51366	0.03 - 0.45	1541 - 23166
6	6.0	8.0	1.75	18980	97949	0.03 - 0.42	3232 - 41334
7	7.0	8.0	1.50	60021	512509	0.13 - 0.36	67651 - 186041

5.3 Results

5.3.1 Monte Carlo sampling

Each set of 1000 dynamical simulations provides a random Monte Carlo sampling of the stars around the smaller black hole in the each binary system, given the priors described at the end of the last section. We plot the final eccentricity distributions of a subset of our runs in Figure 5.2, where the runs that end in disruption are clearly visible as a buildup of points at high eccentricities (low values of $1 - e$). Our simulations give us the fraction of stars that result in TDEs for each parameter combination, as well as the time of disruption for each random sample. We can then scale our results by the expected total number of stars around m_1 within the hierarchical radius (using Equation 5.5) to compare to real galaxies. The simulation parameters and the fraction and number of stars that become TDEs are quoted in Table 5.1 for each of our runs. We can also calculate a TDE rate as a function of time by binning our simulation results as a function of the time of disruption. We plot our time-dependent rates for a

subset of the runs in Figure 5.4 (using gaussian processes to smooth the distributions).

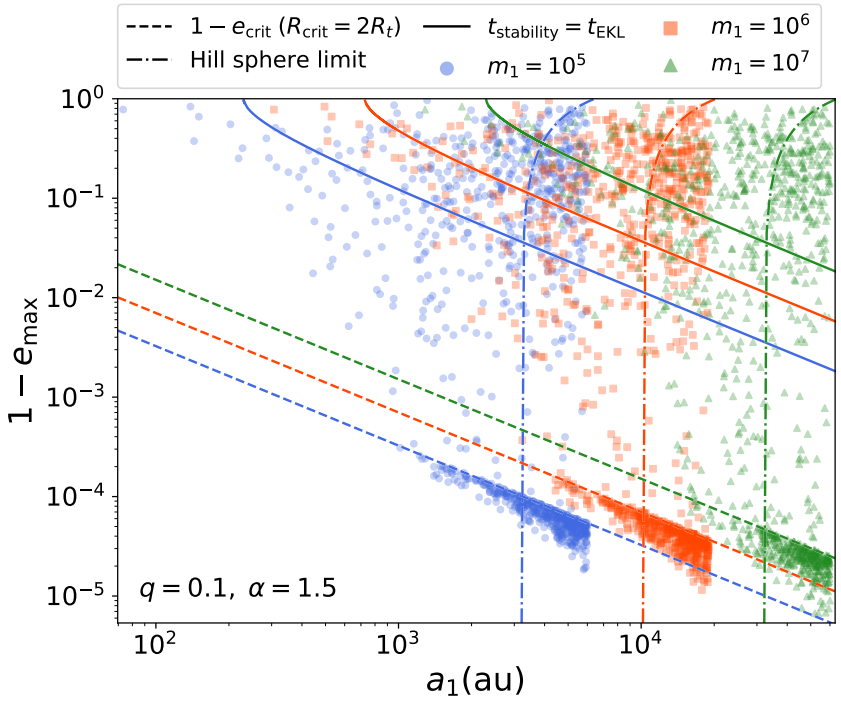

Figure 5.2: The final distributions of the stars' semi-major axes (a_1) and maximum eccentricities ($e_{\rm max}$, plotted as $1 - e_{\rm max}$) for 3 runs with varying inner black hole mass ($m_1 = 10^5, 10^6, 10^7 M_\odot$). The critical radius for disruption used here is $R_p \leq 2R_t$ (allowing for both partial and full disruptions), and denoted by dashed lines in the plot. The Hill radius is denoted by a dash-dotted line. The limiting condition $t_{\rm E} = t_{\rm KL}$ is plotted as a solid line. Orbits that originate outside the Hill radius and have $t_{\rm E} < t_{\rm KL}$ might become unstable before the EKL mechanism can increase their eccentricities and disrupt the stars. These are orbits above the solid line and to the right and below the dash-dotted line. The maximum semi-major axis included for stars in a given run is defined by the hierarchical condition (Equation 5.1).

5.3.2 TDE rates

For each run, we calculate an upper and lower limit for the TDE fraction. The upper limit comes from assuming that all stars on disrupting orbits do, in fact, become TDEs. The lower limit is determined by estimating the fraction of stars that might be scattered onto chaotic orbits on shorter timescales than the EKL timescale, and

excluding these stars when calculating the fraction that become TDEs. We determine which stars to exclude by calculating the timescale that it will take for a star's orbital energy to change by an order of itself ($t_{\rm E}$), and checking if it is smaller than the star's EKL timescale (Zhang et al. 2022):

$$t_{\rm E} = \begin{cases} \frac{1}{4}\left(\frac{m_1}{m_2}\right)^2\left(1+\frac{m_2}{m_1}\right)\left(\frac{a_{\rm bin}}{a_*}\right)\frac{1-e_*}{1+e_*}P_*; & P_*(1-e_*) \sim P_{\rm bin} \\ \\ \frac{1}{16\pi^2}\left(\frac{m_1}{m_2}\right)^2\left(\frac{a_{\rm bin}}{a_*}\right)^4\frac{1}{1-e_*^2}P_*; & P_*(1-e_*) < P_{\rm bin} \end{cases} \tag{5.6}$$

These excluded stars can still become TDEs (as scattered stars can return and be disrupted), however our rates calculated without stars with $t_{\rm E} < t_{\rm KL}$ provide robust lower limits.

We find that for the majority of our simulations, $\sim 13-46\%$ of stars within the maximum radius defined by the hierarchical condition (Equation 5.1) are disrupted. However, increasing the mass ratio increases the number of stars susceptible to scattering by the perturber, and so the lower limit on percentage of stars disrupted in the $q = 100$ runs drops to 3%. As discussed in Section 5.2, the reason we focus on disruptions around the smaller black hole in the SMBH binary is because the stars surrounding the smaller black hole are much more susceptible to eccentricity excitations due to the EKL mechanism. We can compare our results with simulations of the Kozai-Lidov mechanism around the larger black hole in Chen et al. (2011). They find that without including disruptions due to chaotic orbital crossings, the fraction of stars disrupted as a function of radius is always $\lesssim 0.2$, and is approximately 0 at most radii.

5.3.3 Dependence on stellar density profile

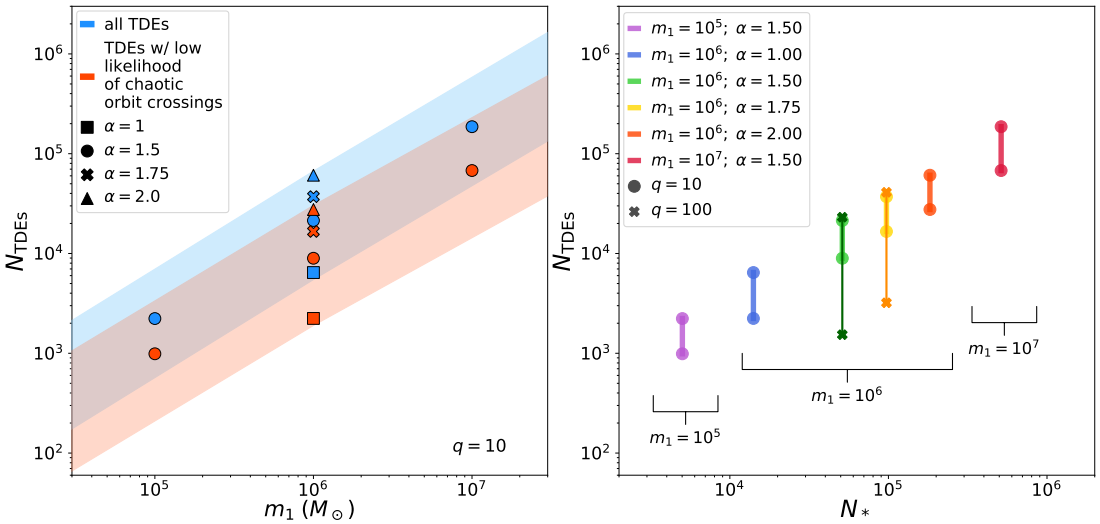

Figure 5.3: **LHS:** The number of TDEs as a function of m_1, with different density profiles represented as different marker shapes. The shaded region is plotted by determining the slopes between the fraction of TDEs for $\alpha = 1.5$ runs at different black hole masses, and then using these slopes and the values for the fraction of TDEs at $m_1 = 10^6 M_\odot$ for $\alpha = 1.0, 1.75, 2.0$ to (linearly) extrapolate estimates for the fraction of TDEs at higher and lower masses for $\alpha = 1.0, 1.75, 2.0$. The points in orange are the lower limits, excluding all stars with $t_{\rm E} < t_{\rm KL}$, while the points in blue are the upper limits and include these stars. **RHS:** The number of TDEs as a function of the number of stars within the hierarchical radius. Each m_1 and α combination is plotted as a different color, and the marker shape is determined by the mass ratio q. The upper and lower limits are determined in the same way as for the LHS.

The rate of tidal disruption events from the EKL mechanism is heavily dependent on the density profile of the stellar cusp. In our simulations, this is due to the fact that the number of stars in the radius range that is most strongly affected by the EKL mechanism changes with the density profile of the cusp. However, changing the density profile of the cusp also changes the background stellar potential each individual star experiences, which can also affect the EKL mechanism. As the steepness of the cusp increases, the timescale for orbital precession due to the stellar potential decreases, and

therefore the EKL mechanism must be stronger to overcome this effect. This is why the EKL mechanism is ineffective at producing TDEs around the larger black hole in the simulations run in Chen et al. (2011) (the majority of TDEs in those simulations come from chaotic orbital crossings). We are interested in studying the regimes in which the EKL mechanism is effective at exciting stellar eccentricities, and therefore we choose values of α, m_1 and m_2 such that the timescale for eccentricity excitation due to the EKL mechanism is shorter than the orbital precession timescale due to the stellar cusp for the majority of the stars in our simulations (see Figure 5.1). We do not model the effect of precession from the stellar potential on our simulations, however we compare our results with Li et al. (2015), who do include this effect, and find that for runs with similar parameters we get a similar fraction of TDEs[8]. The number of tidal disruptions in our simulations remains closely correlated to the number of stars within the hierarchical radius, and increases approximately linearly with the number of stars in this region (as shown in Figure 5.3).

5.3.4 Dependence on black hole mass ratio

Increasing the mass ratio (and therefore the mass of the perturbing black hole, m_2) increases the strength of the perturbations and therefore the range of radii that are sensitive to the EKL mechanism. However, as the majority of stars at large radii (close to our hierarchical radius limit) are disrupted with mass ratios of 10 (see Figure 5.5),

[8](Li et al. 2015) only look at stars within the Hill's radius (even though we expect many stars outside the Hill's radius to be disrupted before they are scattered). In their simulation, $m_1 = 10^7 M_\odot$, $m_2 = 10^8 M_\odot$, $\alpha = 1.75$, $e_2 = 0.5$ and $a_2 = 0.5$pc, and they find 5.7% of stars within the Hill's radius are disrupted. In our simulation with $m_1 = 10^7 M_\odot$, $m_2 = 10^8 M_\odot$, $\alpha = 1.5$, $e_2 = 0.5$ and $a_2 = 0.5 r_h = 1.9$pc, we find that 5.2% of stars within the Hill's radius are disrupted.

increasing the mass ratio in our simulations to 100 does not significantly change the total fraction of stars that are susceptible to the EKL mechanism, even though it does increase this fraction at smaller radii (see Figure 5.5). As there are much fewer stars at small radii ($M_{*,\mathrm{contained}} \propto r^{3-\alpha}$), increasing the mass ratio to 100 only increases the upper limit on the total fraction of disrupted stars in our simulations by a few percent (see Table 5.1). However, increasing the mass ratio does significantly increase the percentage of stars that are susceptible to scattering by the larger black hole, and therefore reduces the lower limit on the number of disrupted stars by a factor of ~ 4. Another noticeable change is to the timescales of the disruptions that do occur. As shown in Figure 5.4, increasing the mass ratio from 10 to 100 increases the TDE rate by a factor of ~ 10 for the first $\sim 10\%$ of the TDE burst (a few $\times 10^5$ years for $m_1 = 10^6 M_\odot$).

In summary, while changing the mass of both black holes and the steepness of the stellar cusp (the value of the density profile exponent 'α') affects the fraction of stars disrupted, it does not change the maximum TDE fraction by more than ~ 0.1, and therefore the strongest determinant of the relative number of TDEs in the system is simply the number of stars within the maximum radius determined by the hierarchical condition (Equation 5.1)[9].

[9]We note that if we did not choose simulation parameters such that $t_{KL} < t_{NT}$ and $t_{KL} < t_{GR1}$ for the majority of stars, the steepness of the stellar cusp and the mass of the black holes might have a more noticeable affect on the TDE rate.

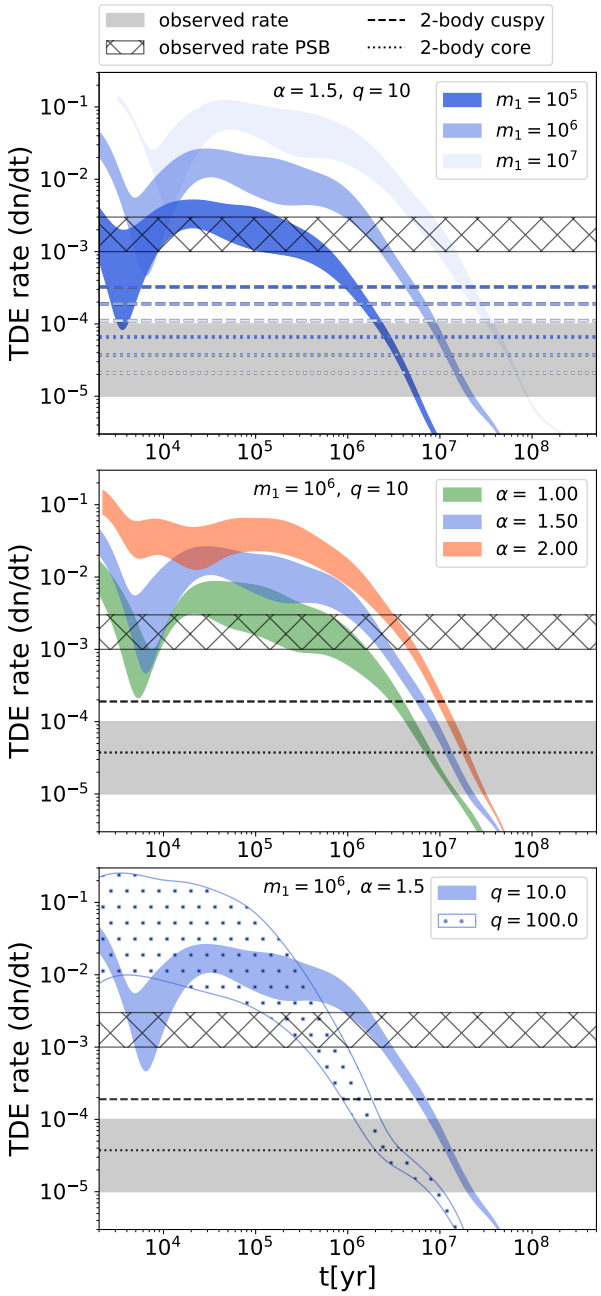

Figure 5.4: TDE rates calculated for the EKL mechanism compared to rates calculated for 2-body relaxation and to observed rates. The 2-body relaxation rates plotted for 'cuspy' galaxies (dashed lines) correspond to galaxies with an inner density profile ($\rho \propto r^{-\gamma}$) $\gamma > 0.5$, while the rates plotted for 'core' galaxies (dotted lines) correspond to $\gamma < 0.3$ (Stone & Metzger 2016, note that density profiles are estimated observationally from radii $> r_h$, and therefore are not a direct comparison to the density profiles used in simulations in this paper for radii interior to r_h.). The observed rate for all TDEs (shaded in gray) is from van Velzen et al. (2020), and the observed rate in post-starburst galaxies (hatched region) is from French et al. (2020).

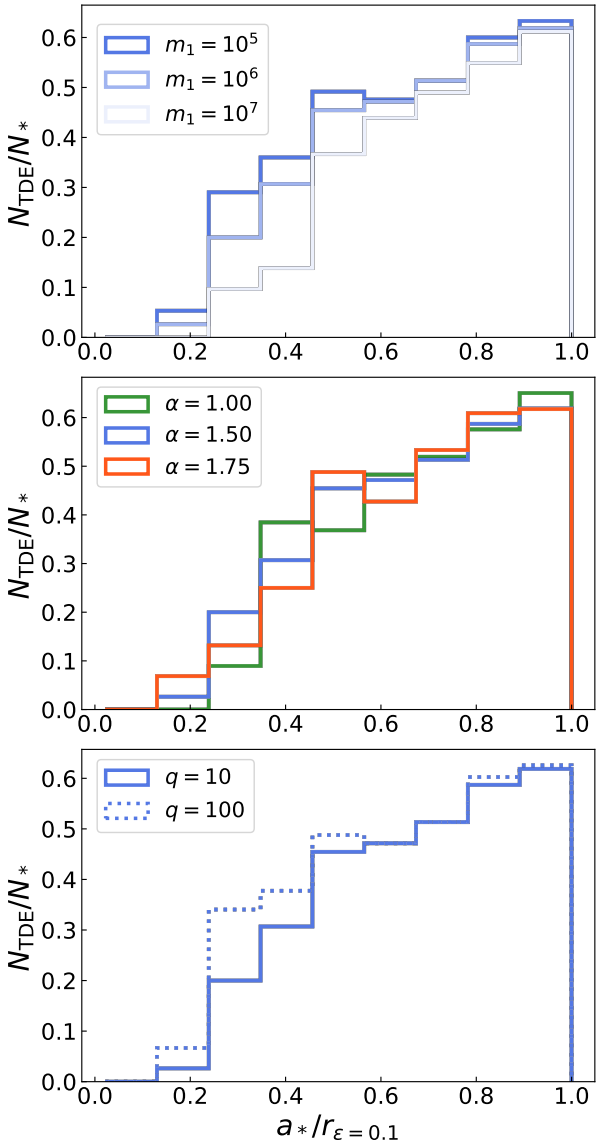

Figure 5.5: The fraction of stars that are disrupted as TDEs as a function of radius. **Top:** $\alpha = 1.5$, $q = 10$. **Middle:** $m_1 = 10^6 M_\odot$, $q = 10$. **Bottom:** $m_1 = 10^6 M_\odot$, $\alpha = 1.5$.

5.4 Discussion

We find that the EKL mechanism in SMBH binaries produces a burst of tidal disruption events at rates much higher than those expected from two-body relaxation (see Figure 5.4). This phenomenon has been previously explored for tidal disruption events, but the majority of past work has focused on the disruptions of stars orbiting the more massive black hole in the binary system (e.g. Ivanov et al. 2005; Chen et al. 2009, 2011; Wegg & Nate Bode 2011). This meant that the majority of disruptions did not actually come from Kozai-Lidov oscillations, but rather from chaotic orbital crossings between the stars and the perturbing black hole (Chen et al. 2011; Wegg & Nate Bode 2011). As we are interested in determining when Kozai-Lidov oscillations in particular are important, we follow Li et al. (2015)'s lead and explore a parameter space centered on the smaller black hole.

5.4.1 Comparison with simulated and observed TDE rates

In Figure 5.4 we compare the rate calculated from our simulations with the rates estimated for two-body relaxation based on properties of observed galaxies (dashed lines, from Stone & Metzger 2016). We find that the rate from the EKL mechanism is higher than the rate from two-body relaxation for timescales between millions to tens of millions of years depending on the parameters of the system. This means that the EKL rate is also much higher than the overall observed rate (as two-body relaxation calculations generally over-predict the observed rate). This is not surprising, as the scenario described in this paper is only applicable to a small subset of galaxies, and

only over a relatively short time period.

Only a fraction of galaxies will have experienced recent mergers and host SMBH binaries at any given time. The merger fraction at low redshift ($z \lesssim 0.7$) for massive galaxies ($M_* \geq 10^{11} M_\odot$) is thought to be $\lesssim 10\%$, with major mergers making up $\sim 2-5\%$ of the total and minor mergers making up $\sim 5\%$ (Bundy et al. 2009; López-Sanjuan et al. 2012). The fraction does appear to decrease with galaxy mass, so that Bundy et al. (2009) find a major merger fraction of $\sim 3\%$ for galaxies between $10^{10} - 10^{11} M_\odot$, and $\sim 5\%$ for galaxies $\geq 10^{11} M_\odot$. Given these results, it seems reasonable to assume a merger fraction of a few percent for minor mergers at galaxy masses below $10^{11} M_\odot$, the relevant mass ratio and galaxy mass range for the simulations in this paper. Some observational studies have also found that the major merger fraction increases with redshift (Bluck et al. 2009, 2012) up to $\sim 25-40\%$ at $z = 3$ ($\sim 10^{10}$ year lookback time), and the Illustris simulation finds a similar trend for both the major and minor merger rates (Rodriguez-Gomez et al. 2015). If this is the case, the current-day SMBH binary population might reflect a higher merger fraction at earlier times, depending on the hardening timescale of the binary.

In addition to there only being a small subset of galaxies with SMBH binaries, there are other reasons the elevated TDE rate from the EKL mechanism could be difficult to observe. If the stars are not replenished rapidly through star formation or dynamical mechanisms, the rate will drop off relatively quickly and the elevated rate will only be observable for at most tens of millions of years (see Figure 5.4). Therefore, it is possible that even in galaxies that have recently merged, we will miss the 'burst' of

TDEs predicted here. Finally, in this paper we focus on the effect of the eccentric Kozai-Lidov oscillations, however it is possible that sub-dominant dynamical mechanisms could change the shape of the rate curves. For example, Melchor et al. (2022) finds that including the effect of two-body relaxation on the EKL mechanism can stretch the rate curves, so that disruptions continue to later times, but the maximum rate is lower. While this does not significantly change the overall number of TDEs from the EKL mechanism, it can decrease the instantaneous rate. These restrictions mean it is unsurprising that we do not observe dramatically higher TDE rates due to the EKL mechanism, we still expect this mechanism to contribute meaningfully to the rates, particularly for larger mass black holes, as the two-body relaxation rate drops off with black hole mass but the rate from the EKL mechanism increases with black hole mass.

Interestingly, the rate we calculate during the EKL burst is much more comparable to the observed rates calculated for post-starburst galaxies, which are often considered candidates for recent mergers (Mihos & Hernquist 1994; Bekki et al. 2005; Hopkins & Hernquist 2009, as mergers can trigger starbursts). The reason why the TDE rate in post-starburst galaxies is $\sim 20 - 200\times$ higher than the galaxy averaged rate is not well understood, and it remains an open question in the field (Arcavi et al. 2014; Law-Smith et al. 2017a; French et al. 2020). Previous work has suggested that SMBH binaries might be able to increase the rates of TDEs in these galaxies if the starburst is due to a recent merger (e.g. Arcavi et al. 2014). However, as Stone et al. (2018) point out, if the starburst is triggered by a merger, and the increased rates are from the resulting SMBH binary, this requires the smaller black hole to sink to the

center of the galaxy on timescales short enough that the post-starburst features are still observable. If the starburst is triggered when the merger stars, this may be difficult, as the timescales for most SMBH binaries to harden to distances of $\sim$ 1pc are thought to be of order 10^9 years (Kelley et al. 2017). That being said, the 'hardening timescale' is very dependent on model assumptions, such as the amount of gas surrounding the binary, and also how quickly stars can refill the region of parameter space with low enough angular momentum to interact with the black hole binary (often called the 'loss cone', not to be confused with the TDE loss cone) (e.g. Khan et al. 2011; Kelley et al. 2017; Vasiliev & Merritt 2013) This second uncertainty in particular can dramatically change the result – refilling the parameter space of stars that interact strongly with the SMBH binary can decrease the average hardening timescale by approximately an order of magnitude (Kelley et al. 2017). If this parameter space is able to be refilled in at least some mergers, than it is possible that post-starburst features would still be observable when the SMBH binary is at separations of $\sim$ 1pc and the EKL mechanism becomes important. Alternatively, if a starburst is triggered later in the merger process, a long hardening timescale might not be an issue.

5.4.2 Finding hidden SMBH binaries

Despite their rarity, bursts of TDEs produced by the EKL mechanism could help us find hidden SMBH binaries. Tidal features from minor mergers dissipate quickly (Conselice et al. 2000), and the potential of a galactic nucleus hosting a SMBH binary with a mass ratio $\lesssim 10$ will be dominated by the mass of the larger black hole, making it difficult to find SMBH binary candidates. However, as shown here, disruptions produced

by the EKL mechanism will produce a significant number of TDEs around the smaller black hole in a SMBH binary, comparable in number to TDEs around the larger black hole for mass ratios of $q = 10$. Tidal disruption flares contain information about the mass of the disrupting black hole, therefore TDEs from the smaller black hole can expose its presence. For example, the light curve timescale of a TDE is dependent on the mass of the black hole (e.g. $t \propto M_h^{1/2}$, Mockler et al. 2019a), therefore if a very short flare occurred around what seemed to be a much larger black hole, that would be an indication of a potential SMBH binary. If the mass of the larger black hole is above $\gtrsim 10^8 M_\odot$, it would not be able to produce and observable flare from the disruptions of most stars, and therefore seeing any TDE at all from very massive galaxies would be a very strong indication of a hidden companion SMBH (e.g. Coughlin & Armitage 2018).

5.4.3 Repeated TDEs

When a star is disrupted, the most commonly used assumption is that part of the star will remain bound to the black hole, and eventually accrete onto it, while the rest of the star will leave the system on an unbound orbit. This is a reasonable assumption for orbits that are nearly parabolic, with eccentricities approaching $e = 1$, as is expected for most TDEs. However, as the eccentricity decreases, the likelihood that the rest of the star becomes unbound decreases. The less bound portion of the star will generally experience a kick (Manukian et al. 2013), however if the eccentricity is low enough this will not be sufficient to unbind it from the SMBH. In the case of a partial disruption, where the star's core remains after material is torn off by the black hole, the star may return to the SMBH and get disrupted multiple times – a 'repeated'

TDE. Recently, the first candidate 'repeated' TDE was observed, the nuclear transient ASASSN-14ko (Payne et al. 2022).

The majority of TDEs that come from two-body relaxation originate near the sphere of influence of the black hole (Stone & Metzger 2016), and require very high eccentricities to pass within their tidal radii and be disrupted. On the other hand, TDEs that come from the EKL mechanism originate from near the hierarchical radius, which can be much smaller than the sphere of influence, as it is dependent on the semi-major axis of the black hole binary (see Equation 5.1). This means that the disrupted stars will have lower eccentricities, and they will be more bound to the SMBH and more likely to produce repeating TDEs.

We find that the EKL mechanism preferentially disrupts stars on the lowest impact parameter orbit possible, which increases the likelihood of repeated events. This is because the increase in maximum eccentricity over multiple EKL oscillations is very small compared to the size of the oscillations. Another way of thinking about this is that the slope of the envelope of the oscillations is small, even though the individual oscillations are quite large. For a true point mass, EKL oscillations are capable of producing eccentricities that approach 1, however as part of this process the point mass will first orbit the SMBH many times at lower eccentricities that are nonetheless high enough to disrupt most stars. Because of this, we expect many stars to get partially disrupted but remain bound to the black hole – producing repeating TDEs that might eventually fully disrupt the star, if the star isn't kicked out of orbit around the SMBH first (see Melchor et al. 2022, for a detailed discussion of repeated TDEs from the EKL

mechanism). In Figure 5.6 we show that the relative number of initial disruptions drops off dramatically as a function of impact parameter. For TDEs from two-body relaxation, the rate as a function of impact parameter is expected to drop off as β^{-1} (for the full loss cone scenario, Stone & Metzger 2016). We find an even quicker drop off in TDE rate as a function of β for TDEs from the EKL mechanism.

5.5 Supplemental Data

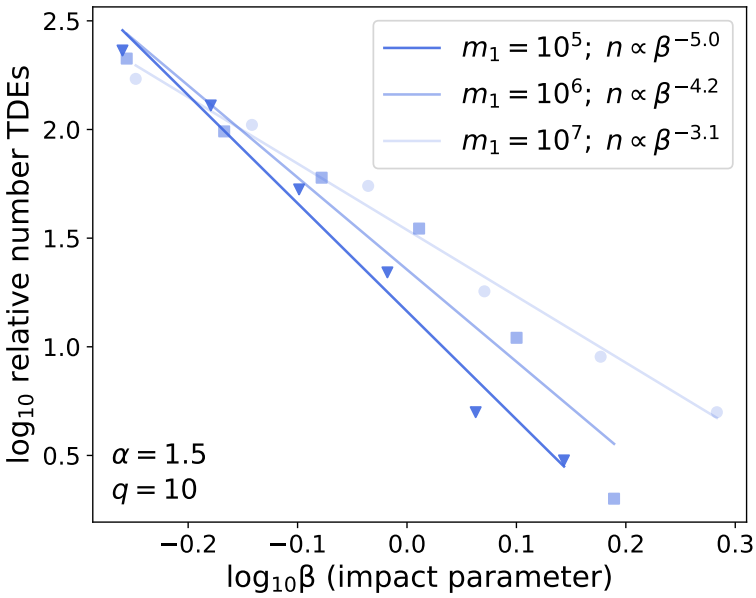

Figure 5.6: Best-fit power laws to the number of TDEs as a function of impact parameter (β). TDEs are binned as a function of β and power laws are fitted to the binned data. The raw binned data is plotted as individual points in the plot. Changing the binning can change the best-fit power law index by $\sim \pm 0.1$. Additional analysis of the β dependence will be presented in later work.

Chapter 6

Summary and Future Directions

6.1 Summary

This thesis explored how tidal disruption events can be used to constrain the properties and evolution of SMBHs and nuclear star clusters. Chapter 2 described a light curve model for tidal disruption events, and used it to fit a population of these transients, determining that properties such as the impact parameter and most notably the black hole mass can be constrained through light curve fitting. The black hole masses measured from the light curve were found to be consistent with measurements from the $M - \sigma$ relation. Chapter 3 used the same model to constrain the emission mechanism in TDEs, showing that even with large uncertainties on the mass-to-energy efficiency, these events are most likely too energetic to be produced by stream-stream collisions, and are more consistent with being produced by accretion processes close to the black hole. This work produced a publicly available, widely used TDE light curve model, and detailed a new method for black hole mass measurement. It also

uncovered trends in the properties of TDE light curves, improving our understanding of the observed population of these transients and helping solve longstanding theoretical debates on the mechanisms powering these transients.

Chapter 4 combined information from the light curve models with data from spectra and the host galaxy to provide constraints on the mass and age of the disrupted stars. Surprisingly, it found that higher metallicity stars (with N/C abundances ≥ 10) are very over-represented in tidal disruption events. These TDEs are consistent with originating from stars with masses $\geq 1.3 M_{\odot}$ – a subset of the stellar population that makes up $\sim 0.05\%$ of stars in the host galaxies but 5% of observed TDEs. This could be due to differences in how star formation operates in the very centers of galaxies compared to the rest of the galaxy, or due to the dynamical processes that are moving stars onto disrupting orbits. Chapter 5 explores how the 3-body dynamics of stars orbiting SMBH binaries can increase the rates of TDEs and possibly uncover hidden binary systems. It finds that for mass ratios of 10, the smaller mass black hole in the system can disrupt a similar amount of stars as the larger black hole, making it a viable method for detecting close SMBH binaries. These chapters examined how TDEs can be used to learn about star formation and dynamics in the centers of galaxies, as well as their connection to the larger picture of galaxy evolution.

6.2 Future directions

The research in this thesis brings to light multiple unresolved questions that have already inspired plans for future projects. Many of these questions are connected

to the radiation transport of TDE emission. For example, it is not clear how closely the observed luminosity traces the mass inflow rate, particularly at early times and near peak luminosity when the mass accretion rate is very high. Deviations from this assumption would affect the measurements of black hole masses, as well as estimates of the time-dependent accretion efficiency. Furthermore, current light curve models are unable to precisely constrain the properties of the star that is disrupted and the efficiency at which the SMBH converts mass into radiation. These parameters are either degenerate (see Chapter 3), or dependent on model assumptions such as the shape and structure of the reprocessing region (Dai et al. 2018). This has fueled ongoing debate about the mass-to-energy conversion efficiency in these events, and the formation timescale and evolution of the accretion disk. Both of these areas of uncertainty are critical for understanding how quickly SMBH can grow when being fed at super-Eddington mass accretion rates. Radiative transfer simulations can constrain the amount of mass in the reprocessing layer, as well as connect the composition of the star to lines in the spectra, providing independent estimates of the mass of the star and therefore also constraining the black hole accretion efficiency.

6.2.1 Radiation transfer simulations of TDEs and wind transients

For 'engine' powered central source transients such as TDEs, the majority of the energy is produced (or liberated) deep within the reprocessing layer. Radiative transfer simulations are thus required to connect theories for energy extraction to observations. The reprocessing of TDE emission is used to explain the smoothness of TDE light curves (Holoien et al. 2019) and their large optical luminosities (e.g., van

Velzen et al. 2020), which set them apart from AGN. However, accurately modeling the reprocessing of the emission is uniquely challenging in a TDE environment.

The strong radiation drives the ionization state out of equilibrium, requiring non-local thermodynamic equilibrium (non-LTE) calculations for modeling line transport. The gas is also optically thick to electron scattering, a regime that photoionization codes like `CLOUDY` cannot accurately model. The high optical depths – due to the very high mass accretion rates – are key to producing the observed continuum and spectra (Roth et al. 2016). Additionally, the order of magnitude changes in mass flow and source luminosity mean that a time-dependent treatment of diffusion is critical for determining the shape of the light curve (Khatami & Kasen 2019). The `Sedona` radiative transfer code (a Monte Carlo radiation transport code) is one of the few codes that can model the conditions in a TDE, and is currently the only one capable of reproducing the appearance of TDE line profiles (see Figure 6.1; Roth et al. 2016; Roth & Kasen 2018). I recently worked on upgrading `Sedona` to run with a state of the art moving mesh hydrodynamics code (Duffell & MacFadyen 2011), so that it can handle the dramatically varying mass flows in these transients. I plan to create two suites of simulations (suites A & B), the first to determine the shape and time evolution of the light curves and the second to model the detailed spectra.

Conditions in TDEs are similar to those in transients with large mass outflows that derive most of their power from a central source, such as changing look AGN, and supernovae powered by fallback accretion, magnetars, or CSM shocks (likely including the enigmatic 'fast blue optical transients', or FBOTS). Therefore, models of the

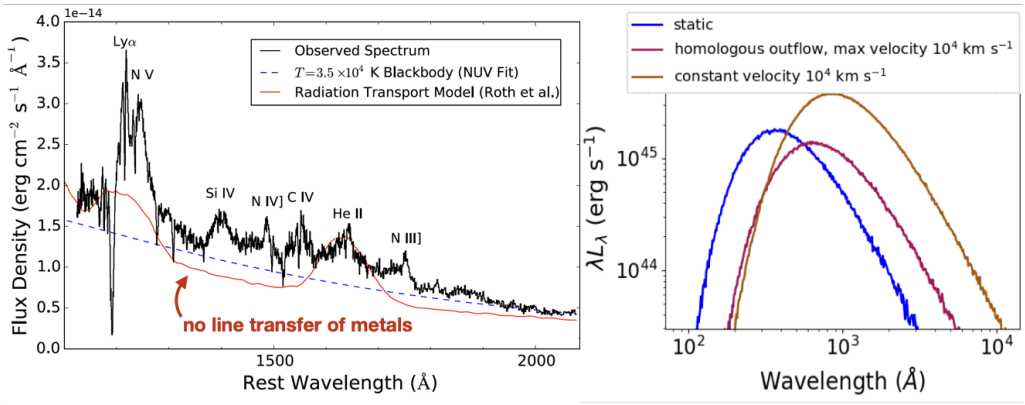

Figure 6.1: **LHS:** `Sedona` model (in red) with UV spectrum of ASASSN-14li (adapted from Cenko et al. 2016). Only line transport of H & He was included. **RHS:** Reprocessing in TDE-like outflow for various velocity profiles (Roth & Kasen 2018).

radiation transport in TDEs can be adapted to study these phenomena as well.

A: What sets the shape of the light curves?

Existing TDE light curve models such as the ones described in Chapter 2 rely on the approximations that the observed luminosity closely follows the rate of return of stellar debris from the disrupted star onto the SMBH and that the emission is a blackbody at a specified radius. Deviations from the first assumption will affect measurements of SMBH masses with TDE light curves, while deviations from the second will affect estimates of the energy released and the black hole accretion efficiency during these transients. Furthermore, current light curve models are unable to independently constrain the properties of the star that is disrupted and the efficiency at which the black hole consumes mass during these events, as these parameters are degenerate (as described in Chapter 3).

To improve these models and their parameter measurement capabilities, I plan to perform the first time-dependent radiation hydrodynamic simulations that model the

entire evolution of the TDE light curve. The few radiative transfer models that exist look at snapshots in time near the peak of the transient's luminosity (Roth et al. 2016; Roth & Kasen 2018; Dai et al. 2018). However, the mass flow to the black hole and the source luminosity change by orders of magnitude throughout the transient's evolution, so *a time-dependent approach is necessary* for determining what sets the shape of the light curve. This is particularly true for the rise of the light curve, when the luminosity timescale is likely small compared to the diffusion timescale.

Additionally, previous simulations of the radiative transfer process for TDEs and other transients have largely relied on homologous velocity profiles. However, Roth & Kasen (2018) showed that for centrally powered sources, the adiabatic reprocessing of luminosity in a constant velocity 'wind' model produced significantly more optical and UV emission compared to a homologous velocity profile (see Figure 6.1). Adiabatic reprocessing is likely to be very important for producing the substantial optical and UV luminosities from the initial source spectrum in TDEs (e.g. Strubbe & Quataert 2009; Piro & Lu 2020), and we speculate that this might also be the case for other transients with fast outflows and centrally concentrated source luminosities. Accurately calculating this effect requires modeling time-dependent electron scattering at high densities to determine how long radiation is 'trapped' within the expanding outflow.

B: Connecting spectra to composition

I also plan to run a set of multi-dimensional non-LTE radiative transfer simulations to determine the dependence of the spectral line features on the conditions of the gas and the composition of the disrupted star. By varying the amount and composition of

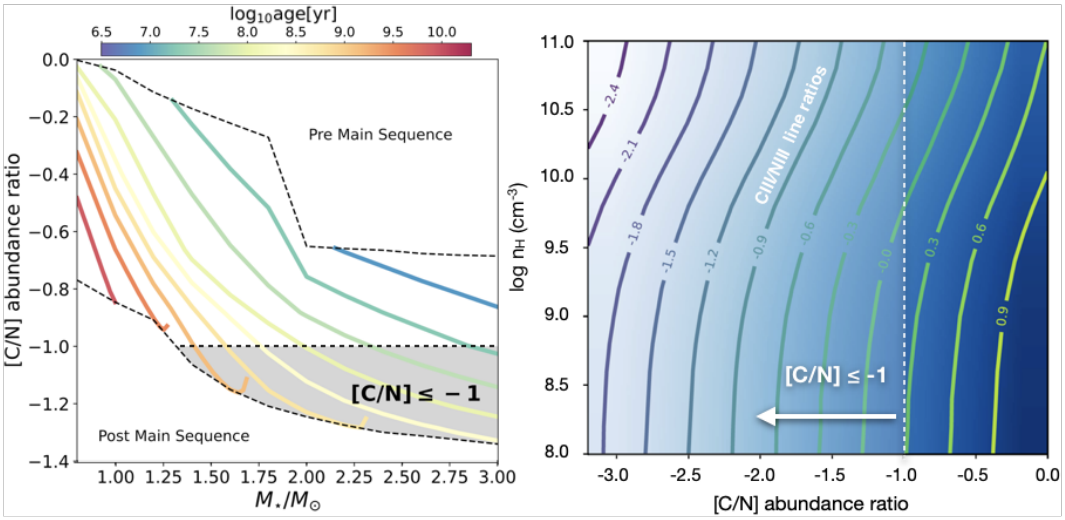

Figure 6.2: Shaded regions show constraints from UV C/N line ratios (C/N≤0.1, N/C≥10). **LHS:** $\log_{10}$[C/N] abundance ratio in the fallback debris as a function of stellar mass, lines of constant age over-plotted (adapted from Chapter 4). **RHS:** The effect of density on the CIII/NIII line ratio as a function of the $\log_{10}$[C/N] abundance ratio (adapted from Yang et al. 2017).

mass in the disk and outflow as well as the source luminosity, we will model different stages in the evolution of the TDE (the light curve rise, peak, and decay). This will help constrain the properties of the disrupted star and determine how the spectra are affected by the geometry and dynamics of the gas around the black hole, building on work done in Chapter 4 of this thesis. This is currently one of few avenues for estimating the individual properties of stars in galactic nuclei outside our own.

Previous work used the UV line ratio of N III/C III to estimate a maximum N/C abundance ratio for several TDEs (Yang et al. 2017). This work assumed that the lines were formed in similar gas conditions, because the UV N III (λ1750) and C III (λ1908) line transitions have similar critical densities and excitation energies, and involve ions with similar ionization energies. Our measurements of UV line ratios rely on space-based spectroscopy from the Hubble Space Telescope (HST), and will

benefit enormously from the development of future space-based missions. There are currently only a handful of TDEs with UV spectra, but if the lower limits on the N/C abundance ratio are accurate, they already point to something interesting. In Chapter 4 I showed that these estimates imply an overabundance of tidal disruptions of stars above $\sim 1 M_{\odot}$ compared to what we would expect from the host galaxies' stellar populations, or our own galactic center. Using `Sedona` we will be able to confirm these results by modeling line transfer through the entire TDE outflow. For example: as the density of the emission region approaches the critical densities (as is possible in the inner regions of TDE outflows), the UV N/C line ratio will start to be strongly affected (by up to $\sim$ 0.6 dex, see Figure 6.2). Yang et al. (2017) were aware of this, and were very conservative when estimating lower limits on abundance ratios because of it. I will model the formation of the lines in the TDE outflow to determine the importance of this effect, improving constraints on the N/C abundance ratio.

I also plan to model the formation of the more easily observable optical nitrogen lines to determine if they can also constrain the composition of the star. This is important as there are only 6 TDEs that have published HST UV spectra, and there are currently $\sim$ 10 TDE candidates with strong N III broad emission lines in their optical spectra that do not have UV spectra. It is unclear whether the optical nitrogen lines indicate enhanced nitrogen abundances, or if the line strength is due to radiation transfer effects. For example, Roth et al. (2016) showed that the high helium-to-hydrogen ratio observed in some TDEs can be explained by optical depth effects, even if the abundance of hydrogen is larger than the abundance of helium. Therefore, accurately modeling the

geometry and velocity profiles of the gas is necessary for connecting observed lines to gas composition.

6.2.2 Improving black hole masses measurements

I plan to incorporate the results of these planned radiative transfer simulations into my `MOSFiT` TDE light curve model, and use it to fit the growing population of TDEs, creating a new dataset of low mass SMBHs ($10^5 M_\odot \lesssim M_h \lesssim 10^8 M_\odot$) with mass measurements.

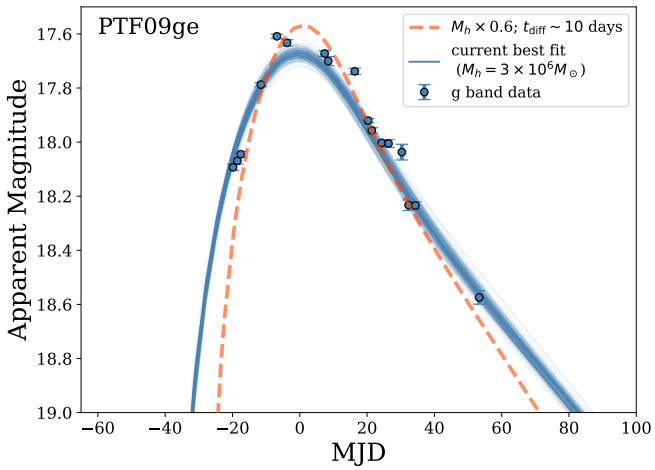

Figure 6.3: Example fit from Chapter 2 plotted in g-band (blue), with estimate of how light curve changes if $M_{\rm h}$ decreases ($M_{\rm h,\,new} = 0.6 \times M_{\rm h,\,original}$) but we include an approximation of a $\sim$ 10 day diffusion timescale (orange). Fit score for original model is higher, however both can approximate light curve shape.

As discussed earlier, theoretical uncertainties in the reprocessing efficiency and diffusion timescale, as well as model degeneracies between the mass of the star and the mass-to-energy efficiency of the transient, produce systematic uncertainties in the parameter extraction from TDE light curve models (see Figure 6.3). Reducing these

uncertainties is particularly important for modeling TDEs around lower mass SMBHs ($\lesssim 10^6 M_\odot$). As the black hole mass decreases, the peak timescales decrease and mass fallback rates increase at the same time the Eddington limit decreases. Therefore, transients around smaller mass black holes will likely have more mass in their outflows at early times, and a shorter source luminosity timescale. Both of these factors will increase the effect the diffusion timescale has on the observed light curve, and the uncertainties it induces in the estimation of the black hole mass.

Similar uncertainties in the reprocessing efficiency and diffusion timescale exist in the models of other transients with wind outflows and/or central sources (Ginzburg & Balberg 2012; Khatami & Kasen 2019). I plan to use the results of my time-dependent radiation hydrodynamic simulations (suite A) to determine how differing velocity profiles and mass fallback rates affect the diffusion and reprocessing of the luminosity in my models and therefore the shape of the light curve in TDEs. By creating 'diffusion' and 'photosphere' `MOSFiT` modules specific to central-source transients and wind outflow reprocessing (as opposed to homologous expansion), and which can be substituted into other existing models, I will also improve the `MOSFiT` models for related transients (e.g. CSM interaction, magnetar-powered, and fallback supernovae).

Additionally, I plan to add fitting (and predictions) of N/C UV line ratios into the `MOSFiT` TDE model. My radiation transfer simulations modeling the line transport of nitrogen and carbon (suite B) will hopefully determine how the N/C UV line ratio measured for a given abundance ratio is affected by the gas density, velocity, and source luminosity (similar to the right panel of Figure 6.2, but varying more parameters). I plan

to use the results to make either semi-analytical fitting functions or interpolation functions for the line ratio as a function of these parameters. To make use of this information, I will update my `MOSFiT` TDE model to run using the library of composition-tracking mass fallback rates calculated in Law-Smith et al. (2020, inc. Mockler) for a wide range of stellar masses and ages. This will make it possible to estimate the nitrogen-to-carbon abundance in the outflowing debris as a function of time and input it into the model's calculation of the observed line ratio. While incorporating full spectral fitting would be too computationally expensive and physically uncertain given the complicated dependencies of most lines on gas conditions, we expect to be able to constrain the N/C UV line ratio because of its simpler dependence on gas conditions.

Measurements of the diffusion timescale and the outflow reprocessing will help break the current model degeneracy between the mass of the star and the mass-to-energy efficiency, allowing better estimates of these parameters from light curves. For events with measured N/C UV line ratios, the improved library of mass fallback rates will provide even better constraints on these parameters, and will also constrain the age of the star. Estimating the properties of the star will also further reduce uncertainties in the measurement of the mass of the SMBH, as large deviations in the mass-radius relation of the star can affect the SMBH mass measurement (see Chapter 2).

Bibliography

Alexander, K. D., Berger, E., Guillochon, J., Zauderer, B. A., & Williams, P. K. G. 2016, ApJ, 819, L25

Allison, R. J., Goodwin, S. P., Parker, R. J., et al. 2009, ApJ, 700, L99

Andalman, Z. L., Liska, M. T. P., Tchekhovskoy, A., Coughlin, E. R., & Stone, N. 2020, arXiv e-prints, arXiv:2008.04922

Andalman, Z. L., Liska, M. T. P., Tchekhovskoy, A., Coughlin, E. R., & Stone, N. 2022, Monthly Notices of the Royal Astronomical Society, 510, 1627, aDS Bibcode: 2022MNRAS.510.1627A

Antonini, F., Barausse, E., & Silk, J. 2015, The Astrophysical Journal, 812, 72

Arcavi, I., Gal-Yam, A., Sullivan, M., et al. 2014, ApJ, 793, 38

Asplund, M., Grevesse, N., Sauval, A. J., & Scott, P. 2009, ARA&A, 47, 481

Auchettl, K., Guillochon, J., & Ramirez-Ruiz, E. 2017, ApJ, 838, 149

Auchettl, K., Ramirez-Ruiz, E., & Guillochon, J. 2018, ApJ, 852, 37

Ayal, S., Livio, M., & Piran, T. 2000, ApJ, 545, 772

Bahcall, J. N., & Wolf, R. A. 1977, ApJ, 216, 883

Barnes, J. E., & Hernquist, L. E. 1991, ApJ, 370, L65

Bate, M. R. 2009, MNRAS, 392, 1363

Batra, N. D., & Baldwin, J. A. 2014, Monthly Notices of the Royal Astronomical Society, 439, 771, aDS Bibcode: 2014MNRAS.439..771B

Baumgardt, H., Makino, J., & Ebisuzaki, T. 2004, ApJ, 613, 1143

Bekki, K., Couch, W. J., Shioya, Y., & Vazdekis, A. 2005, MNRAS, 359, 949

Beloborodov, A. M. 1999, High Energy Processes in Accreting Black Holes, 161, 295

Blagorodnova, N., Gezari, S., Hung, T., et al. 2017, The Astrophysical Journal, 844, 46

Blagorodnova, N., Cenko, S. B., Kulkarni, S. R., et al. 2019, ApJ, 873, 92

Blandford, R. D., & McKee, C. F. 1982, ApJ, 255, 419

Bluck, A. F. L., Conselice, C. J., Bouwens, R. J., et al. 2009, Monthly Notices of the Royal Astronomical Society, 394, L51, aDS Bibcode: 2009MNRAS.394L..51B

Bluck, A. F. L., Conselice, C. J., Buitrago, F., et al. 2012, The Astrophysical Journal, 747, 34, aDS Bibcode: 2012ApJ...747...34B

Bogdanović, T., Eracleous, M., Mahadevan, S., Sigurdsson, S., & Laguna, P. 2004, ApJ, 610, 707

Bonnerot, C., & Lu, W. 2020, MNRAS, 495, 1374

Bonnerot, C., Price, D. J., Lodato, G., & Rossi, E. M. 2016a, ArXiv e-prints, arXiv:1611.09853

Bonnerot, C., Rossi, E. M., Lodato, G., & Price, D. J. 2016b, MNRAS, 455, 2253

Brooks, S. P., & Gelman, A. 1998, Journal of computational and graphical statistics, 7, 434

Brown, J. S., Holoien, T. W.-S., Auchettl, K., et al. 2017, Monthly Notices of the Royal

Astronomical Society, 466, 4904

Brown, J. S., Shappee, B. J., Holoien, T. W.-S., et al. 2016, Monthly Notices of the Royal Astronomical Society, 462, 3993

Brown, J. S., Kochanek, C. S., Holoien, T. W. S., et al. 2018, MNRAS, 473, 1130

Brown, J. S., Kochanek, C. S., Holoien, T. W.-S., et al. 2018, Monthly Notices of the Royal Astronomical Society, 473, 1130

Bundy, K., Fukugita, M., Ellis, R. S., et al. 2009, The Astrophysical Journal, 697, 1369, aDS Bibcode: 2009ApJ...697.1369B

Burrows, D., Kennea, J., Ghisellini, G., et al. 2011, Nature, 476, 421

Cannizzo, J. K., Lee, H. M., & Goodman, J. 1990, ApJ, 351, 38

Cao, R., Liu, F. K., Zhou, Z. Q., Komossa, S., & Ho, L. C. 2018, MNRAS, 480, 2929

Cenko, S. B., Cucchiara, A., Roth, N., et al. 2016, The Astrophysical Journal, 818, L32

Cenko, S. B., Cucchiara, A., Roth, N., et al. 2016, ApJ, 818, L32

Charalampopoulos, P., Leloudas, G., Malesani, D. B., et al. 2021, arXiv e-prints, arXiv:2109.00016

Chen, X., Madau, P., Sesana, A., & Liu, F. K. 2009, ApJ, 697, L149

Chen, X., Sesana, A., Madau, P., & Liu, F. K. 2011, ApJ, 729, 13

Cheng, R. M., & Bogdanović, T. 2014, Phys. Rev. D, 90, 064020

Choi, J., Dotter, A., Conroy, C., et al. 2016, The Astrophysical Journal, 823, 102

Chornock, R., Berger, E., Gezari, S., et al. 2014, ApJ, 780, 44

Conselice, C. J., Bershady, M. A., & Jangren, A. 2000, The Astrophysical Journal, 529, 886, aDS Bibcode: 2000ApJ...529..886C

Coughlin, E. R., & Armitage, P. J. 2017, ArXiv e-prints, arXiv:1705.04689

Coughlin, E. R., & Armitage, P. J. 2018, Monthly Notices of the Royal Astronomical Society, 474, 3857, aDS Bibcode: 2018MNRAS.474.3857C

Coughlin, E. R., & Begelman, M. C. 2014, ApJ, 781, 82

Coughlin, E. R., & Nixon, C. J. 2019, ApJ, 883, L17

Dai, L., Escala, A., & Coppi, P. 2013, ApJ, 775, L9

Dai, L., McKinney, J. C., & Miller, M. C. 2015, ApJ, 812, L39

Dai, L., McKinney, J. C., Roth, N., Ramirez-Ruiz, E., & Miller, M. C. 2018, ApJ, 859, L20

Davis, S. W., Narayan, R., Zhu, Y., et al. 2011, ApJ, 734, 111

De Colle, F., Guillochon, J., Naiman, J., & Ramirez-Ruiz, E. 2012, ApJ, 760, 103

Dib, S., Schmeja, S., & Parker, R. J. 2018, MNRAS, 473, 849

Dodd, S. A., Law-Smith, J. A. P., Auchettl, K., Ramirez-Ruiz, E., & Foley, R. J. 2021, ApJ, 907, L21

Dotter, A. 2016, The Astrophysical Journal Supplement Series, 222, 8

Dressler, A., & Gunn, J. E. 1983, ApJ, 270, 7

Duffell, P. C., & MacFadyen, A. I. 2011, ApJS, 197, 15

Evans, C. R., & Kochanek, C. S. 1989, ApJ, 346, L13

Fitzpatrick, E. L. 1999, PASP, 111, 63

Foote, H. R., Generozov, A., & Madigan, A.-M. 2020, ApJ, 890, 175

Foreman-Mackey, D., Hogg, D. W., Lang, D., & Goodman, J. 2013, PASP, 125, 306

Frank, J., & Rees, M. J. 1976, MNRAS, 176, 633

French, K. D., Arcavi, I., & Zabludoff, A. 2016, ApJ, 818, L21

—. 2017, ApJ, 835, 176

French, K. D., Arcavi, I., Zabludoff, A. I., et al. 2020, ApJ, 891, 93

Gadotti, D. A., & Kauffmann, G. 2009, Monthly Notices of the Royal Astronomical Society, 399, 621

Gafton, E., & Rosswog, S. 2019, MNRAS, 487, 4790

Gallegos-Garcia, M., Law-Smith, J., & Ramirez-Ruiz, E. 2018, ApJ, 857, 109

Gaskell, C. M., & Rojas Lobos, P. A. 2014, MNRAS, 438, L36

Gelman, A., Hwang, J., & Vehtari, A. 2014, Statistics and Computing, 24, 997

Gelman, A., & Rubin, D. B. 1992, Statistical Science, 7, 457

Gennaro, M., Brandner, W., Stolte, A., & Henning, T. 2011, in Stellar Clusters & Associations: A RIA Workshop on Gaia, 294–298

Gezari, S., Cenko, S. B., & Arcavi, I. 2017, The Astrophysical Journal Letters, 851, L47

Gezari, S., Chornock, R., Lawrence, A., et al. 2015, ApJ, 815, L5

Gezari, S., Basa, S., Martin, D. C., et al. 2008, ApJ, 676, 944

Gezari, S., Heckman, T., Cenko, S. B., et al. 2009, ApJ, 698, 1367

Gezari, S., Chornock, R., Rest, A., et al. 2012, Nature, 485, 217

Ginsburg, A., Parikh, M., Woillez, J., et al. 2016, astroquery: v0.3.2 release

Ginzburg, S., & Balberg, S. 2012, ApJ, 757, 178

Golightly, E. C. A., Nixon, C. J., & Coughlin, E. R. 2019, ApJ, 882, L26

Graham, A. W., & hui Li, I. 2009, The Astrophysical Journal, 698, 812

Greene, J. E., & Ho, L. C. 2007, ApJ, 667, 131

Greene, J. E., Peng, C. Y., Kim, M., et al. 2010, The Astrophysical Journal, 721, 26

Guillochon, J., Manukian, H., & Ramirez-Ruiz, E. 2014, ApJ, 783, 23

Guillochon, J., Nicholl, M., Villar, V. A., et al. 2017a, ArXiv e-prints, arXiv:1710.02145

—. 2018, ApJS, 236, 6

Guillochon, J., Parrent, J., Kelley, L. Z., & Margutti, R. 2017b, ApJ, 835, 64

Guillochon, J., & Ramirez-Ruiz, E. 2013, ApJ, 767, 25

—. 2015a, ApJ, 809, 166

—. 2015b, ApJ, 798, 64

Guillochon, J., Ramirez-Ruiz, E., Rosswog, S., & Kasen, D. 2009, ApJ, 705, 844

Gültekin, K., Richstone, D. O., Gebhardt, K., et al. 2009, ApJ, 698, 198

Haas, R., Shcherbakov, R. V., Bode, T., & Laguna, P. 2012, ApJ, 749, 117

Hamann, F., & Ferland, G. 1993, The Astrophysical Journal, 418, 11, aDS Bibcode: 1993ApJ...418...11H

Hayasaki, K., Stone, N., & Loeb, A. 2013, MNRAS, 434, 909

Hayasaki, K., Stone, N., & Loeb, A. 2016, MNRAS, 461, 3760

Hennebelle, P., & Chabrier, G. 2008, ApJ, 684, 395

Hillenbrand, L. A., & Hartmann, L. W. 1998, The Astrophysical Journal, 492, 540

Holoien, T. W.-S., Brown, J. S., Auchettl, K., et al. 2018a, Monthly Notices of the Royal Astronomical Society, sty2273

Holoien, T. W.-S., Prieto, J. L., Bersier, D., et al. 2014, MNRAS, 445, 3263

Holoien, T. W.-S., Kochanek, C. S., Prieto, J. L., et al. 2016a, ArXiv e-prints, arXiv:1602.01088

—. 2016b, MNRAS, 455, 2918

Holoien, T. W. S., Huber, M. E., Shappee, B. J., et al. 2018b, arXiv:1808.02890

Holoien, T. W. S., Vallely, P. J., Auchettl, K., et al. 2019, ApJ, 883, 111

Holoien, T. W. S., Auchettl, K., Tucker, M. A., et al. 2020, ApJ, 898, 161

Hopkins, P. F., & Hernquist, L. 2009, ApJ, 698, 1550

Hopkins, P. F., & Quataert, E. 2010, MNRAS, 405, L41

Hosek, M., Lu, J. R., Andersen, M., et al. 2019, BAAS, 51, 439

Hu, X. Y., Adams, N. A., & Iaccarino, G. 2009, Journal of Computational Physics, 228, 6572

Hung, T., Gezari, S., Blagorodnova, N., et al. 2017, The Astrophysical Journal, 842, 29

Hung, T., Cenko, S. B., Roth, N., et al. 2019, ApJ, 879, 119

Hung, T., Foley, R. J., Ramirez-Ruiz, E., et al. 2020, arXiv e-prints, arXiv:2003.09427

Hung, T., Foley, R. J., Veilleux, S., et al. 2021, ApJ, 917, 9

Ivanov, P. B., Polnarev, A. G., & Saha, P. 2005, MNRAS, 358, 1361

Jiang, N., Dou, L., Wang, T., et al. 2016, The Astrophysical Journal, 828, L14

Jiang, Y.-F., Greene, J. E., & Ho, L. C. 2011, ApJ, 737, L45

Jiang, Y.-F., Guillochon, J., & Loeb, A. 2016a, ApJ, 830, 125

—. 2016b, ArXiv e-prints, arXiv:1603.07733

Jonker, P. G., Stone, N. C., Generozov, A., Velzen, S. v., & Metzger, B. 2020, ApJ, 889, 166

Kara, E., Dai, L., Reynolds, C. S., & Kallman, T. 2018, MNRAS, 474, 3593

Kasliwal, M. M., Kulkarni, S. R., Gal-Yam, A., et al. 2012, ApJ, 755, 161

Kelley, L. Z., Blecha, L., & Hernquist, L. 2017, Monthly Notices of the Royal Astronomical Society, 464, 3131, aDS Bibcode: 2017MNRAS.464.3131K

Kesden, M. 2012a, Phys. Rev. D, 86, 064026

—. 2012b, Phys. Rev. D, 85, 24037

Khan, F. M., Just, A., & Merritt, D. 2011, The Astrophysical Journal, 732, 89, aDS Bibcode: 2011ApJ...732...89K

Khatami, D. K., & Kasen, D. N. 2019, The Astrophysical Journal, 878, 56, aDS Bibcode: 2019ApJ...878...56K

Kobayashi, S., Laguna, P., Phinney, E. S., & Mészáros, P. 2004, ApJ, 615, 855

Kochanek, C. S. 1994, ApJ, 422, 508

Kochanek, C. S. 2015, ArXiv e-prints, arXiv:1512.03065

—. 2016, MNRAS, arXiv:1601.06787

Kocsis, B., & Tremaine, S. 2015, Monthly Notices of the Royal Astronomical Society, 448, 3265, aDS Bibcode: 2015MNRAS.448.3265K

Kollmeier, J. A., Onken, C. A., Kochanek, C. S., et al. 2006, ApJ, 648, 128

Kozai, Y. 1962, The Astronomical Journal, 67, 591, aDS Bibcode: 1962AJ.....67..591K

Kroupa, P. 2001, MNRAS, 322, 231

Kroupa, P. 2001, MNRAS, 322, 231

Kroupa, P., Tout, C. A., & Gilmore, G. 1993, MNRAS, 262, 545

Laor, A., & Davis, S. 2011, arXiv e-prints, https://arxiv.org/abs/1110.0653

Larson, R. B. 2005, MNRAS, 359, 211

Law-Smith, J., Guillochon, J., & Ramirez-Ruiz, E. 2019, ApJ, 882, L25

Law-Smith, J., MacLeod, M., Guillochon, J., Macias, P., & Ramirez-Ruiz, E. 2017a, ApJ, 841, 132

Law-Smith, J., Ramirez-Ruiz, E., Ellison, S. L., & Foley, R. J. 2017b, ApJ, 850, 22

Law-Smith, J. A. P., Coulter, D. A., Guillochon, J., Mockler, B., & Ramirez-Ruiz, E. 2020, arXiv e-prints, arXiv:2007.10996

Leloudas, G., Fraser, M., Stone, N. C., et al. 2016, ArXiv e-prints, arXiv:1609.02927

Leloudas, G., Dai, L., Arcavi, I., et al. 2019, ApJ, 887, 218

Li, G., Naoz, S., Kocsis, B., & Loeb, A. 2015, MNRAS, 451, 1341

Lidov, M. L. 1962, Planetary and Space Science, 9, 719

Liu, F. K., Zhou, Z. Q., Cao, R., Ho, L. C., & Komossa, S. 2017, MNRAS, 472, L99

Lodato, G. 2012, in European Physical Journal Web of Conferences, Vol. 39, European Physical Journal Web of Conferences, 01001

Lodato, G., King, A. R., & Pringle, J. E. 2009, MNRAS, 392, 332

Lodato, G., & Rossi, E. M. 2011, MNRAS, 410, 359

Loeb, A., & Ulmer, A. 1997, ApJ, 489, 573

Lu, J. R., Do, T., Ghez, A. M., et al. 2013, ApJ, 764, 155

Lu, W., & Bonnerot, C. 2020, MNRAS, 492, 686

Lu, W., & Kumar, P. 2018, ApJ, 865, 128

López-Sanjuan, C., Le Fèvre, O., Ilbert, O., et al. 2012, Astronomy and Astrophysics, 548, A7

MacLeod, M., Guillochon, J., & Ramirez-Ruiz, E. 2012, ApJ, 757, 134

Madigan, A.-M., Halle, A., Moody, M., et al. 2018, ApJ, 853, 141

Magorrian, J., & Tremaine, S. 1999, MNRAS, 309, 447

Manukian, H., Guillochon, J., Ramirez-Ruiz, E., & O'Leary, R. M. 2013, ApJ, 771, L28

Marconi, A., Risaliti, G., Gilli, R., et al. 2004, The Interplay among Black Holes, 222, 49

Margutti, R., Metzger, B. D., Chornock, R., et al. 2017, ApJ, 836, 25

Mazzolari, G., Bonetti, M., Sesana, A., et al. 2022, Extreme Mass Ratio Inspirals triggered by Massive Black Hole Binaries: from Relativistic Dynamics to Cosmological Rates, Tech. rep.,

McConnell, N. J., & Ma, C.-P. 2013, ApJ, 764, 184

McLure, R. J., & Jarvis, M. J. 2002, MNRAS, 337, 109

Melchor, D., Mockler, B., Naoz, S., Rose, S. C., & Ramirez-Ruiz, E. 2022, in prep.

Menanteau, F., Jimenez, R., & Matteucci, F. 2001, ApJ, 562, L23

Mendel, J. T., Simard, L., Palmer, M., Ellison, S. L., & Patton, D. R. 2014, ApJS, 210, 3

Metzger, B. D., & Stone, N. C. 2016, MNRAS, 461, 948

Mihos, J. C., & Hernquist, L. 1994, ApJ, 425, L13

Miller, J. M., Kaastra, J. S., Miller, M. C., et al. 2015, Nature, 526, 542

Miller, M. C. 2015, ApJ, 805, 83

Mockler, B., Denyz, M., Smadar, N., & Enrico, R. 2021, submitted to ApJ

Mockler, B., Guillochon, J., & Ramirez-Ruiz, E. 2019a, The Astrophysical Journal, 872, 151

—. 2019b, The Astrophysical Journal, 872, 151

Mockler, B., & Ramirez-Ruiz, E. 2020, arXiv e-prints, arXiv:2007.12198

—. 2021, ApJ, 906, 101

Mockler, B., Twum, A. A., Auchettl, K., et al. 2022, The Astrophysical Journal, 924, 70, aDS Bibcode: 2022ApJ...924...70M

Morrison, R., & McCammon, D. 1983, ApJ, 270, 119

Naoz, S. 2016, Annual Review of Astronomy and Astrophysics, 54, 441

Naoz, S., Kocsis, B., Loeb, A., & Yunes, N. 2013, ApJ, 773, 187

Naoz, S., Rose, S. C., Michaely, E., et al. 2022, ApJL, 927, L18

Negueruela, I., Clark, J. S., & Ritchie, B. W. 2010, A&A, 516, A78

Nicholls, B., Holoien, T. W.-S., Stanek, K. Z., et al. 2015, The Astronomer's Telegram, 7642

Norton, S. A., Gebhardt, K., Zabludoff, A. I., & Zaritsky, D. 2001, ApJ, 557, 150

Novikov, I. D., & Thorne, K. S. 1973, in Black Holes (Les Astres Occlus), ed. C. DeWitt & B. DeWitt (N.Y.: Gordon and Breach), 343–450

O'Donnell, J. E. 1994, ApJ, 422, 158

O'Leary, R. M., Kocsis, B., & Loeb, A. 2009, MNRAS, 395, 2127

Onori, F., Cannizzaro, G., Jonker, P. G., et al. 2019, MNRAS, 489, 1463

Pancoast, A., Brewer, B. J., & Treu, T. 2014a, MNRAS, 445, 3055

Pancoast, A., Brewer, B. J., Treu, T., et al. 2014b, MNRAS, 445, 3073

Pancoast, A., Barth, A. J., Horne, K., et al. 2018, ApJ, 856, 108

Pandya, V., Brennan, R., Somerville, R. S., et al. 2017, MNRAS, 472, 2054

Parker, R. J., Bouvier, J., Goodwin, S. P., et al. 2011, MNRAS, 412, 2489

Paumard, T., Genzel, R., Martins, F., et al. 2006, ApJ, 643, 1011

Paxton, B., Bildsten, L., Dotter, A., et al. 2011, ApJS, 192, 3

Paxton, B., Bildsten, L., Dotter, A., et al. 2011, ApJS, 192, 3

Paxton, B., Cantiello, M., Arras, P., et al. 2013, The Astrophysical Journal Supplement Series, 208, 4

Paxton, B., Cantiello, M., Arras, P., et al. 2013, ApJS, 208, 4

Paxton, B., Marchant, P., Schwab, J., et al. 2015, The Astrophysical Journal Supplement Series, 220, 15

Paxton, B., Marchant, P., Schwab, J., et al. 2015, ApJS, 220, 15

Payne, A. V., Shappee, B. J., Hinkle, J. T., et al. 2022, ApJ, 926, 142

Peterson, B. M. 2015, Measuring the Masses of Supermassive Black Holes, ed. M. Falanga, T. Belloni, P. Casella, M. Gilfanov, P. Jonker, & A. King (New York, NY: Springer New York), 253–275

Phinney, E. S. 1989, The Center of the Galaxy: Proceedings of the 136th Symposium of the International Astronomical Union, 136, 543

Pipino, A., Kaviraj, S., Bildfell, C., et al. 2009, MNRAS, 395, 462

Piran, T., Svirski, G., Krolik, J., Cheng, R. M., & Shiokawa, H. 2015, ApJ, 806, 164

Piro, A. L., & Lu, W. 2020, The Astrophysical Journal, 894, 2, aDS Bibcode: 2020ApJ...894....2P

Plunkett, A. L., Fernández-López, M., Arce, H. G., et al. 2018, A&A, 615, A9

Pracy, M. B., Owers, M. S., Couch, W. J., et al. 2012, MNRAS, 420, 2232

Pracy, M. B., Croom, S., Sadler, E., et al. 2013, MNRAS, 432, 3131

Raimundo, S. I., Fabian, A. C., Vasudevan, R. V., Gandhi, P., & Wu, J. 2012, Monthly Notices of the Royal Astronomical Society, 419, 2529

Ramirez-Ruiz, E., & Rosswog, S. 2009, ApJ, 697, L77

Rauch, K. P., & Tremaine, S. 1996, New A, 1, 149

Rees, M. J. 1988, Nature, 333, 523

Rodriguez-Gomez, V., Genel, S., Vogelsberger, M., et al. 2015, Monthly Notices of the Royal Astronomical Society, 449, 49, aDS Bibcode: 2015MNRAS.449...49R

Rosswog, S., Ramirez-Ruiz, E., & Hix, W. R. 2009, ApJ, 695, 404

Roth, N., & Kasen, D. 2018, ApJ, 855, 54

Roth, N., Kasen, D., Guillochon, J., & Ramirez-Ruiz, E. 2016, ApJ, 827, 3

Ryu, T., Krolik, J., Piran, T., & Noble, S. C. 2020, ApJ, 904, 98

Sánchez-Janssen, R., Puzia, T. H., Ferrarese, L., et al. 2019, MNRAS, 486, L1

Sari, R., & Fragione, G. 2019, ApJ, 885, 24

Sądowski, A., Tejeda, E., Gafton, E., Rosswog, S., & Abarca, D. 2016, MNRAS, 458, 4250

Schödel, R., Nogueras-Lara, F., Gallego-Cano, E., et al. 2020, A&A, 641, A102

Servin, J., & Kesden, M. 2017, Phys. Rev. D, 95, 083001

Shiokawa, H., Krolik, J. H., Cheng, R. M., Piran, T., & Noble, S. C. 2015, ApJ, 804, 85

Stone, N., & Loeb, A. 2012, Physical Review Letters, 108, 061302

Stone, N. C., Generozov, A., Vasiliev, E., & Metzger, B. D. 2018, MNRAS, 480, 5060

Stone, N. C., & Metzger, B. D. 2016, MNRAS, 455, 859

Strubbe, L. E., & Quataert, E. 2009, MNRAS, 400, 2070

Tejeda, E., Gafton, E., & Rosswog, S. 2017, ArXiv e-prints, arXiv:1701.00303

Thomas, D., Steele, O., Maraston, C., et al. 2013, Monthly Notices of the Royal Astronomical Society, 431, 1383

Tout, C. A., Pols, O. R., Eggleton, P. P., & Han, Z. 1996, MNRAS, 281, 257

Tremaine, S. 1995, AJ, 110, 628

Ulmer, A., Paczynski, B., & Goodman, J. 1998, A&A, 333, 379

van Velzen, S., Gezari, S., Hung, T., et al. 2019, The Astronomer's Telegram, 12568, 1

van Velzen, S., Mendez, A. J., Krolik, J. H., & Gorjian, V. 2016a, ArXiv e-prints, arXiv:1605.04304

van Velzen, S., Stone, N. C., Metzger, B. D., et al. 2019, The Astrophysical Journal, 878, 82

van Velzen, S., Farrar, G. R., Gezari, S., et al. 2011, ApJ, 741, 73

van Velzen, S., Anderson, G. E., Stone, N. C., et al. 2016b, Science, 351, 62

van Velzen, S., Gezari, S., Hammerstein, E., et al. 2020, arXiv e-prints, arXiv:2001.01409

—. 2021, ApJ, 908, 4

Vasiliev, E. 2017, ApJ, 848, 10

Vasiliev, E., & Merritt, D. 2013, ApJ, 774, 87

Vestergaard, M. 2002, ApJ, 571, 733

Wang, J., & Merritt, D. 2004, ApJ, 600, 149

Watanabe, S. 2010, Journal of Machine Learning Research, 11, 3571

Wegg, C., & Nate Bode, J. 2011, ApJ, 738, L8

Wen, S., Jonker, P. G., Stone, N. C., Zabludoff, A. I., & Psaltis, D. 2020, ApJ, 897, 80

Wernke, H. N., & Madigan, A.-M. 2019, The Astrophysical Journal, 880, 42, aDS Bibcode: 2019ApJ...880...42W

Wernke, H. N., & Madigan, A.-M. 2019, ApJ, 880, 42

Wevers, T., van Velzen, S., Jonker, P. G., et al. 2017, ArXiv e-prints, arXiv:1706.08965

Wyrzykowski, Ł., Zieliński, M., Kostrzewa-Rutkowska, Z., et al. 2017, MNRAS, 465, L114

Xiao, T., Barth, A. J., Greene, J. E., et al. 2011, The Astrophysical Journal, 739, 28

Yang, C., Wang, T., Ferland, G. J., et al. 2017, The Astrophysical Journal, 846, 150

Yang, Y., Zabludoff, A. I., Zaritsky, D., & Mihos, J. C. 2008, ApJ, 688, 945

Zhang, E., Naoz, S., & Will, C. M. 2022, in prep.

Zhou, Z. Q., Liu, F. K., Komossa, S., et al. 2021, ApJ, 907, 77